ulm university universität uulm

Annual Report 2017

Institute of Optoelectronics

Cover photo:
Photograph of a large parabolic mirror with two retro-reflective prisms for multipass quantum-well pumping of a semiconductor disk laser. The green light is generated by an infrared laser beam visualizer detecting the 940 nm pump light. The optically excited disk laser chip emitting spontaneous light is visible through the opening in the middle of the parabolic mirror. The article on page 37 describes the setup and demonstrates a pump power absorption of over 75 % with this multipass pump setup.

Contents

1:	Vignesh Devaki Murugesan	2:	Ferdinand Scholz	3:	Martin Schneidereit
4:	Jürgen Mähnß	5:	Jan-Patrick Scholz	6:	Karl Joachim Ebeling
7:	Sven Bader	8:	Irene Lamparter	9:	Markus Miller
10:	Rainer Blood	11:	Markus Polanik	12:	Thomas Zwosta
13:	Jassim Bin Shahbaz	14:	Susanne Menzel	15:	Tobias Pusch
16:	Rainer Michalzik	17:	Oliver Rettig	18:	Peter Unger

Not on the photo:

Sükran Kilic, Eva Nüßle, Rudolf Rösch, Ilona Schwaiger

Ulm University
Institute of Optoelectronics

Albert-Einstein-Allee 45, 89081 Ulm, Germany
URL: http://www.uni-ulm.de/opto
Fax: +49–731/50–26049
Phone: +49–731/50–

Acting Director of Institute

Prof. Dr.	Hans-Jörg Fecht	–25490	hans.fecht@uni-ulm.de

Deputy Directors

Prof. Dr.	Ferdinand Scholz	–26052	ferdinand.scholz@uni-ulm.de
Prof. Dr.	Peter Unger	–26054	peter.unger@uni-ulm.de

Group Leader

apl. Prof. Dr.-Ing.	Rainer Michalzik	–26048	rainer.michalzik@uni-ulm.de

Emeritus Director

Prof. Dr.	Karl Joachim Ebeling	–26051	karl.ebeling@uni-ulm.de

Cleanroom Management

Dr.-Ing.	Jürgen Mähnß	–26053	juergen.maehnss@uni-ulm.de

Secretaries

	Sükran Kilic	–26059	suekran.kilic@uni-ulm.de
	Hildegard Mack*	–26060	hildegard.mack@uni-ulm.de
	Eva Nüßle	–26050	eva.nuessle@uni-ulm.de

Research Staff

M. Sc.	Sven Bader	–26037	sven.bader@uni-ulm.de
M. Sc.	Markus Daubenschüz*	–26038	markus.daubenschuez@uni-ulm.de
M. Sc.	Vignesh Devaki Murugesan	–26038	vignesh.devaki@uni-ulm.de
M. Sc.	Markus Miller	–26038	markus.miller@uni-ulm.de
M. Sc.	Markus Polanik	–26046	markus.polanik@uni-ulm.de
M. Sc.	Tobias Pusch	–26037	tobias.pusch@uni-ulm.de
M. Sc.	Oliver Rettig	–26036	oliver.rettig@uni-ulm.de
M. Sc.	Martin Schneidereit	–26039	martin.schneidereit@uni-ulm.de
M. Sc.	Jan-Patrick Scholz	–26044	jan-patrick.scholz@uni-ulm.de
M. Sc.	Jassim Bin Shahbaz	–26039	jassim.shahbaz@uni-ulm.de

Technical Staff

	Rainer Blood	–26044	rainer.blood@uni-ulm.de
	Irene Lamparter	–26057	irene.lamparter@uni-ulm.de
	Susanne Menzel	–26041	susanne.menzel@uni-ulm.de
	Rudolf Rösch	–26057	rudolf.roesch@uni-ulm.de
	Ilona Schwaiger+	–26036	ilona.schwaiger@uni-ulm.de
	Thomas Zwosta	–26036	thomas.zwosta@uni-ulm.de

* Is an alumnus of the Institute meanwhile

+ Currently on parental leave

Preface

On Sep. 30, 2017, Prof. Karl Joachim Ebeling retired from his position as the Director of the Institute of Optoelectronics which he held from its establishment in 1989 until 2001 and again over the last two years after his time as President of Ulm University. We thank him for his encouraging leadership and many years of fruitful and enjoyable cooperation. Currently, Prof. Hans-Jörg Fecht, Director of the Institute of Micro and Nanomaterials, is appointed as the Acting Director of Optoelectronics. According to the plans of the Faculty of Engineering, Computer Science and Psychology of Ulm University, our Institute will become part of an Institute of Functional Nanosystems (FNS) to be established in 2018. Ferdinand Scholz, Peter Unger, and Rainer Michalzik will continue their research activities under the umbrella of FNS. As a consequence, this 28th Annual Report of the Institute of Optoelectronics will most probably be the last issue, as indicated on the back side of the cover. A sum total of more than 1000 technical papers has been published so far.

On the technical side, the VCSELs and Optical Interconnects Group has continued the research on four topics, namely VCSELs with monolithically integrated phototransistors for optically controlled current confinement, spintronic VCSELs with high and tunable birefringence for future polarization modulation schemes, a new time-of-flight-based method for depth imaging using VCSEL illumination, as well as refractive index sensing with VCSEL-related resonant devices, the latter two with the involvement of K.J. Ebeling. As an outlook, the VCSEL Group will organize the *11th European VCSEL Day* Workshop on April 12 and 13, 2018 in the premises of the University West campus.

In 2017, the GaN group could acquire funding of a project which focuses on vertical field effect transistors in cooperation with the Fraunhofer Institute of Applied Solid State Physics (Freiburg) and the University of Freiburg. This activity strengthens our research concerning low defect density GaN grown by hydride vapor phase epitaxy. Our sensor activities have further intensified the cooperation with our colleagues from Organic Chemistry (Prof. T. Weil), a quite exciting and new field for us. Also the studies about AlBGaN have brought many interesting results, substantially supported by a guest scientist from the Czech Academy of Sciences (Prague), Dr. Markéta Zíková.

In the High-Power Semiconductor Laser Group, a multipass pump optics for quantum-well-pumped semiconductor disk lasers has been developed allowing up to three double passes of the pump light through the laser disk. Absorption rates of more than 75 % have been achieved with this setup yielding 16 W of continuous output power and slope efficiencies above 50 %.

Hildegard Mack, a secretary of the Institute for many years, has accepted a new position in the administration of Ulm University. We thank her for the great service and wish her all the best. We are grateful to Sükran Kilic for taking over most of her responsibilities.

Finally we thank all readers for the interest in the Annual Report series of our Institute.

Rainer Michalzik
Ferdinand Scholz
Peter Unger Ulm, March 2018

Investigation of Thin AlBGaN Layers Grown by MOVPE

Oliver Rettig

In this article, epitaxial growth of AlBGaN layers and superlattices with boron content in the lower percentage regime are investigated. The focus of this work lies on the growth development of thin layers and their luminescent properties. Only very few reports in literature investigate photoluminescence of these layers due to the poorer crystal quality compared to conventional AlGaN layers. Here we show that the addition of boron to AlGaN leads to 3D-like growth with tilted facets. In contrast to thicker layers, thin layers of AlBGaN layers show similarly strong luminescence compared to AlGaN layers, and therefore have potential for applications in UV-LEDs.

1. Introduction

Group III nitrides such as InN, GaN, AlN and their alloys have attracted a lot of interest due to their potential in providing high efficiency electronic and optoelectronic devices in a broad spectral regime including UV-C through to the whole visible spectrum [1]. Whereas for InGaN based blue to green LEDs already very high efficiencies have been achieved, AlGaN based UV devices still suffer from relatively poor external quantum efficiencies below 21 % [2]. Over the recent years a lot of progress has been made to reduce problems like high dislocation densities in AlGaN epitaxial layers [3], low carrier injection efficiency into the active region [3] and low light outcoupling efficiency [2]. Another major challenge is the very strong internal field in the quantum well (QW) active region due to lattice mismatch, leading to a strong decrease in overlap of the carrier wave functions and thus to a decrease in internal quantum efficiency. As a potential material allowing to reduce the strain in the QW, AlBGaN has been proposed [4]. By adding boron as the lightest and smallest group III element to the currently used AlGaN system, another degree of freedom in band gap and lattice constant tailoring can be utilized. To lattice-match AlBGaN QWs with an aluminium content of 50 % to an AlN barrier, a boron incorporation below 6 % would be sufficient [5, 6]. However, the solubility of boron in AlGaN is very low.

Recent experimental studies show single phase epitaxial growth of AlBN for boron contents up to ∼10 % [7]. However, provided TEM micrographs seem to indicate irregularities in the crystalline structure which might be due to the fact that the solubility limit is reached if not even exceeded, as evidenced by spinodal isotherm calculations where a maximum boron content of 3 % for a stable phase in AlN and GaN is predicted for a growth temperature of 1000 °C [8,9]. This may be also the reason that up to now we could not find acceptable photoluminescence data of AlBGaN layers even with low B content in the open literature.

Considering state-of-the-art UV-LED devices [2], $Al_xGa_{1-x}N$ quantum wells ($x = 0.4$) and barriers ($x = 0.55$) have a difference in aluminium composition of $\Delta x = 15\,\%$. Lattice matching of both layers could be achieved by incorporating only small B amounts of about 2 % in the quantum wells, assuming the validity of Vegard's law and lattice constants of 0.3112 nm, 0.3189 nm, and 0.2549 nm for the binaries AlN, GaN, and wurtzite BN, respectively [6, 10]. Still, the low solubility, but also parasitic gas phase reactions and low surface mobility of boron, make it very challenging to grow high quality quaternary AlBGaN alloys with appropriate optoelectronic properties [11,12,14]. In this research, we therefore concentrate on the MOVPE growth and characterization of AlBN and AlBGaN layers with low B content. We try to retain good crystallinity for boron containing layers with good luminescence characteristics to study the applicability of this quaternary material in future LEDs.

2. Experimental Details

For this study a low-pressure horizontal flow MOVPE reactor (Aixtron Aix-200/4 RF-S) with high-temperature kit is used, allowing growth temperatures up to 1400 °C. For all experiments 500–900 nm thick AlN templates were used which were grown on (0001) sapphire substrates with a 0.3° offcut towards the m-plane. The optimized AlN templates show a full width at half maximum (FWHM) below 50 arcsec and 1000 arcsec for the (0002) and $(10\bar{1}2)$ reflexes, respectively, in high resolution x-ray diffraction (HRXRD). Precursors for epitaxial growth were trimethyl-aluminium (TMAl), trimethyl-gallium (TMGa), triethyl-boron (TEB), and ammonia (NH_3). Ex-situ characterization involves, besides HRXRD, aberration-corrected high-resolution transmission electron microscopy (AC-HRTEM), low temperature photoluminescence spectroscopy (PL) at 8 K with an argon fluoride excimer laser excitation source ($\lambda = 193$ nm), atomic force microscopy (AFM) and secondary ion mass spectrometry (SIMS). For cross-sectional TEM investigations, the samples were ground to a thickness of 100 µm and further trenched down below 5 µm. Ion milling was performed with 5 kV at 10° incident angle in a Fischione Ion Mill 1010. Liquid nitrogen cooling was applied to reduce amorphization due to ion bombardment.

3. Results and Discussion

3.1 Growth of thin AlBGaN layers

The results presented above indicate that thin layers with low B content may have good crystalline properties. To further investigate the development of 3D growth and its impact on the PL characteristics of the layers, thin single AlBGaN layers were grown on AlN templates. Ga was added to the thin layers to be able to clearly identify luminescence from the boron containing layer besides the luminescence of the AlN template. The B/III-ratio was chosen to be 0.7 % due to the trend for better crystal quality at lower boron contents [14]. Further, the Ga/III-ratio was set to 46 %, the reactor pressure was set to 35 hPa and the surface temperature is kept at 1160 °C. On similarly grown single layer structures, SIMS measurements revealed a boron and Ga incorporation of ∼1 % and

$\sim$30 %, respectively. This leads to an estimated lattice mismatch between the AlBGaN and AlN layers of $\sim$0.5 %. Corresponding AFM studies of layers with thicknesses from 5–20 nm are displayed in Fig. 1.

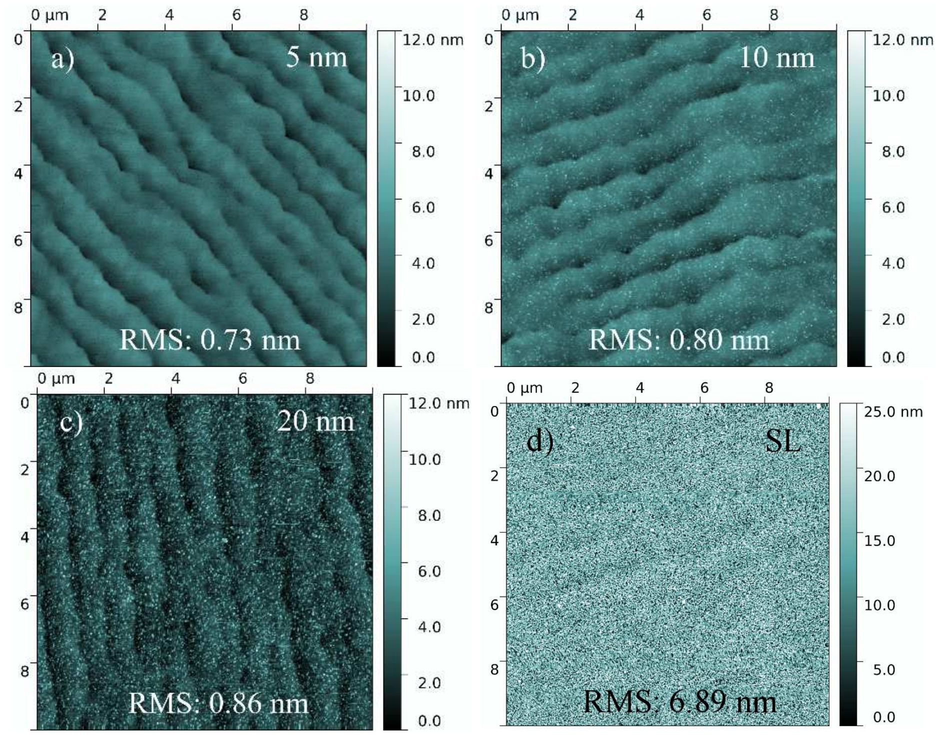

Fig. 1: AFM images (10 µm × 10 µm) of AlBGaN layers with varying thicknesses (a–c) and from an AlBGaN/AlN superlattice structure (d).

Growth steps, visible in all AFM images, originate from the AlN template. Even after 20 nm of AlBGaN growth, they are still visible, indicating an ongoing 2D growth mode not heavily impacted by the presence of boron. Also the RMS roughness values of the surface do not significantly increase when comparing 5 nm and 20 nm thick layers with values of 0.73 nm and 0.86 nm, respectively, showing that the growth is mainly occurring in 2D mode.

Table 1: Comparison of the dislocation and grain densities of the investigated samples.

Sample	template disloc. density	column/grain
300 nm AlBN	$<10^{10}\,\mathrm{cm}^{-2}$	$\sim 2 \cdot 10^{11}\,\mathrm{cm}^{-2}$
10 nm AlBGaN	$<10^{10}\,\mathrm{cm}^{-2}$	$\sim 1.6 \cdot 10^{9}\,\mathrm{cm}^{-2}$
20 nm AlBGaN	$<10^{10}\,\mathrm{cm}^{-2}$	$\sim 1.2 \cdot 10^{10}\,\mathrm{cm}^{-2}$

However, small grainy features can be observed on the surfaces starting from 10 nm thick AlBGaN layers. This is exemplarily shown in Fig. 2, exhibiting a magnified part of the sample of Fig. 1 (b). The features become more pronounced and their density increases from $\sim 1.6 \cdot 10^{9}\,\mathrm{cm}^{-2}$ for a 10 nm thick AlBGaN layer to $\sim 1.2 \cdot 10^{10}\,\mathrm{cm}^{-2}$ for a 20 nm thick layer. The densities are calculated by counting the white spots present in the 10 µm × 10 µm AFM micrographs (Fig. 1), which have heights typically around 2–3 nm,

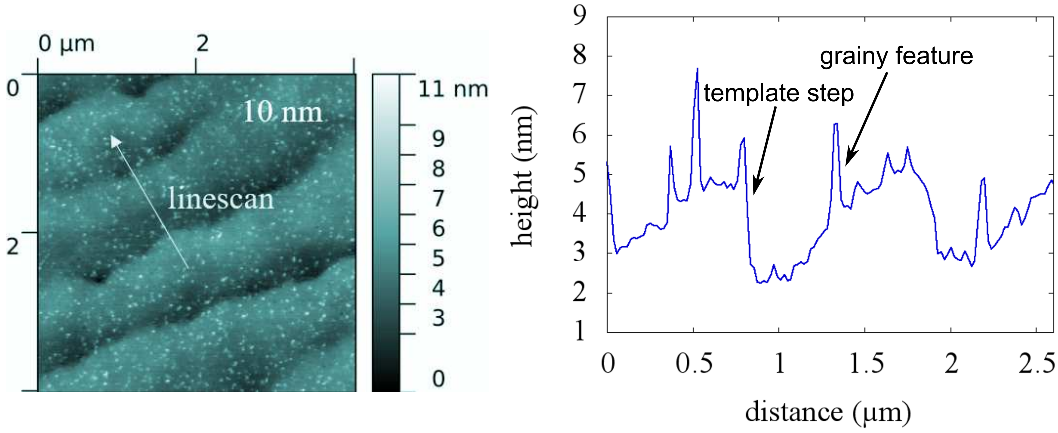

Fig. 2: AFM line profile (right) of the 10 nm thick AlBGaN layer measured perpendicular to the steps on the template (left).

as illustrated in a line scan in Fig. 2. They have an average width of ∼30 nm, which is in good agreement with the width of the columns observed for our thicker AlBN layers [13] and columnar sizes found by Li et al. [14,15]. The density of the columns ($\sim 2 \cdot 10^{11}\,\mathrm{cm}^{-2}$) measured on the samples shown in the previous annual report [13] exceeds the density of the threading dislocations ($<10^{10}\,\mathrm{cm}^{-2}$) estimated from XRD calculations by over an order of magnitude (see also Table 1). Therefore, we exclude a correlation between columnar growth or the formation of grains and the threading dislocation density. Also no evidence of such a dependence was found in weak-beam dark-field investigations on similar samples.

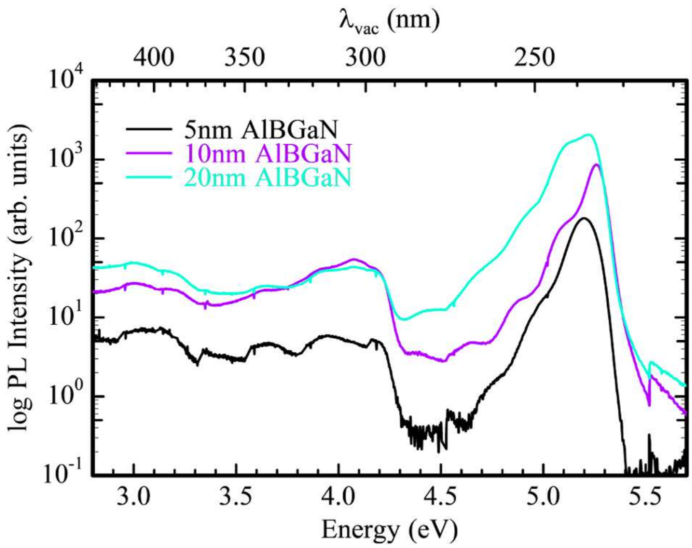

Fig. 3: PL spectra from an AlBGaN layer thickness series from 5–20 nm.

Logarithmic PL spectra from the thin layers are displayed in Fig. 3. The peak at 5.2 eV can be attributed to the near band edge (NBE) luminescence of AlBGaN. The dependence of the band edge energy and the composition in AlBN or BGaN is not yet well known.

Theoretical calculations for wurtzite BN predict a direct and indirect band gap of 10.2 eV and 6.8 eV, respectively [16]. For the bowing parameters of the direct band gap of AlBN high values of ∼7 eV can be approximated from graphs shown by Zhang et al. [16]. BGaN also exhibits strong bowing of ∼3.61 eV [17]. Hence for 1 % of boron in AlN and GaN, only small shifts of the band gap energy in the range of −20 meV to −40 meV are expected. Therefore, the band gap energy is predominantly defined by the AlGaN composition.

From the NBE luminescence at 5.2 eV it is clearly visible that layers up to 20 nm thickness containing about ∼1 % of boron maintain good luminescence yields despite the presence of small 3D growth features. In these spectra, the NBE luminescence intensity increases for thicker layers, showing no sign of deterioration of the crystal quality. This might be partially due to the fact that the optically active volume increases for thicker layers. In the energy range 4.5–5.2 eV, Fabry–Pérot fringes are visible, which correlate with the thickness of the template (∼900 nm). The broadening of the NBE peak might be caused by compositional fluctuations of the thin AlBGaN layers.

We attribute the broad band ranging from 3 eV [18, 19] to 4 eV [19–21] to silicon, oxygen and carbon related defects and their complexes. Their intensities are not strongly influenced by the layer thickness, despite the roughening of the surface which could have indicated a deterioration of the crystal quality and increase in structural defects.

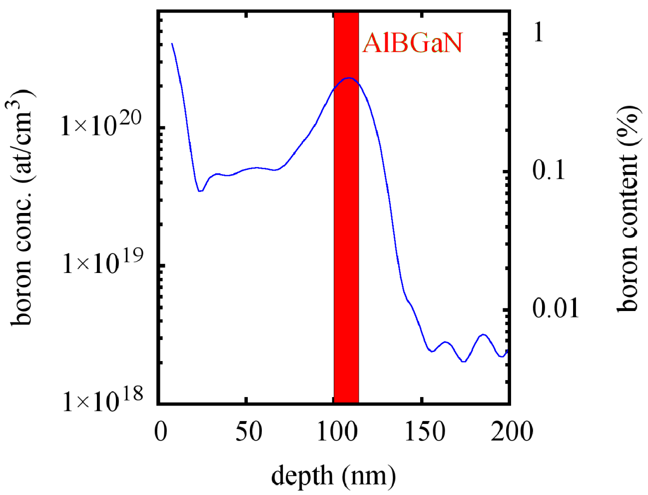

Fig. 4: SIMS measurement of the boron concentration of a ∼14 nm thick AlBGaN layer capped by 100 nm of AlN.

For thicker boron containing layers, columnar growth was observed [13]. The change in growth mode from 2D to a 3D process might have influence on the boron incorporation efficiency into Al(Ga)N. Therefore, SIMS investigations were performed on thin layers. For this study an additional sample was grown under the same growth conditions as described above. Due to artefacts at the start of the SIMS measurement, which can be observed in the concentration profile at the surface (Fig. 4), the thin AlBGaN layer needs to be buried in a capping layer, in this case chosen to be 100 nm AlN. The thickness of the AlBGaN layer is ∼14 nm. However, the boron signal smears over a depth more than that. This is attributed to the already depicted roughness of AlN capped AlBGaN, which reduces the depth resolution in SIMS. Therefore, the boron concentration was evaluated by integrating the total amount of boron divided by the initial AlBGaN layer thickness. This results in a boron content of ~1.5 %. However, the actual boron content in AlBGaN might be slightly lower in case of a memory effect of boron in the gas phase. After the decrease of the B concentration curve, between about 75 and 25 nm SIMS depth, the B signal levels off at a significantly higher level than the AlN template's background noise level of boron ($\sim 2 \cdot 10^{18}\,\mathrm{cm}^{-3}$ at 150 nm and deeper). This could be an indication of a memory effect of boron.

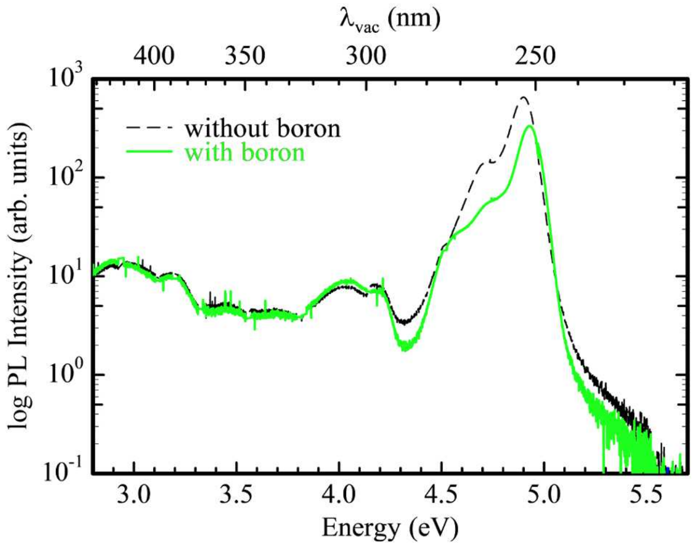

Fig. 5: Low temperature PL spectra at 7 K from an AlBGaN and an AlGaN layer with a thickness of 20 nm each, grown on the same template only differing in an extra supply of TEB.

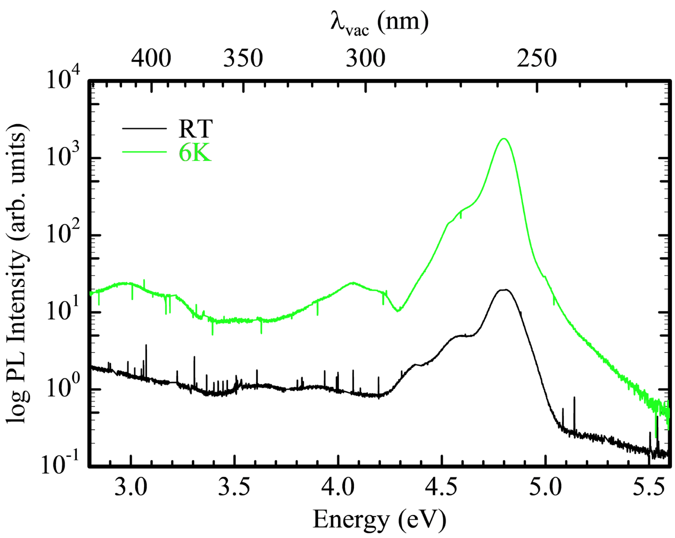

Fig. 6: Room and low temperature PL spectra from a 20 nm thick AlBGaN layer.

A direct comparison of the PL of B-containing and B-free layers grown otherwise under the same conditions is depicted in Fig. 5. Compared to the samples shown in Fig. 3, these samples have slightly increased Ga supply in the gas phase from 46 % to 54 %, which results in a redshift. As described above, with the incorporation of small amounts of boron, a negative energy shift of the NBE luminescence is expected. However, in Fig. 5 a minor positive change of the peak energy of ∼30 meV is observed. Again, small Al/Ga composition shifts from run to run or across the sample area may cause such differences. The B-containing layer shows quite strong PL with about half the intensity of the boron-free layer. Both layers show a broadening of the NBE peak towards lower energies. This might be attributed to composition fluctuations in the AlGaN or AlBGaN layers. No enhanced defect luminescence between 3 eV and 4 eV is visible (Fig. 5) for the boron containing layer as compared to pure AlGaN layers. This indicates, that the presence of boron does not promote the formation of silicon, oxygen or carbon related vacancies. Therefore, we attribute the decrease in PL intensity to non-radiative recombination, presumably related to an increased amount of stacking faults and edge-type dislocations, as discussed in the next section.

A comparison of the room and low temperature PL spectra of an AlBGaN layer is shown in Fig. 6. We observe a strong decrease of about two orders of magnitude in band edge luminescence for the higher temperature. This is again an indication of a considerable amount of defects present in boron containing layers. No redshift can be observed for the room temperature PL compared to the measurement at 6 K, which would be expected due to the temperature dependence of the band gap. This might be explained by a local fluctuation of the Ga, Al and B compositions. At higher temperatures carriers also recombine at regions with locally higher Al content and consequently higher band gap energy, mitigating the reduction of the band gap at higher temperatures.

3.2 Growth of AlBGaN/AlN superlattice structure

To visualize the temporal development of the 3D growth, we grew an AlBGaN/AlN superlattice (SL) structure with thicknesses of approximately 7 nm and 10 nm, respectively, as confirmed by cross-section high angle annular dark field (HAADF)-STEM micrographs (Fig. 8). The growth conditions were kept the same as in the previous experiment. Hence the B content of the AlBGaN layers is estimated to be about 1 %.

Owing to the high amount of Ga in these layers, we observe very clear interfaces between the AlN and AlBGaN layers. As expected from the AlBN layers described in the previous annual report [13] and the thin AlBGaN layers in Sect. 3.1, the first AlBGaN/AlN interfaces are very smooth. However, in the upper AlBGaN layers a blurred contrast can be seen. After few periods, some 3D growth develops. The layer stacking still can be identified, but inclined facets occur for many areas in the cross-section, which may be explained by the formation of many small V-pit-like defects or more stable tilted side facets compared to c-plane. The blurring may be explained by the finite thickness of the TEM specimen, which is ∼100 nm, estimated from energy-filtered transmission electron microscopy (EFTEM) measurements. Hence we see a projection over randomly positioned V-pits. Due to the small thickness of the AlBGaN layers and the surface roughness, estimation of the boron content by HRXRD was not possible.

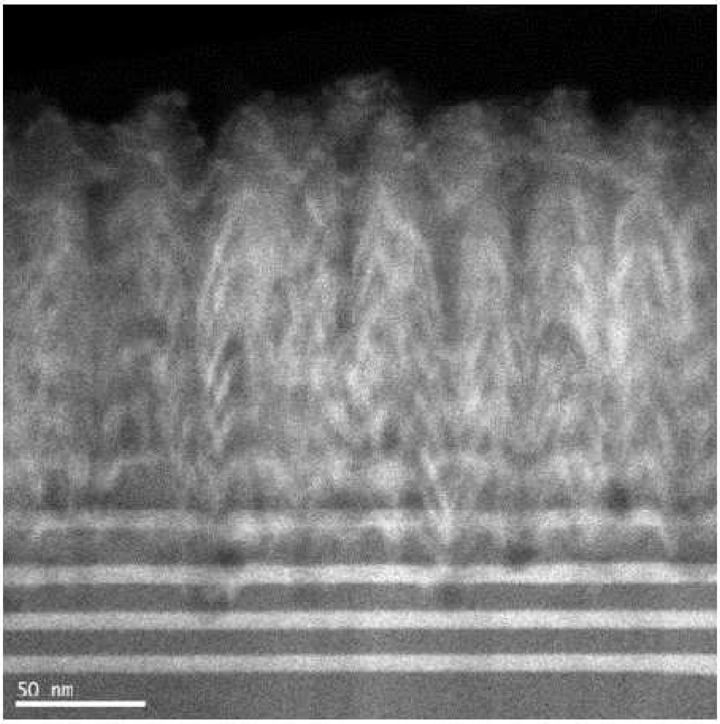

Fig. 7: HAADF image of an AlBGaN/AlN superlattice structure. The AlBGaN layers appear brighter than the AlN. The first periods grow nicely aligned, however, after a few stacks strong 3D growth can be observed.

Recent studies have shown that B-III-N based crystals can exhibit lattice twinning [22] or tilting [7]. SAED measurements (Fig. 8 a–d) were carried out to prove the absence of lattice twinning and polycrystalline growth. There are no additional diffraction spots apart from the wurtzite AlN in the lower SL region (Fig. 8 a,b). Here, the AlN template, the first well aligned SL periods and the upper part of the SL contribute to the diffraction pattern. Also investigations from only the upper part of the SL (Fig. 8 c,d) clearly show single phase wurtzite material without lattice twinning or tilting. The tilted facets visible in cross-section micrographs (Fig. 7) are therefore not occurring due to a tilt of the lattice planes, but refer to 3D growth with inclined facets. WBDF images from this sample show no correlation of threading dislocations and the columns. In Fig. 8 e) a cross-section image with Burgers vector $g = (0002)$ is displayed, making visible screw and mixed type threading dislocations. They already thread through the AlN template and continue through the first SL periods. After a few nanometers, the contrast changes indicating that these later grown layers exhibit a high amount of defects.

The fast Fourier transform (FFT) filtered HRTEM micrograph in Fig. 9 taken from the upper part of the AlBGaN SL confirms the c-direction alignment of the lattice also visible in selective area electron diffraction investigation.

It is again evident that the sharp tilted AlBGaN/AlN interfaces in the upper part of the SL stack are not originating from a tilting of lattice planes [11] but are caused by

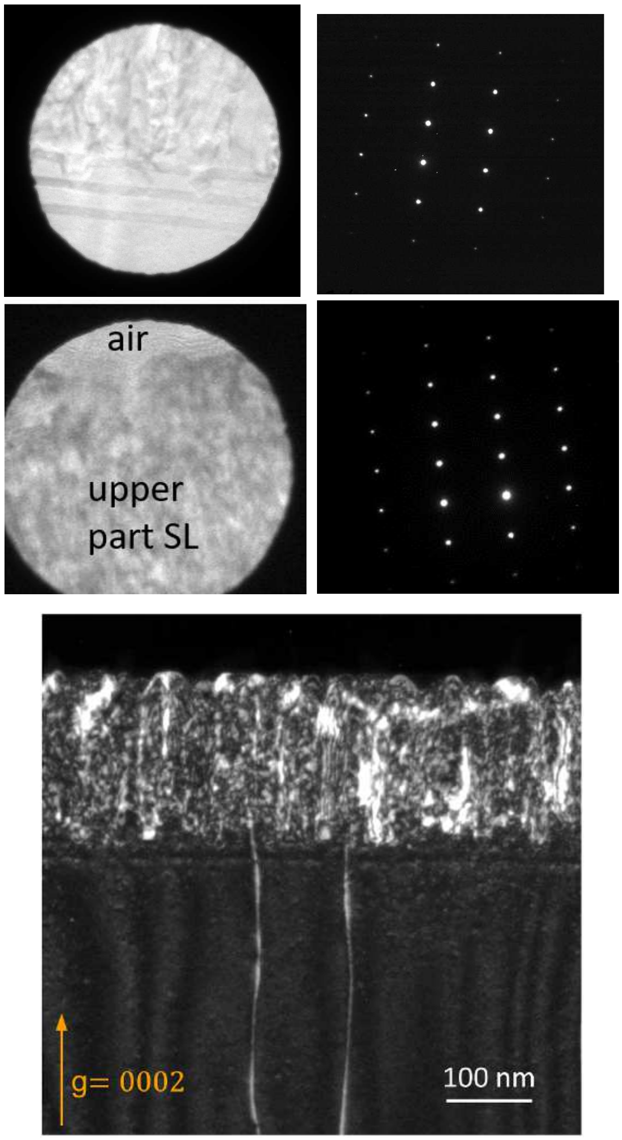

Fig. 8: SAED of the lower (top 2 images) and the upper (middle 2 images) part of the SL stack and WBDF (bottom image) investigation on the growth of the AlBGaN/AlN SL.

formation of tilted facets with higher Miller indices during growth. Additionally, many inserted half-planes can be seen in the micrograph, forming edge-type dislocations with Burgers vector in (0002) direction and propagation in the a-direction. Above those defects, planes are slightly bent to compensate for the mismatch caused by underlying defects. The vertical line defects illustrated in Fig. 9 (b) correspond to stacking faults, which are terminated by partial defects [15]. We do not attribute these defects to the occurrence of columnar-like growth, because their distance is much smaller than the observed column size [13]. Possibly more favourable tilted facets observed in the superlattice structure in Fig. 8 lead to the formation of grains and 3D growth.

These investigations show that by the superlattice approach overgrowing thin layers of AlBGaN by 10 nm of AlN, 3D growth can not be prevented. However, in this sample no

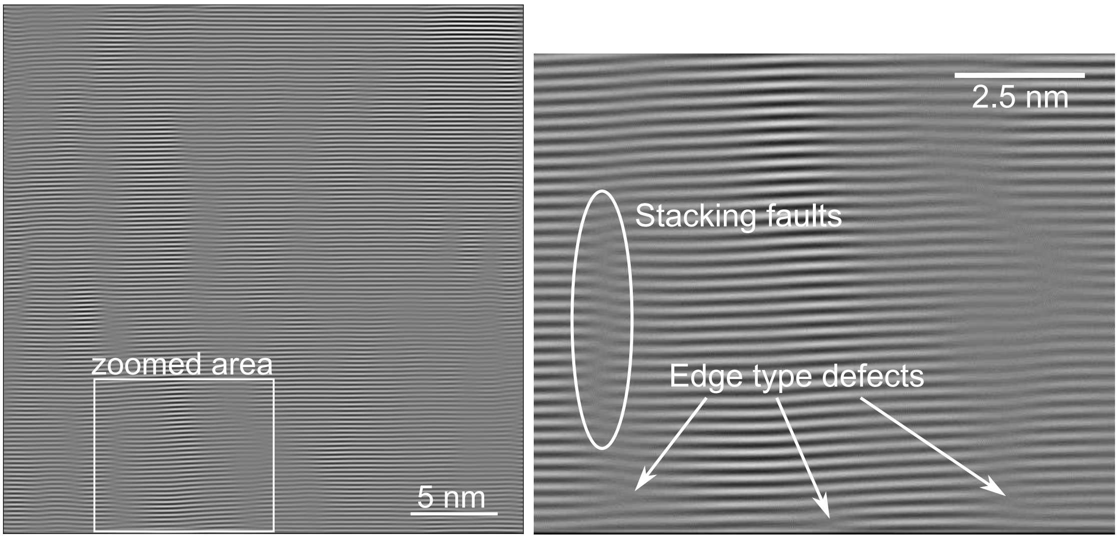

Fig. 9: FFT filtered HRTEM image (left) and therein indicated zoomed area (right) of the upper part (upper 20 nm) of the AlBGaN/AlN superlattice structure. Some planes end, forming horizontal edge-type dislocations. Vertical defect lines correspond to stacking faults with partial dislocations at their ends.

phase separation with formation of amorphous regions was found in TEM. This is possibly related to the decrease in boron content leading to better crystalline quality. Additionally, growing only 7 nm of B-containing material followed by 10 nm of AlN and the presence of Ga might delay the appearance of amorphous phases.

4. Conclusion

For the growth of AlBN and AlBGaN layers, we have observed the development of 3D growth. No correlation between the density of the grains and the threading dislocation density could be seen. Even when separating thin B containing layers by pure AlN, 3D growth is observed after a few superlattice periods, which results in inclined facets. For the growth of thin AlBGaN layers from 5–20 nm, good PL yields were observed with no sign of degradation. Also smooth layers with predominantly 2D growth behaviour were observed in AFM measurements. However, small grain-like features develop starting from thicknesses of 10 nm. Their density is increasing with thickness, and their size matches the diameter of the columns previously observed for AlBN. Since no degradation of the PL intensity occurs, these 3D features do not seem to strongly affect the crystalline quality. For optimized growth conditions, AlBGaN layers show a PL peak intensity about half of that of corresponding B-free AlGaN layer.

Acknowledgment

I thank the coauthors N. Steiger, J.-P. Scholz, S. Bauer, M. Hocker, and K. Thonke of the Institute of Quantum Matter, Semiconductor Physics Group at Ulm University for optical characterization and help with AFM, XRD and CL spectroscopy, Y. Li, H. Qi, J. Biskupek, and U. Kaiser of the Central Facility of Electron Microscopy at Ulm University for performing TEM analysis, and T. Hubáček and M. Zíková of the Institute of Physics, Czech Academy of Sciences, Prague, Czech Republic for their scientific support with epitaxy, AFM and XRD. This work is financially supported by the Deutsche Forschungsgemeinschaft (DFG). We thank Probion Analysis (Bagneux, France) for the SIMS investigations.

References

[1] S.O. Kasap and P. Capper (Eds.), *Springer Handbook of Electronic and Photonic Materials*, New York: Springer, 2006.

[2] T. Takano, T. Mino, J. Sakai, N. Noguchi, K. Tsubaki, and H. Hirayama, "Deep-ultraviolet light-emitting diodes with external quantum efficiency higher than 20 % at 275 nm achieved by improving light-extraction efficiency", *Appl. Phys. Express*, vol. 10, pp. 031002-1–4, 2017.

[3] M. Kneissl, T. Kolbe, C. Chua, V. Kueller, N. Lobo, J. Stellmach, A. Knauer, H. Rodriguez, S. Einfeldt, Z. Yang, N.M. Johnson, and M. Weyers, "Advances in group III-nitride-based deep UV light-emitting diode technology", *Semicond. Sci. Technol.*, vol. 26, pp. 014036-1–6, 2011.

[4] S. Sakai, Y. Ueta, and Y. Terauchi, "Band gap energy and band lineup of III-V alloy semiconductors incorporating nitrogen and boron", *Jpn. J. Appl. Phys.*, vol. 32, pp. 4413–4417, 1993.

[5] K. Shimada, T. Sota, and K. Suzuki, "First-principles study on electronic and elastic properties of BN, AlN, and GaN", *J. Appl. Phys.*, vol. 84, pp. 4951–4958, 1998.

[6] A. Nagakubo, H. Ogi, H. Sumiya, K. Kusakabe, and M. Hirao, "Elastic constants of cubic and wurtzite boron nitrides", *Appl. Phys. Lett.*, vol. 102, pp. 241909-1–5, 2013.

[7] X. Li, S. Wang, H. Liu, F.A. Ponce, T. Detchprohm, and R.D. Dupuis, "100-nm thick single-phase wurtzite BAlN films with boron contents over 10 %", *Phys. Status Solidi B*, vol. 254, pp. 1600699-1–5, 2017.

[8] C.H. Wei and J.H. Edgar, "Unstable composition region in the wurtzite $B_{1-x-y}Ga_x Al_yN$ system", *J. Cryst. Growth*, vol. 208, pp. 179–182, 2000.

[9] T. Kimura and T. Matsuoka, "Calculation of phase separation in wurtzite $In_{1-x-y-z} Ga_xAl_yB_zN$", *Jpn. J. Appl. Phys.*, vol. 46, pp. L574–L576, 2007.

[10] M.A. Moram and M.E. Vickers, "X-ray diffraction of III-nitrides", *Reports on Progress in Physics*, vol. 72, pp. 036502-1–40, 2009.

[11] T. Akasaka and T. Makimoto, "Flow-rate modulation epitaxy of wurtzite AlBN", *Appl. Phys. Lett.*, vol. 88, pp. 041902-1–3, 2006.

[12] A.Y. Polyakov, M. Shin, W. Qian, M. Skowronski, D.W. Greve, and R.G. Wilson, "Growth of AlBN solid solutions by organometallic vapor-phase epitaxy", *J. Appl. Phys.*, vol. 81, pp. 1715–1719, 1997.

[13] O. Rettig, "Investigation of AlBN Grown by MOVPE", *Annual Report 2016*, pp. 59–66, Ulm University, Institute of Optoelectronics.

[14] X. Li, S. Sundaram, Y. El Gmili, T. Moudakir, F. Genty, S. Bouchoule, G. Patriarche, R.D. Dupuis, P.L. Voss, J.P. Salvestrini, and A. Ougazzaden, "BAlN thin layers for deep UV applications", *Phys. Status Solidi A*, vol. 212, pp. 745–750, 2015.

[15] Y. Li, H. Qi, T. Meisch, M. Hocker, K. Thonke, F. Scholz, and U. Kaiser, "Formation of I_2-type basal-plane stacking faults in $In_{0.25}Ga_{0.75}N$ multiple quantum wells grown on a (101-1) semipolar GaN template", *Appl. Phys. Lett.*, vol. 110, pp. 022105-1–4, 2017.

[16] M. Zhang and X. Li, "Structural and electronic properties of wurtzite $B_xAl_{1-x}N$ from first-principles calculations: structural and electronic properties of wurtzite $B_xAl_{1-x}N$", *Phys. Status Solidi B*, vol. 254, pp. 1600749-1–8, 2017.

[17] A. Said, M. Debbichi, and M. Said, "Theoretical study of electronic and optical properties of BN, GaN and $B_xGa_{1-x}N$ in zinc blende and wurtzite structures", *Optik – International Journal for Light and Electron Optics*, vol. 127, pp. 9212–9221, 2016.

[18] B.E. Gaddy, Z. Bryan, I. Bryan, J. Xie, R. Dalmau, B. Moody, Y. Kumagai, T. Nagashima, Y. Kubota, T. Kinoshita, A. Koukitu, R. Kirste, Z. Sitar, R. Collazo, and D.L. Irving, "The role of the carbon-silicon complex in eliminating deep ultraviolet absorption in AlN", *Appl. Phys. Lett.*, vol. 104, pp. 202106-1–4, 2014.

[19] K.B. Nam, M.L. Nakarmi, J.Y. Lin, and H.X. Jiang, "Deep impurity transitions involving cation vacancies and complexes in AlGaN alloys", *Appl. Phys. Lett.*, vol. 86, pp. 222108-1–3, 2005.

[20] P. Kamyczek, E. Placzek-Popko, V. Kolkovsky, S. Grzanka, and R. Czernecki, "A deep acceptor defect responsible for the yellow luminescence in GaN and AlGaN", *J. Appl. Phys.*, vol. 111, pp. 113105-1–7, 2012.

[21] S.F. Chichibu, H. Miyake, Y. Ishikawa, M. Tashiro, T. Ohtomo, K. Furusawa, K. Hazu, K. Hiramatsu, and A. Uedono, "Impacts of Si-doping and resultant cation vacancy formation on the luminescence dynamics for the near-band-edge emission of $Al_{0.6}Ga_{0.4}N$ films grown on AlN templates by metalorganic vapor phase epitaxy", *J. Appl. Phys.*, vol. 113, pp. 213506-1–6, 2013.

[22] S. Wang, X. Li, A.M. Fischer, T. Detchprohm, R.D. Dupuis, and F.A. Ponce, "Crystal structure and composition of BAlN thin films: effect of boron concentration in the gas flow", *J. Cryst. Growth*, vol. 475, pp. 334–340, 2017.

InGaN Heterostructures as Optical Transducers for Hydrogen Sensing

Jassim Shahbaz

GaN/InGaN quantum wells were investigated as optical transducers for the detection of hydrogen. The heterostructure sensors were grown by metal organic vapour phase epitaxy and later covered by a thin layer of Pt by electron beam evaporation. The quantum well photoluminescence is sensitive to changes in the sensor surface potential and this characteristic is used as the detection principle. With the adsorption of hydrogen at the Pt/GaN interface, downward near-surface band bending results in an increase in the quantum-confined Stark effect producing a red-shift in the luminescence. A reduction in photoluminescence intensity is also observed due to the separation of the electron and hole wave functions. Some samples have shown opposite trends based on different surface treatments and those result are under investigation. Further studies are in progress to see whether this phenomenon also allows the detection of hydrides such as hydrogen sulfide, an important gas present in the human breath for early detection of diseases.

1. Introduction

Group-III nitrides have well known material properties that make them suitable for applications in biochemical sensing [1–4]. Specifically, GaN has the capacity to operate at high temperatures hence it can be used to realize Schottky diode and field effect transistor (FET) gas sensors which can be used in harsh environmental conditions [5–7]. Due to its surface being highly electrochemically stable [7, 8], GaN can also be applied in the field of biochemical sensors in liquid electrolytes [9–12]. The material also has good optoelectronic properties that can be utilized in the creation of novel sensors which produce an optical readout signal. Since this optical signal can be processed remotely the sensor can be used in situations where destructive chemicals would make electrical contacting a complicated endeavour.

GaN based gas sensors investigatd in this study work on the principle of near-surface band bending due to the adsorption of gas or biomolecules at the sensor surface. This produces a change in the surface potential and the Fermi level pinning. N-doped GaN in air has been reported to have a near-surface upward band bending of about 1 eV [13]. This somewhat compensates the quantum-confined Stark effect (QCSE) present due to internal stress in the near-surface GaInN quantum well (QW). When a reducing agent like hydrogen gets adsorbed at the sensor surface it produces downward band bending since it donates an electron to the semiconductor surface [14]. This results in an increase of the QCSE and a red-shift in the PL emission of the QW, while an oxidizing agent which accepts an electron from the surface will induce a blue-shift [15].

This study is concerned with characterizing GaN/InGaN QW grown on optically transparent sapphire substrates and capped by a thin Pt layer for selectivity purposes. Chemically induced changes to the surface potential alter the PL emission of the QW. This effect is then used to demonstrate hydrogen gas sensing by inducing a change in the PL wavelength and intensity.

2. Experimental Details

The semiconductor heterostructures investigated in this work were grown in Aixtron AIX200/RF, a commercial horizontal flow metal organic vapour phase epitaxy (MOVPE) reactor. Ammonia (NH_3), trimethylgallium (TMGa), trimethylaluminum (TMAl), triethylgallium (TEGa), and trimethylindium (TMIn) are the precursors for the epitaxial growth. Ultra-pure hydrogen and nitrogen act as carrier gases. Growth takes place on a 2 inch *c*-oriented 0.2° off m-axis double-side polished (DSP) sapphire wafer. Firstly, a 10 nm thick AlN nucleation layer is grown for better quality GaN growth. This is followed by an undoped Ga-polar GaN buffer layer with a thickness of about 2 µm. Then a series of samples with a single 3 nm thick InGaN QW was grown with a GaN capping layer of different thickness, i.e., 3, 6, 9 and 15 nm at the top (Fig. 1). Another series with higher background doping concentration ($\approx 1 \cdot 10^{18}\,\mathrm{cm}^{-3} - 1 \cdot 10^{19}\,\mathrm{cm}^{-3}$) of the GaN buffer layer was also investigated, as simulation results had shown better sensitivity with higher carrier concentration [16]. To functionalize the sensor surface for hydrogen detection, a layer of Pt with thickness of 3, 6 and 9 nm was grown on top of these samples using electron beam evaporation.

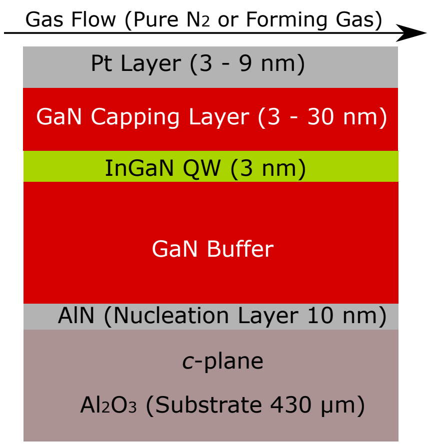

Fig. 1: InGaN/GaN semiconductor heterostructure. Capping layers of different thickness were used for these measurements.

For the optical characterization of the QW, a photoluminescence setup (Fig. 2) was built specifically for gas sensing measurements. It consists of a sealed chamber with a sample holder used for backside excitation of the sample through a glass window with AR coating. The chamber is connected to a gas mixing apparatus which is in turn connected to nitrogen and forming gas (95 % nitrogen and 5 % hydrogen mixture) supply, forming gas being used as a source of hydrogen. The PL emission changes in response to the cyclic switching of ambient gases and is recorded continuously. A blue laser with a wavelength of 405 nm is used for the excitation of the QW with PL emission around 465 nm, and the read-out of the PL spectra is performed through the same path as the excitation. A dichroic mirror with a cut-off wavelength of 425 nm separates the excitation from the PL signal. Finally a monochromator in combination with a CCD camera is used to spectrally resolve and record the QW emission signal.

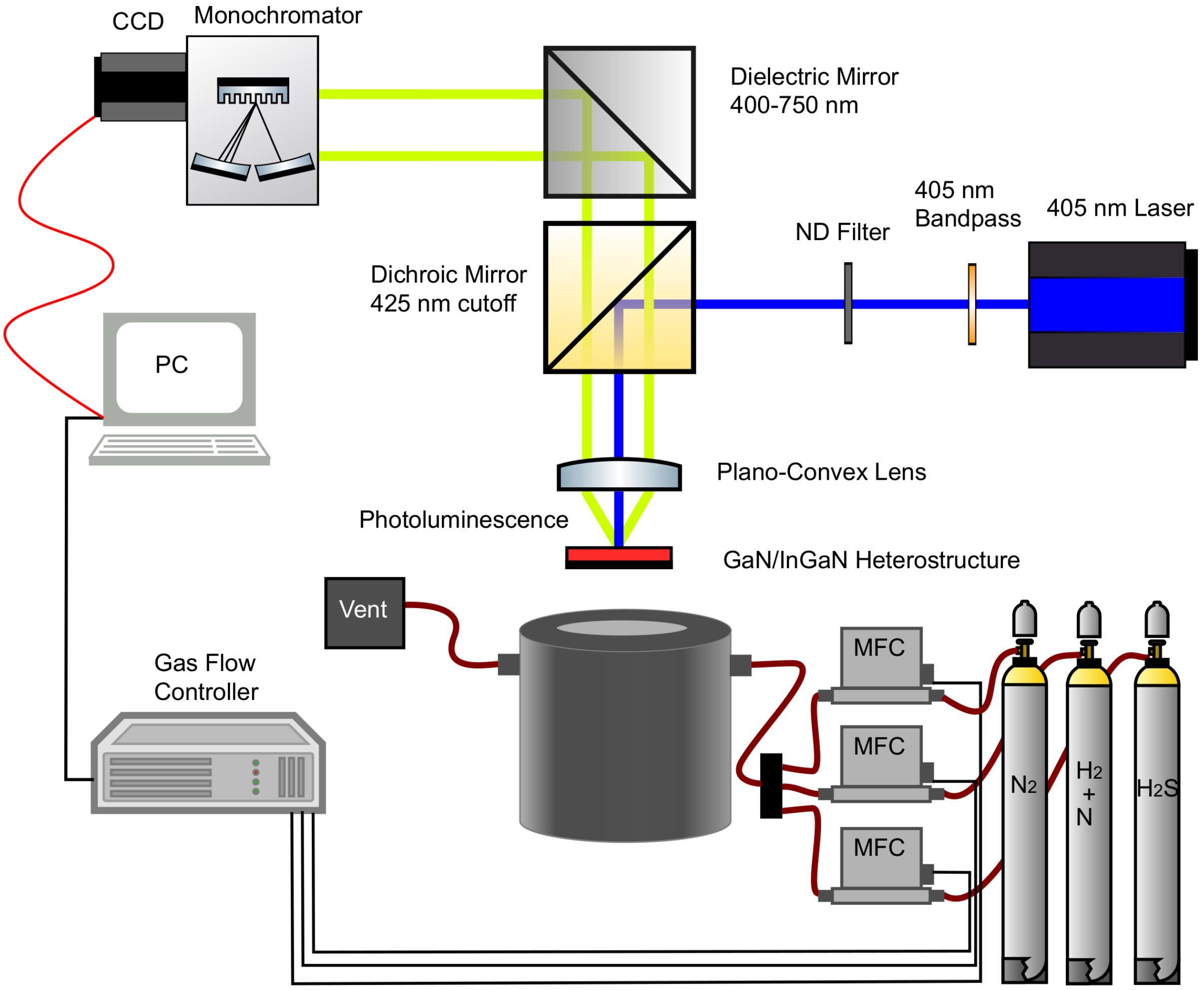

Fig. 2: Optical gas sensing setup: A blue laser is focused onto the GaN/InGaN heterostructure through an optical system consisting of a plano-convex lens and a dichroic mirror which separates the laser and the PL emission. A dielectric mirror reflects the collimated PL emission into a monochromator. The sealed chamber is connected to a gas mixing setup with a supply of nitrogen, hydrogen and hydrogen sulfide.

3. Gas Sensing Results and Discussion

Gas sensing was performed first for the planar single InGaN quantum well samples. The parameter investigated in this case was the thickness of the GaN capping layer as that has a direct impact on the responsiveness of the sensor. The influence of gases on the

QW emission was measured by alternatively letting pure nitrogen and then hydrogen (in 95 % nitrogen) flow through the gas chamber in intervals of 2 min. Hydrogen being an electron donor will induce a downward near-surface band bending for n-GaN, increasing the QCSE. Stronger QCSE produces a red-shift in the PL emission along with a reduction of the electron–hole wave function overlap resulting in lowered intensity.

Earlier simulation and experimental results reported in [17] have shown a higher sensitivity with a thinner cap layer. However, the PL emission intensity of samples with thin cap layer suffers considerably with the deposition of a Pt layer. It is assumed that the smaller barrier results in tunnelling transport of electrons out of the QW towards the metal-coated surface. Further investigations will be done to optimise the cap layer thickness where the PL intensity is still measurable.

In Fig. 3 the sensor response of a sample with 15 nm GaN cap with different Pt layer thickness is plotted. When switching from nitrogen to hydrogen a red-shift along with a decrease in PL intensity is observed the mechanism for which is described above. Ignoring the one spike when switching from hydrogen to nitrogen with the 3 nm Pt, the sensor response does not seemingly change much with the thickness of the metal layer for a single QW sample. It remains between 3–6 meV here and in several other measurements. The result for the intermediate thickness of 6 nm have shown some inconsistency and are being investigated further.

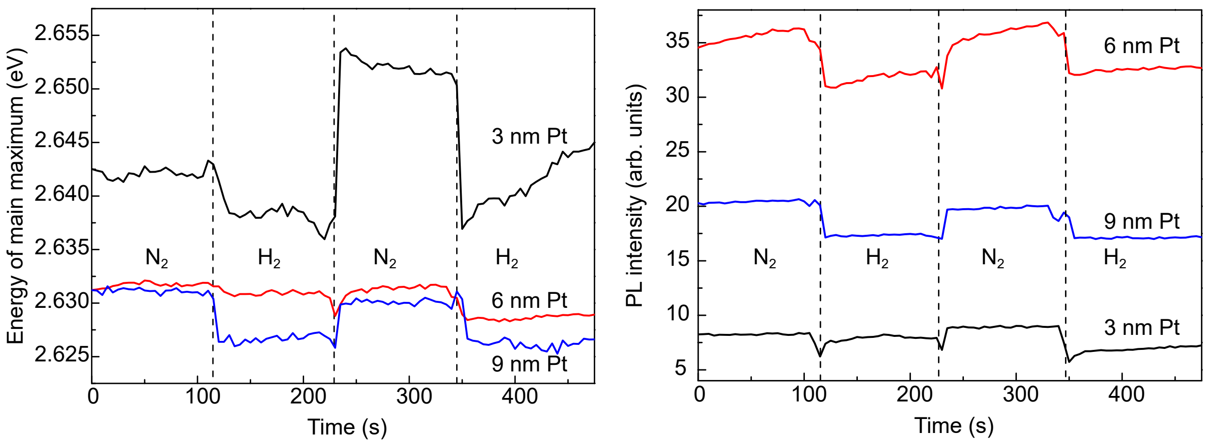

Fig. 3: The change in PL emission energy (left) and intensity (right) of a single QW sample with GaN cap layer thickness of 15 nm under nitrogen and hydrogen ambient. The gases were cyclically switched after 2 min intervals. A red-shift and decrease in PL intensity is observed when switching from nitrogen to hydrogen.

Simulation results [16] indicate a thinner capping layer along with higher background doping makes the sensor more sensitive. A series of samples with different doping ($\approx 1\cdot10^{18}\,\mathrm{cm}^{-3}$–$1\cdot10^{19}\,\mathrm{cm}^{-3}$) was grown and gas sensing measurements done for a comparison with simulated data. The results as seen in Fig. 4 show a nice correlation between the calculated (left) and the experimental (right) data. In both cases lower doping has a flatter response regardless of the cap layer thickness, while higher doping produces a large wavelength shift with a thin cap but the shift falls sharply with increasing cap thickness.

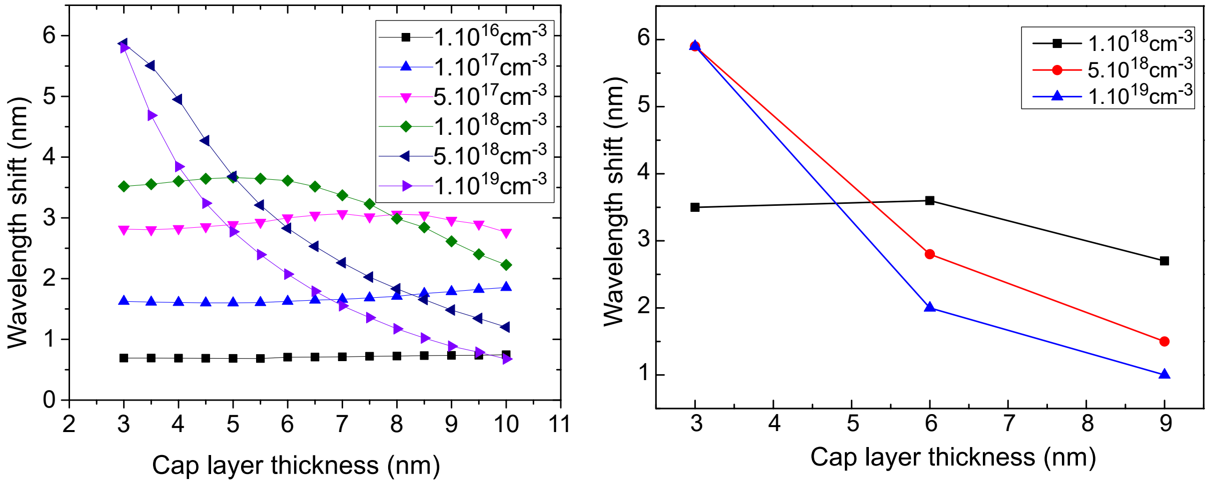

Fig. 4: Wavelength shift vs. GaN cap layer thickness. Simulation results have shown a larger wavelength shift with higher background doping concentration (left), this has experimentally been confirmed as samples with three different doping concentrations were grown and gas sensing performed, higher doping produced larger shift in emission wavelength (right).

Up to now gas sensing was performed with single QW samples to keep the PL emission simpler to understand. However, since the emission intensity for a single QW when combined with a platinum layer becomes rather weak or even undetectable in some cases, a 5 QW sample was also tested. This sample was recently cleaned with Piranha solution and deposited with a Pt layer. Piranha etching hydroxylates the surface, the OH^- groups produce an upward near-surface band bending.

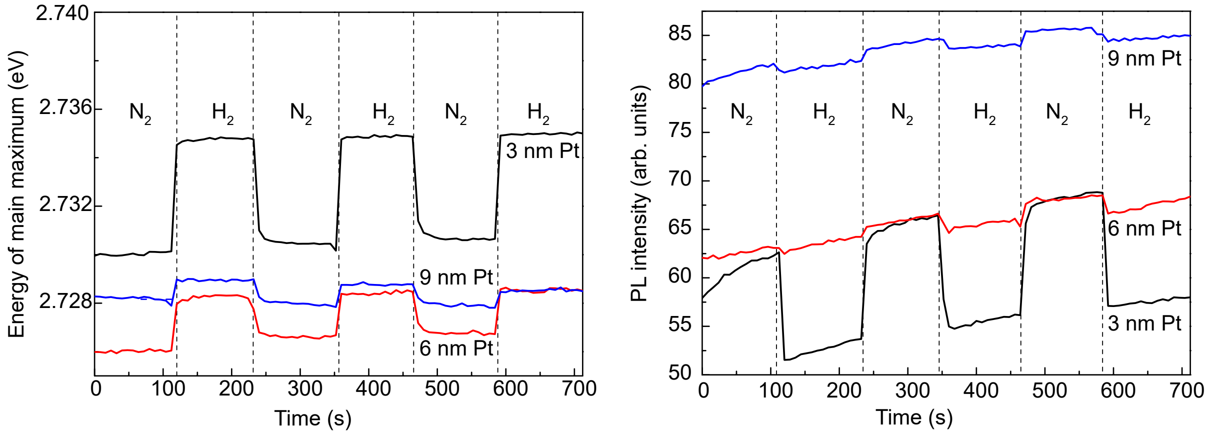

Fig. 5: The change in PL emission energy (left) and intensity (right) of a 5 QW sample with GaN cap layer thickness of about 9 nm under nitrogen and hydrogen ambient for different Pt layer thickness.

With the adsorption of hydrogen downward band bending should follow but instead of the expected red-shift a blue-shift is observed with a decrease in the PL intensity as seen in Fig. 5. This trend is not limited to the multiple QW but was also seen in single QW samples which have been freshly cleaned and deposited with Pt layer and tested within a day. Here time could be a factor in defining the sensing behaviour and will be investigated further.

The upward band bending counteracts the QCSE, so a blue-shift should also increase the radiation transition probability. However, the decreasing PL intensity points towards another mechanism counteracting the radiative recombination. One possible reason for this could be the enhanced tunnelling of photoexcited electron–hole pairs out of the QW, the reason for which is under investigation. This phenomenon will be verified with simulation data to better understand the bandgap changes under different conditions at the surface. However, in this case the thinner Pt layer of 3 nm gives the highest sensitivity compared to thicker layers a trend also seen in single QW samples which were cleaned with Piranha and tested for sensitivity soon after.

4. Conclusions

The effect of hydrogen adsorption on the surface of a GaN/InGaN heterostructure functionalized with a Pt layer has been investigated. For single QW samples, a red-shift and a decrease in the emission intensity is observed in accordance with an increase in the QCSE due to downward near-surface band bending. Thinner cap layer samples should in theory show higher sensitivity but suffer from increased tunnelling of the carriers to the metal-coated surface. Experimental data have confirmed theoretical calculations that higher doping concentration produces better sensitivity. Samples treated with Piranha solution form hydroxyl groups at the sensor surface and seemingly invert the sensor response to hydrogen by producing a blue-shift in emission. This phenomenon will be investigated further with accompanying simulations for a better understanding of the effects of surface chemistry on the GaN/InGaN bandgap emission. The results are nevertheless promising and the heterostructures will be improved to realize a highly selective and sensitive gas sensor.

Acknowledgment

Most of the work presented here has been done within the master thesis project of Y. Liao. The scientific and technical support provided by M. Schneidereit, J.P. Scholz, O. Rettig, I. Lamparter, R. Blood, R. Rösch and T. Zwosta (Institute of Optoelectronics, Ulm University) as well as F. Huber, S. Bauer, and K. Thonke (Institute of Quantum Matter, Ulm University) is gratefully acknowledged. This work is financially supported by the Deutsche Forschungsgemeinschaft (DFG) within the PULMOSENS project "Semiconductor-based nano structures for the highly sensitive optical analysis of gases and bio-materials".

References

[1] O. Weidemann, P.K. Kandaswamy, E. Monroy, G. Jegert, M. Stutzmann, and M. Eickhoff, "GaN quantum dots as optical transducers for chemical sensors", *Appl. Phys. Lett.*, vol. 94, pp. 113108-1–3, 2009.

[2] D. Heinz, F. Huber, M. Spiess, M. Asad, L. Wu, O. Rettig, D. Wu, B. Neuschl, S. Bauer, Y. Wu, S. Chakrabortty, N. Hibst, S. Strehle, T. Weil, K. Thonke, and F. Scholz, "GaInN quantum wells as optochemical transducers for chemical sensors and biosensors", *IEEE J. Select. Topics Quantum Electron.*, vol. 23, pp. 1900109-1–9, 2017.

[3] J. Teubert, P. Becker, F. Furtmayr, and M. Eickhoff, "GaN nanodiscs embedded in nanowires as optochemical transducers", *Nanotechnology*, vol. 22, pp. 275505-1–5, 2011.

[4] S.J. Pearton, F. Ren, Y.L. Wang, B.H. Chu, K.H. Chen, C.Y. Chang, W. Lim, J. Lin, and D.P. Norton, "Recent advances in wide bandgap semiconductor biological and gas sensors", *Prog. Mater. Sci.*, vol. 55, pp. 1–59, 2010.

[5] J. Schalwig, G. Müller, U. Karrer, M. Eickhoff, O. Ambacher, M. Stutzmann, L. Görgens, and G. Dollinger, "Hydrogen response mechanism of Pt–GaN Schottky diodes", *Appl. Phys. Lett.*, vol. 80, pp. 1222–1224, 2002.

[6] J. Schalwig, G. Müller, M. Eickhoff, O. Ambacher, and M. Stutzmann, "Gas sensitive GaN/AlGaN-heterostructures", *Sens. Actuators B*, vol. 87, pp. 425–430, 2002.

[7] J. Schalwig, G. Müller, M. Eickhoff, O. Ambacher, and M. Stutzmann, "Group III-nitride-based gas sensors for combustion monitoring", *Mater. Sci. Eng. B*, vol. 93, pp. 207–214, 2002.

[8] Y.L. Wang, F. Ren, U. Zhang, Q. Sun, C.D. Yerino, T.S. Ko, Y.S. Cho, I.H. Lee, J. Han, and S.J. Pearton, "Improved hydrogen detection sensitivity in N-polar GaN Schottky diodes", *Appl. Phys. Lett.*, vol. 94, pp. 212108-1–3, 2009.

[9] M. Stutzmann, J.A. Garrido, M. Eickhoff, and M.S. Brandt, "Direct biofunctionalization of semiconductors: a survey", *Phys. Status Solidi A*, vol. 203, pp. 3424–3437, 2006.

[10] S. Paul, A. Helwig, G. Müller, F. Furtmayr, J. Teubert, and M. Eickhoff, "Opto-chemical sensor system for the detection of H_2 and hydrocarbons based on InGaN/GaN nanowires", *Sens. Actuators B*, vol. 173, pp. 120–126, 2012.

[11] G. Steinhoff, M. Hermann, W.J. Schaff, L.F. Eastman, M. Stutzmann, and M. Eickhoff, "pH response of GaN surfaces and its application for pH-sensitive field-effect transistors", *Appl. Phys. Lett.*, vol. 83, pp. 177–179, 2003.

[12] H.T. Wang, B.S. Kang, F. Ren, S.J. Pearton, J.W. Johnson, P. Rajagopal, J.C. Roberts, E.L. Piner, and K.J. Linthicum, "Electrical detection of kidney injury molecule-1 with AlGaN/GaN high electron mobility transistors", *Appl. Phys. Lett.*, vol. 91, pp. 222101-1–3, 2003.

[13] I. Cimalla, F. Will, K. Tonisch, M. Niebelschütz, V. Cimalla, V. Lebedev, G. Kittler, M. Himmerlich, S. Krischok, A.J. Schaefer, M. Gebinoga, A. Schober, T. Friedrich, and O. Ambacher, "AlGaN/GaN biosensor—effect of device processing steps on the

surface properties and biocompatibility", *Sens. Actuators B*, vol. 123, pp. 740–748, 2007.

[14] M. Foussekis, A.A. Baski, and M.A. Reshchikov, "Photoadsorption and photodesorption for GaN", *Appl. Phys. Lett.*, vol. 94, pp. 162116-1–3, 2009.

[15] Z. Zhang, J.T. Yates Jr.,"Band bending in semiconductors: chemical and physical consequences at surfaces and interfaces", *Chem. Rev.*, vol. 112, pp. 5520–5551, 2012.

[16] P. Iskander, *Chemical Sensors Based on GaN Heterostructures*. Bachelor Thesis, Ulm University, Ulm, Germany, 2017.

[17] J. Shahbaz, M. Schneidereit, B. Hörbrand, S. Bauer, K. Thonke, and F. Scholz, "Optimising InGaN heterostructures for bio and gas sensors", in Proc. *Europ. Workshop on Metalorganic Vapor Phase Epitaxy, EW-MOVPE17*, pp. 118–122. Grenoble, France, June 2017.

Improved Functionalization of InGaN Sensor Structures

Martin F. Schneidereit

This report presents continued work on the functionalization of InGaN quantum well structures for biochemical sensing. Previous work of our group had shown functionalization of GaN surfaces for selective ferritin binding via microstamping. The contrast of fluorescence micrographs was low due to strong unspecific binding of the ferritin complex to non-functionalized InGaN areas. The microstamping technique is improved to achieve maximal contrast and thus lowest unspecific binding. An alternative techique of microdrop casting is introduced to encounter possible drawbacks of microstamping.

1. Introduction

Since their breakthrough over the last decades gallium nitride (GaN) and its alloys indium gallium nitride (InGaN) and aluminium gallium nitride (AlGaN) have been established as the gold standard for short wavelength visible light emitting diodes (LEDs). Because of its high bandgap, it has also gained increased interest as a base material for high-power electronics [1]. Due to its chemical stability and temperature resistance [2, 3] it is also well-suited for extreme environments as has been shown by various groups [4]. In biological environments, chemical inertness is a crucial parameter to minimize interaction with the respective specimens like cells or enzymes. It has been shown by our group that biochemical sensors can be made of GaN with a purely optical readout by making use of the quantum-confined Stark effect (QCSE) [5]. One big advantage of this approach is the possibility to remotely excite and analyze the structure to make use of InGaN's high stability. The photoluminescence (PL) of InGaN quantum wells (QWs) located closely to the surface of a GaN bulk layer shows sensitivity to surface-related potential changes. When (macro-)molecules are adsorbed on the surface, they eventually give rise to surface charges and thus create a zone of near-surface band-bending. The QWs are affected by the resulting field and their luminescence spectrum is changed in intensity and energy position (QCSE). This shift can be used to evaluate the potential change on the surface of the GaN layer.

In sensor theory, selectivity is just as important as is the sensitivity of a system. The detection process of the above mentioned effect is highly non-selective, as it is purely electronic. Various molecules may adsorb to GaN with different affinities but the change of the sensor signal cannot be attributed to a single substance. In order to increase the selectivity, a functionalization layer can be attached to the surface of the sensor. Different standard techniques exist in biochemistry, but each one has to be established for a new material to work in the most effective way. For GaN, various groups have shown different functionalization techniques [6, 7].

In previous work of our group, the functionalization of InGaN QWs has been pursued, and a preferred attachment of ferritin molecules to functionalized areas could be demonstrated. The interaction chosen for our sensor system is the biotin-streptavidin interaction, which is one of the strongest, non-covalent reactions in biochemistry (dissociation constant $K_\mathrm{d} \approx 4 \cdot 10^{14}$ mol/l) [8]. Biotin (also known as vitamin B7) is involved in the synthesis of fatty acids and for the transformation of certain non-carbohydrates into sugar (gluconeogenesis). However for the first experiments, the contrast between functionalized and non-functionalized surfaces was low due to strong unspecific binding to the surface. In this report, our studies to improve the situation are presented.

2. Basic Functionalization Procedure

In previous work, functionalization has been shown by our project group [9], with position-selective binding of a ferritin-biotin-rhodamine (FBR) complex being demonstrated. The process has several steps as will be discussed below (compare Fig. 1).

In order to enable a binding of our analyte (ferritin), the first step is to create OH-groups on the GaN surface. This can be done by either annealing the sample in an oxygen plasma asher for 30–60 min at 100 W or by dipping it into a solution of hydrogen peroxide with sulfuric acid ($H_2O_2 : H_2SO_4$ in 1:3) for 10 min (piranha solution). The OH-groups then enable covalent binding of the PEG-silane-biotin complex with its Si-group. This is done in a way to create areas of silane functionalization and areas without. This way, in a later sensing analysis, the response of the system can be analyzed with respect to different regions to compare the shift introduced by the biomolecules. After incubating the silane complex for 15 min, streptavidin (strp) is added to the surface and incubated for 30–60 min. Biotin fits into one of four binding pockets of strp, where it is (among others) fixed with hydrogen bonds and van der Waals interaction [10]. Strp has 4 binding sites for biotin, which enables the last step of the process: Attaching the FBR-complex to the remaining binding sites of strp (incubation time: 30–60 min). After each subsequent step, thorough washing is performed, to reduce non-specific binding of the complexes to the GaN surface.

After deposition, the sensor sample is analyzed in a fluorescent microscope. The FBR-complex is visible due to rhodamine, which is a fluorescent dye commonly used in biochemistry. After analysis of the pattern, the sample can be put into our project's automated micro-PL setup. With this setup, a PL map can be created, where every pixel corresponds to a measured PL spectrum. The emission of the QW is analyzed with a center of mass method to determine the center wavelength. In order to be able to refer both methods to one another, gold markers are deposited prior to all experiments on the GaN structure. This way, a reference system is created to compare both techniques at the same positions.

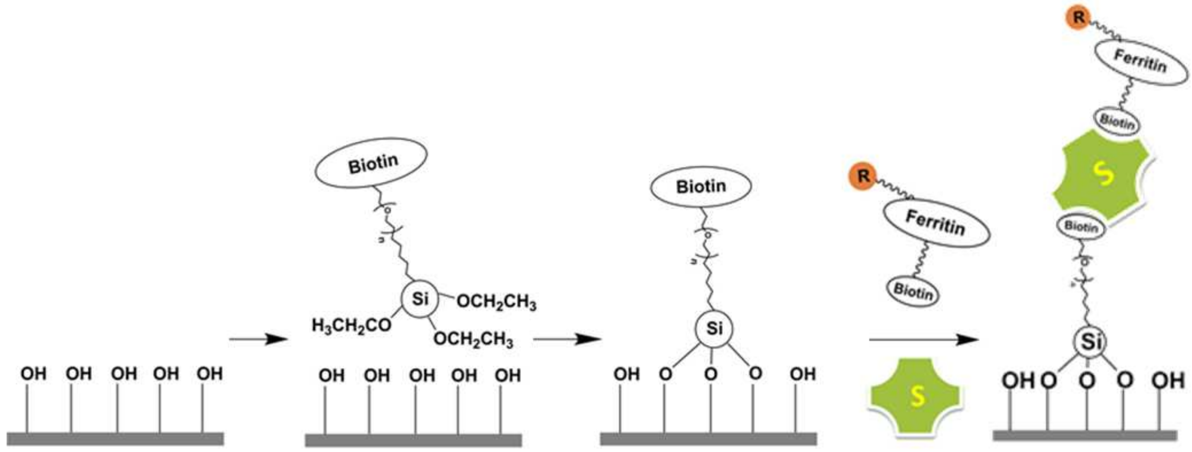

Fig. 1: The functionalization process shown in steps: The hydroxilated GaN surface enables covalent binding of the PEG-silane-complex. The second step creates a binding between strp (S) and biotin of the PEG-silane. In the last step, the same interaction is used for binding the FBR-complex to the free binding sites of strp. The dark dot (R) indicates rhodamine.

3. Surface Pattering Techniques

3.1 Microcontact printing

The technique used in most of our experiments is microstamping: A silicon wafer structured by photolithography is used to mold polydimethylsiloxane (PDMS) polymer into a high-low-pattern. A holder is attached, and after drying, the polymer can be carefully released from the wafer to create the inverse stamping pattern of the wafer. The stamp is then vapor-loaded with the respective silane in a glass cylinder for 30 min (compare [9]). Thin layers of silane can thus be expected to be deposited on the stamp and thus later on the substrates. For the stamping process itself, a dip-coating machine is used, which provides a constant up- or down-movement. The force which is applied to the structure is regulated with a spring-dampened base-plate, on which the sample is fixed during the process. This way, the time of lowering the stamp is proportional to the downward force of the stamp. Stamping provides a very directed deposition of the silanes onto GaN and incubation after stamping is not necessary anymore. On the other hand, the time required for loading the stamp with silane takes 30–60 min, and the PDMS material shows a soaking effect, which deteriorates the stamp after few uses and requires new stamps to be made.

3.2 Microdrop casting

The second technique used in this work is the technique of microdrop casting: A commercial, piezo-driven nozzle with a diameter of few micrometers shoots drops of $\approx 200\,\mathrm{pl}$ at a repetition rate of up to 1 kHz. The deposited amount can be regulated precisely by shooting several drops on one spot before moving to the next position. The system enables homogeneous and repeatable deposition rates and well-defined molecule amounts due to possible dilution of the used solution. The main drawback of this technique is possible clogging of the nozzle with viscous molecule solutions and thus a potential timely nozzle cleaning process before every run (acetone is flushed through the system to dissolve all contaminants and to release possible clogs). After deposition and incubation of silane molecules on GaN, excess material has to be removed with supersonication for at least 1 min in deionized (DI) water.

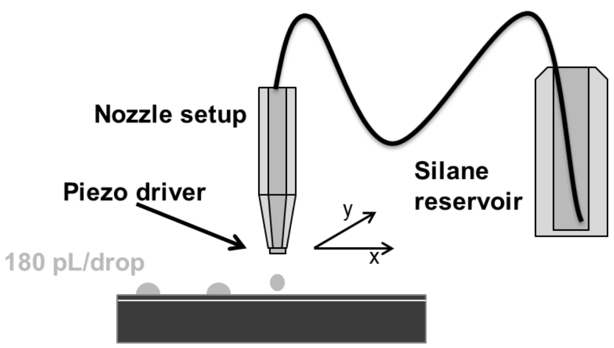

Fig. 2: Schematic of the microdrop setup: A piezo-driven nozzle shoots ≈ 200 pl/drop at a repetition rate of up to 1 kHz. A reservoir of ≈ 2 ml is connected with a tube to enable continuous operation for up to three hours. When mounted into the automated micro-PL setup, the drops can be deposited in different amounts per spot, as the system moves after each deposition.

4. Sensing Experiments

4.1 Sensing of stamped structures

As mentioned in the introduction, first functionalization results have been obtained for GaN by our project group [9]. The system used in this previous work made use of covalent bindings. 3-mercaptopropyltrimethoxysilane (MPTMS) binds to the OH-groups (hydroxy) of a prepared GaN surface. MPTMS has a functional SH-group (thiole) which binds covalently to the maleimide-group of ferritin-maleimide-complex. A big drawback of this technique is the lack of possible regeneration of the sensor surface for later experiments. In order to break the strong covalent bonding between the analyte (ferritin) and the sensor, aggressive chemistry would have to be used which also removes MPTMS. A solution to this problem is the use of a weaker interaction. The biotin-streptavidin interaction can be removed with a nonionic aqueous solution at 70 °C [8], but otherwise is very strong and stable. In order to reduce unspecific binding, the concentration of the FBR solution was reduced (previously 5 mg/ml, now 0.02 mg/ml), and a more thorough washing process was established. All constituents in the newly used process are water soluble, enabling efficient washing with Milli-Q water in an ultrasonic bath. Subsequent sonication after every step highly improved the contrast of stamped structures (compare Fig. 3). The next step was to evaluate the stamped structures via the sensor signal itself. For this, the automated micro-PL setup was used to scan over a previously selected area, where stamps as well as the gold markers could be seen (see Sect. 2). The area was scanned in steps of 50 µm and a total area of $700 \times 700\,\mu m^2$ was analyzed. For each step, a PL-spectrum was recorded. The center wavelength and the intensity of the PL signal is analyzed automatically. The corresponding results can be seen in Fig. 4: While

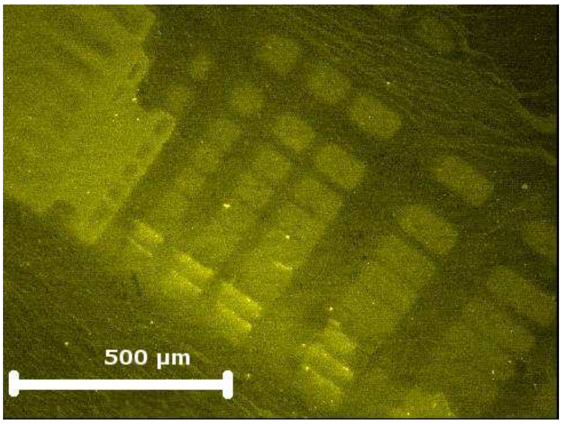

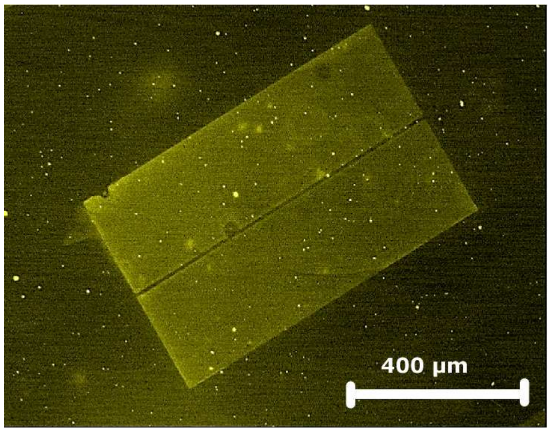

Fig. 3: Comparison between previous stamping results (left) and optimized structures with the biotin-strp interaction (right) in fluorescence micrographs: Strong nonspecific binding can be observed for the old method, the contrast between stamped areas and the GaN surface is low. For the biotin-strp, the edges of the stamped areas are clearly visible and even fine details (the 15 µm groove between both stamped bars) can be resolved.

the stamped pattern is clearly visibile alongside the gold marker in the fluorescence micrograph, the same structure cannot be seen as a sensor response in the PL-map. The color scale of the map is set according to the PL peak center energy: high (medium grey), medium (bright grey), and low (dark grey) energies. An eventual shift can be observed in the area where the groove between both stamped bars is located (double arrow). This might be attributed to a local accumulation of molecules at the groove. As the molecules are probably attached in densities close to a monolayer, the sensor response might be too small for the non-optimized sensor yet. For this reason, an alternative functionalization method via microdrops was introduced for potentially higher molecule concentrations on the sensor surface.

4.2 Functionalization of microdrops on GaN

The micropdrop setup was built to be mounted into the micro-PL setup for automated dropcasting. In this way, the sensor sample can be patterned similar to the microstamp technique. The volume of one drop is small enough to enable structure sizes of ≈ 200 µm, thus being similar to the stamped structures. In Fig. 5 an example of dropcasting on glass is shown: via a camera, the dropcasting process can be evaluated and adjusted ad-hoc. Glass was chosen as a cheap substrate for the first optimization eperiments with this new technique, as for InGaN, the glass parameters can be used and then improved. Different amounts of drops were investigated per spot. After every dropcasting procedure, the silane drops were incubated for 15 min at 40 °C and subsequently excess silane was removed by supersonication in Milli-Q water for 1 min. In the following incubation processes for streptavidin and FBR (both 0.02 mg/ml for 30 min), a humidic chamber was used to minimize drop evaporation and thus inhibit drying inhomogeneities. After strp incubation, sonication in buffer solution[2] was used to remove excess streptavidin. After

[2] 10 mM PBS (pH 7.4), 0.3 M NaCl, 0.1 % Tween20

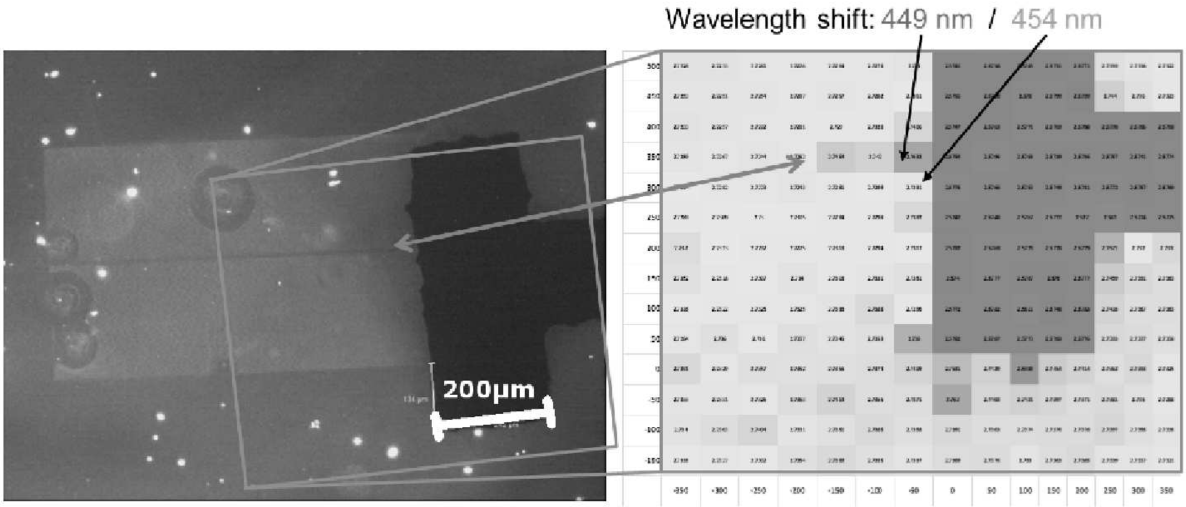

Fig. 4: A functionalized sensor area was investigated by fluorescence microscopy (left): The double-bar structure is clearly visible with high resolution and contrast. When analyzed in the micro-PL setup, there is no clear sensor response visible (right). The colorscale is set according to the PL peak center energy: high (medium grey), medium (bright grey), and low (dark grey) energies. An energy shift can be observed at the position of the groove between both stamped bars (double arrow).

the FBR incubation, the sample was rinsed in Milli-Q water 5–10 times. The optimum drop amount was found to be 10 which translates into a volume of $\approx 2\,\mathrm{nl}$. Below this volume, the drops evaporate too fast for efficient incubation, and above, drops show reduced homogeneity in the observed pattern. In a next step, these procedures will be transfered to our InGaN sensor structures.

5. Conclusion and Outlook

In this work, different approaches for InGaN functionalization have been investigated. The stamping technique was optimized for low unspecific binding and thus high contrast in fluorescent micrographs. One drawback of the stamping procedure is the degradation of the stamp itself and the not well-defined amount of silane molecules on the stamp and thus on the sensor. In the micro-PL setup, no explicit response could be found. This might be attributed to the incomplete coverage of the monolayer and thus very low molecule concentration, or to the sensitivity of the sensor being too low. As reported in previous work from this group, simulations have been performed to improve the sensitivity of the sensor structure. With new structures being grown and functionalized an effective response might be received in the future.

In the second part, a new functionalization technique is introduced: microdrop casting. This technique enables better control of the actual amount of molecules being deposited on the sensor surface and was proven to work effectively on glass substrate. Referring to our experience with stamping, it can be followed that the parameters for ideal functionaliza-

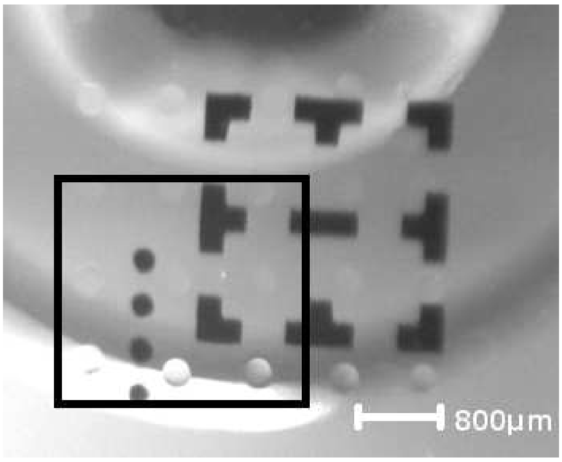

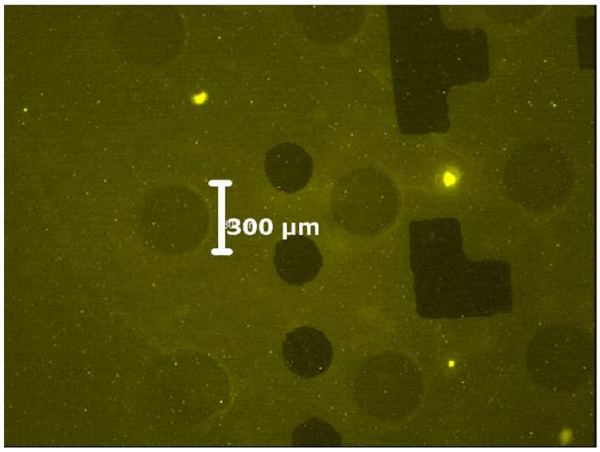

Fig. 5: The dropcasting process can be monitored within the automated micro-PL setup and then related to FL- and PL-measurements (left). The drops can be seen best in the bottom left corner of the black square. The same area as seen in the FL-microscope (right): Drops can be clearly seen alongside the gold marks. They show an inverse behaviour, such that they seem darker than the surounding surface. This was due to non optimized incubation steps and was resolved in later experiments.

tion should not differ strongly for GaN and thus can be adapted. Subsequently, sensing experiments will be performed on these new structures. For live sensing, microfluidic channels can be introduced, which enable measurement of the various functionalization steps. This way a clearer understanding can be drawn of how the various binding steps affect the sensor response.

Acknowledgment

The work presented in this article is a close collaboration of our IOB project group constisting of my fellow PhD colleagues F. Huber and N. Naskar, and the project leaders Prof. K. Thonke, Prof. T. Weil, and my supervisor Prof. F. Scholz. Most results have been obtained from experiments performed by a group of two or more of the PhD students. Financial support by the Baden-Württemberg Stiftung gGmbH within the project "Intelligente optoelektronische Biosensoren" is gratefully acknowledged.

References

[1] F. Yamaki, K. Inoue, N. Ui, A. Kawano, and S. Sano, "A 65 % drain efficiency GaN HEMT with 200 W peak power for 20 V to 65 V envelope tracking base station amplifier", in Proc. *2011 IEEE MTT-S International Microwave Symposium*, 4 pages. Baltimore, MD, USA, June 2011.

[2] K.A. Son, A. Liao, G. Lung, M. Gallegos, T. Hatake, R.D. Harris, L.Z. Scheick, and W.D. Smythe, "GaN-based high-temperature and radiation-hard electronics for

harsh environments", in *Micro- and Nano-Harsh Environment Sensors*, T. George, M.S. Islam, and A.K. Dutta (Eds.), Proc. SPIE 7679, pp. 76790U-1–8, 2010.

[3] I. Yonenaga, "Thermo-mechanical stability of wide-bandgap semiconductors: high temperature hardness of SiC, AlN, GaN, ZnO and ZnSe", *Physica B: Condensed Matter*, vol. 308–310, pp. 1150–1152, 2001.

[4] I. Cimalla, F. Will, K. Tonisch, M. Niebelschütz, V. Cimalla, V. Lebedev, G. Kittler, M. Himmerlich, S. Krischok, J. Schaefer, M. Gebinoga, A. Schober, T. Friedrich, and O. Ambacher, "AlGaN/GaN biosensor—effect of device processing steps on the surface properties and biocompatibility", *Sens. Actuators B*, vol. 123, pp. 740–748, 2007.

[5] D. Heinz, F. Huber, M. Spiess, M. Asad, L. Wu, O. Rettig, D. Wu, B. Neuschl, S. Bauer, Y. Wu, S. Chakrabortty, N. Hibst, S. Strehle, T. Weil, K. Thonke, and F. Scholz, "GaInN quantum wells as optochemical transducers for chemical sensors and biosensors", *IEEE J. Select. Topics Quantum Electron.*, vol. 23, pp. 1–9, 2017.

[6] B. Baur, G. Steinhoff, J. Hernando, O. Purrucker, M. Tanaka, B. Nickel, M. Stutzmann, and M. Eickhoff, "Chemical functionalization of GaN and AlN surfaces", *Appl. Phys. Lett.*, vol. 87, pp. 263901-1–3, 2005.

[7] S. Jung, K.H. Baik, F. Ren, S.J. Pearton, and S. Jang, "Detection of ammonia at low concentrations (0.1–2 ppm) with ZnO nanorod-functionalized AlGaN/GaN high electron mobility transistors", *J. Vac. Sci. Technol. B*, vol. 35, pp. 042201-1–5, 2017.

[8] A. Holmberg, A. Blomstergren, O. Nord, M. Lukacs, J. Lundeberg, and M. Uhlén, "The biotin-streptavidin interaction can be reversibly broken using water at elevated temperatures", *Electrophoresis*, vol. 26, pp. 501–510, 2005.

[9] D. Heinz and M.F. Schneidereit, "Selective functionalization of GaInN quantum well surfaces for applications in biosensing", *Annual Report 2016*, pp. 29–36, Ulm University, Institute of Optoelectronics.

[10] J. DeChancie and K. Houk, "The origins of femtomolar protein ligand binding: hydrogen bond cooperativity and desolvation energetics in the biotin–(strept)avidin binding site", *J. Am. Chem. Soc.*, vol. 129, pp. 5419–5429, 2007.

Investigations of GaN-Based Vertical Field Effect Transistors for Applications in High-Power Electronics

Jan-Patrick Scholz

In this report, some pre-studies for our research project "Investigations of GaN-based vertical field effect transistors (FETs) for applications in high-power electronics" will be shown. In particular, we have re-established decent hydride vapor phase epitaxy sample quality as confirmed by Hall, high-resolution X-ray diffraction and as well by mercury probe measurements. In addition we started with the growth of classical two-dimensional FET test structures by metal organic vapor phase epitaxy.

1. Introduction

For large power density while simultaneously enabling high power conversion efficiency and reduced form factor in semiconductor devices, GaN is a very promising material [1]. However, with ever increasing power density in two-dimensional devices, one reaches a critical source-drain voltage before avalanche-like breakthrough occurs [2] due to free charge carriers accumulating near the gate on the drain side [3]. Current devices work around this issue by increasing the distance between gate and drain contacts [3]. However, these devices need ever increasing space in the horizontal plane. By using the third dimension, it is possible to hold the blocking voltage for still small lateral dimensions. One possible approach is the so-called current aperture vertical electron transistor (CAVET) as shown in Fig. 1. In addition to the decreased lateral size of a three-dimensional-transistor, the problem of surface charges is reduced, as the active region is located within the material [3].

The way these devices work is the following: The field-effect control of the current is very similar as in conventional lateral devices high electron mobility transistors (HEMTs): The gate voltage controls the two-dimensional carrier gas density at the AlGaN-GaN interface. Below this interface, an insulating blocking-layer prevents carriers from escaping to the bulk. The electrons flow from the source contact to the region below the gate where the blocking layer is interrupted thus forming a current aperture. Hence the carriers can drift down to the drain contact positioned below the current aperture. Consequently, fairly large gate-drain distances and thus blocking voltages can be realized by the thickness of this drift region without compromising the lateral size of the device. Therefore, it is possible to control high currents with the gate voltage, while large source-drain voltages can be applied [1, 4].

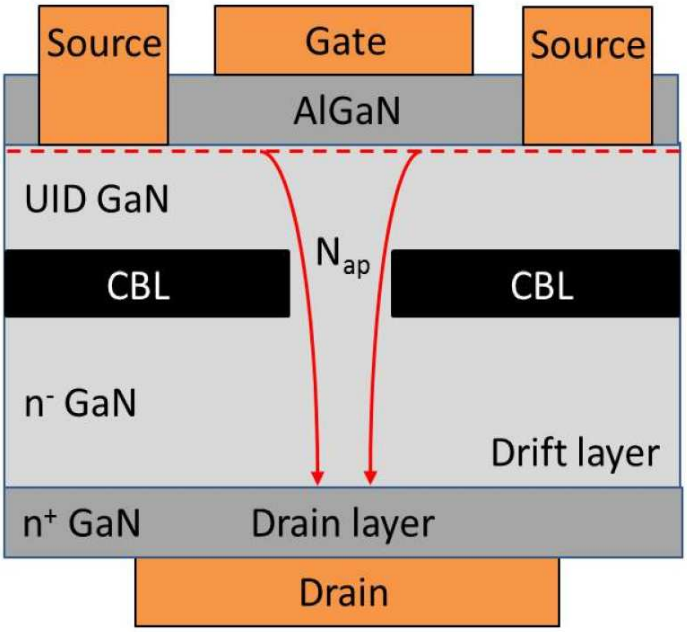

Fig. 1: Schematic view of a CAVET. On top, a classical HEMT structure with an AlGaN layer on unintentionally doped GaN for high electron mobility in the two-dimensional carrier gas at the interface, then the current blocking layer (CBL) forming the current aperture and channelling the current, next a thick drift layer, holding the blocking voltage, and at the bottom a higher n-doped layer for the drain contact (after [1]) .

For such a device to work, it is important to have good crystal quality, otherwise threading dislocations can penetrate the current-blocking layer and create an unwanted current path, the region under the gate being particularly critical. Also for high breakdown voltages, a low free charge carrier concentration is required in the drift region. Therefore, such devices are typically grown on free-standing GaN wafers grown by hydride vapor phase epitaxy (HVPE).

For preparing structures for such CAVETs, we worked on re-establishing good crystal quality in HVPE and metal organic vapor phase epitaxy (MOVPE) grown samples.

2. Experimental Details

The HVPE reactor used to grow thick GaN samples is a horizontal, five-zone hot-wall showerhead reactor (Aixtron Aix LP VPE). A mixture of nitrogen and hydrogen is used as carrier gas, while ammonia is used as the group-V precursor. As Ga precursor, gallium-chloride is formed in-situ by streaming gaseous hydrochloric acid (HCl) over a pure gallium bath at 850 °C. The growth is performed on 2-inch, 2 µm thick MOVPE grown GaN layers on sapphire similar as described by Scholz *et al.* [8].

For the MOVPE growth, a low-pressure horizontal reactor (Aixtron AIX-200/4 RF-S) with the Aixtron standard 2-inch SiC-coated graphite suszceptor is used. All samples are grown on standard (0001) sapphire substrates with an offcut of 0.3° towards the m-plane. Trimethyl-aluminium (TMAl), trimethyl-gallium (TMGa) and ammonia are used as precursors.

For characterisation, a high-resolution X-ray diffractometer (Bruker Discover D8) is used to check the crystal quality of the samples. From the measured rocking curve full-width-half-maximum (FWHM) data, the dislocation density can be deduced [5]. We used a pinhole of 0.3 mm on the emitter side in order to reduce the unwanted effect of peak broadening due to wafer curvature. A Hall setup with a magnetic field of 0.45 T was used to determine carrier concentration and mobility. For our test structures, contacts made of 5 nm titanium, 220 nm aluminium, 40 nm nickel and 50 nm gold have been deposited. The contacts were annealed at 700 °C for three minutes.

Capacitance-voltage (C-V) measurements were performed using a mercury probe at Inatech in Freiburg by M.Sc. Björn Christian.

3. Growth and Evaluation of HVPE and MOVPE Test Samples

Currently, high quality GaN layers with a reasonable thickness of 2 µm grown in our MOVPE reactor have typical X-ray diffraction rocking curve widths of 300 arcsec and 400 arcsec for the symmetric (002) and the asymmetric (102) peak, respectively, as confirmed by high-resolution X-ray diffraction (HRXRD) measurements. It is expected that the defect density and hence the FWHM of the rocking curve peaks is reduced in thicker layers grown on such templates by HVPE. However, in these studies, we concentrated on fairly thin HVPE layers of about 15 µm thickness in order to keep them crack-free. Indeed, most samples show slight improvement in crystal quality for the 102 peak which mainly reflects edge-type dislocations. For the best samples, we found peak widths as low as 200 arcsec. The 002 peak, mainly caused by screw-type dislocations, typically did not change significantly. One possible explanation for this is the fact that because of the different growth speed in the HVPE as compared to the MOVPE we get a more three-dimensional growth an therefore the stacking of the crystal planes is not so good in the c-direction. Another possible explanation for the still high defect density may be due to the not yet perfectly optimized HVPE process. On some samples, we found particles from the shower head which might disturb the further growth. A better cleaning procedure with HCl may help to overcome such problems.

It is important to note here that, even though we did not see a clear reduction in the 002 FWHM, the defect density scales with the square of the respective FWHM for the respective peak. Therefore a factor two in the 102 peak width means a significant reduction in dislocation density of the samples by a factor of four [5].

In order to directly confirm the improved crystal quality and to get quantitative values for the dislocation density, it is planned to measure the etch pit density of the samples and calculate from that the number of threading dislocations reaching the surface.

This can be done by etching the samples in the HVPE reactor at elevated temperatures with HCl [6]. The etch pit density can then be determined either by scanning electron microscopy or by atomic force microscopy.

The electrical characteristics of our MOVPE and HVPE layers were measured via the use of the Hall effect in van-der-Pauw geometry. The carrier concentration of the 2 µm thick MOVPE samples was below the detection limit of our setup. For the 15 µm thick HVPE samples, n-type carrier concentrations in the order of $2 \cdot 10^{16}\,\mathrm{cm}^{-3}$ were measured.

On three MOVPE and two HVPE samples, C-V profiles were measured using a mercury probe at Inatech (University of Freiburg). These experiments confirmed the quite low carrier concentration in these samples: The free-carrier concentration for all except one HVPE sample was not high enough for the measurement, indicating good quality and a useful substrate for further applications in vertical field effect transistors. Only one sample was near the detection limit of the C-V-measurement (Fig. 2).

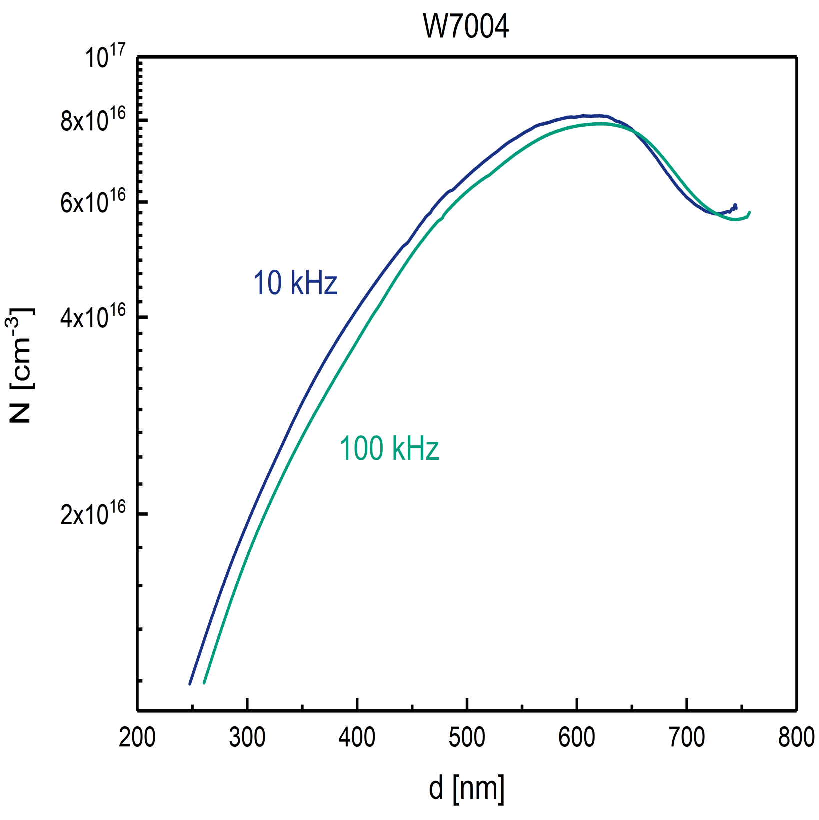

Fig. 2: C-V depth scan near the surface of a 15 µm thick HVPE sample (W7004) for two different measurement frequencies, showing a slight deviation from the carrier concentration of $4.8 \cdot 10^{16}\mathrm{cm}^{-3}$ measured by Hall. This is probably due to the fact that in Hall the bulk data is measured while C-V measurements are surface-sensitive. Even though the sample was near the detection limit, a meaningful depth profile could be obtained, since the courses for the two different measurement frequencies are similar .

4. Growth and Evaluation of 2-D HEMTs Grown in MOVPE

In addition to the HVPE experiments, we started growing classical HEMT test structures by MOVPE being composed of an AlGaN barrier on top of our undoped GaN layers described above, where a 2-dimensional electron gas (2DEG) is formed at the boundary between GaN and AlGaN.

Starting with a sapphire wafer, first 2 µm thick GaN was grown. On top of that a 18 nm thick $Al_{0.34}Ga_{0.66}N$ barrier layer was deposited and finally a 3 nm thick GaN cap layer for better contacts. Between the AlGaN and the GaN layer an about 1 nm thick AlN layer was placed which prevents the electron wave function to penetrate into the ternary barrier and thus leads to a higher mobility of the 2DEG.

These first test structures show promising results with an electron mobility of $1326\,\mathrm{cm^2/(Vs)}$ at room-temperature and $4328\,\mathrm{cm^2/(Vs)}$ at 77 K. The fairly low values at nitrogen temperature indicate that we still have some defects in our layers which requires further optimization. However the measured carrier concentration of $1.9 \cdot 10^{13}\,\mathrm{cm^{-2}}$ is high when compared to expected results for such structures [7].

A possible explanation for this may be unintentional doping [9]. However since our buffer layers have indicated high resistivity, the doping might come from the AlN precursor TMAl.

5. Summary

In order to improve the breakdown voltages of GaN-based field effect transistors, we have started to investigate the concept of vertical transistors. For such devices, high quality GaN is needed. Therefore we have investigated the quality of MOVPE and HVPE grown GaN layers. HRXRD, Hall-effect and C-V measurements confirmed the high quality of such layers which should be sufficient for vertical transistors. In a next step, etch experiments in our HVPE reactor will be done to determine the defect density directly. First two-dimensional HEMT test structures grown by MOVPE also indicated promising quality for the future device, although the measured sheet carrier concentration is a little bit too high for our purposes, which will also be worked on in the future.

6. Acknowledgment

Special thanks go M.Sc. Björn Christian from Inatech in Freiburg for C-V measurements. This work was financially supported by the Deutsche Forschungsgemeinschaft within the framework of the project “Investigations of GaN-Based Vertical Field Effect Transistors for Applications in High-Power Electronics”.

References

[1] S. Chowdhury, B.L. Swenson, M.H. Wong, and U.K. Mishra, "Current status and scope of gallium nitride-based vertical transistors for high-power electronics application", *Semicond. Sci. Technol.*, vol. 28, pp. 074014-1–8, 2013.

[2] I. Ben-Yaacov, Y.-K. Seck, and U.K. Mishra, "AlGaN/GaN current aperture vertical electron transistors with regrown channels", *J. Appl. Phys.*, vol. 95, pp. 2073–2078, 2004.

[3] N.-Q. Zhang, B. Moran, S.P. DenBaars, U.K. Mishra, X.W. Wang, and T.P. Ma, "Kilovolt AlGaN/GaN HEMTs as switching devices", *Phys. Status Solidi A*, vol. 188, pp. 213–217, 2001.

[4] X. Liu, H. Gu, K. Li, L. Guo, D. Zhu, Y. Lu, J. Wang, H.-C. Kuo, W. Liu, L. Chen, J. Fang, K.-W. Ang, K. Xu, and J.-P. Ao, "AlGaN/GaN high electron mobility transistors with a low sub-threshold swing on free-standing GaN wafer", *AIP Advances*, vol. 7, pp. 2158–3226, 2017.

[5] M.A. Moram and M.E. Vickers, "X-ray diffraction of III-nitrides", *Rep. Prog. Phys.*, vol. 72, pp. 036502-1–40, 2009.

[6] F. Habel and M. Seyboth, "Determination of dislocation density in epitaxially grown GaN using an HCl etching process", *Phys. Status Solidi A*, vol. 7, pp. 2448–2451, 2003.

[7] O. Ambacher, J. Smart, J. Shealy, N. Weimann, K. Chu, M. Stutzmann, W. Rieger, and J. Hilsenbeck, "Two-dimensional electron gases induced by spontaneous and piezoelectric polarization charges in N- and Ga-face AlGaN/GaN heterostructures", *J. Appl. Phys.*, vol. 85, pp. 3222–3233, 1999.

[8] F. Scholz, P. Brückner, M. Peter, K. Köhler, and F. Habel, "Improved GaN layer morphology by hydride vapor phase epitaxy on misoriented Al_2O_3 wafers", *Appl. Phys. Lett.*, vol. 87, pp. 181902-1–3, 2005.

[9] O. Ambacher, B. Foutz, J. Smart, J.R. Shealy, N.G. Weimann, K. Chu, M. Murphy, A.J. Sierakowski, W.J. Schaff, L.F. Eastman, R. Dimitrov, A. Mitchell, and M. Stutzmann, "Two-dimensional electron gases induced by spontaneous and piezoelectric polarization in undoped and doped AlGaN/GaN heterostructures", *J. Appl. Phys.*, vol. 87, pp. 334–344, 2000.

A Multipass Optics for Quantum-Well-Pumped Semiconductor Disk Lasers

Markus Polanik

The pump absorption of quantum-well-pumped semiconductor disk lasers can significantly be improved with a resonant design for the pump wavelength inside the semiconductor disk and an external optics that redirects the reflected pump power several times back onto the disk. Our double-resonant laser, which is designed for an emission wavelength of 985 nm and a pump wavelength of 940 nm, allows a pump absorption of about 35 % in a double pass of the pump radiation through the disk. Here, we demonstrate how the absorption of the pump power can be further improved using a multipass pump optics. This pump optics consists of a parabolic mirror and two retro-reflecting prisms allowing up to three double passes of the pump radiation through the semiconductor disk. This is sufficient for absorption rates above 75 %. The laser disks mounted on copper heat sinks are capable of output powers beyond 16 W and of slope efficiencies above 50 %.

1. Introduction

Using optical pumping of the quantum wells of a semiconductor disk laser directly instead of pumping the surrounding barriers, it is possible to drastically reduce the quantum energy difference between the pump and the laser photon which is called the quantum defect. This wavelength difference can be less than 2.1 nm, which corresponds to a quantum defect below 0.22 % [1]. Consequently, the produced amount of waste heat inside the active region originating from the quantum defect becomes negligible. The elimination of the largest loss mechanism allows to realize high-power lasers that do not depend on strong cooling. The major drawback of such a laser is the low absorption of the pump power. Therefore, investigations are necessary on how the pump absorption can be improved by redirecting the unabsorbed light multiple times back onto the chip. A conventional multipass optics consists of a parabolic mirror and at least two retro-reflecting prisms and provides up to eight double passes of the pump radiation through the disk [2]. More complex pump designs allow 32 double passes [3]. An absorption rate above 70 % was already reported for quantum-well-pumped semiconductor disk lasers using twelve double passes [4]. This result, however, is not necessarily comparable with other quantum-well-pumped disk lasers, since the absorption strongly depends on the layer structure and the difference between the pump and laser wavelength. Our multipass optics allows to experiment with one, two, or three double passes of the pump radiation through the disk, which gives us the ability to predict how the pump absorption behaves in dependence of the number of double passes.

2. Layer Design and Characterization of the Disk Laser

The quantum-well-pumped semiconductor disk laser has a resonant structure for the emission wavelength of 985 nm and for the pump wavelength of 940 nm. The realization of such a double-resonant structure requires to grow an over 1 µm-thick GaAs spacer between two sets of four double quantum wells, as depicted in Fig. 1. The separation of the quantum wells is necessary because of the phase shift between laser and pump field [5, 6]. Another specialty of the design is the top Bragg reflector which increases the finesse of the microcavity and therefore enhances the resonant absorption. Both sides of the semiconductor laser are coated with an ion-beam sputter-deposited dielectric coating. The dielectric layer on top serves as an anti-reflection (AR) coating for the pump radiation, while the bottom coating allows to reduce the mirror pairs of the bottom Bragg reflector from 24.5 to 18.5 without sacrificing a reflection loss. This is possible due to the large refractive index difference between Al_2O_3 and GaAs. The epitaxial growth is performed in reverse order. This allows us to apply the bottom dielectric coating on the whole waver before a Ti/Au metalization is applied. Afterwards, the wafer is cleaved into $2 \times 2\,\mathrm{mm}^2$ large pieces and soldered with indium on copper heat sinks. Then the GaAs substrate is completely removed by wet-chemical etching and the AR coating is applied.

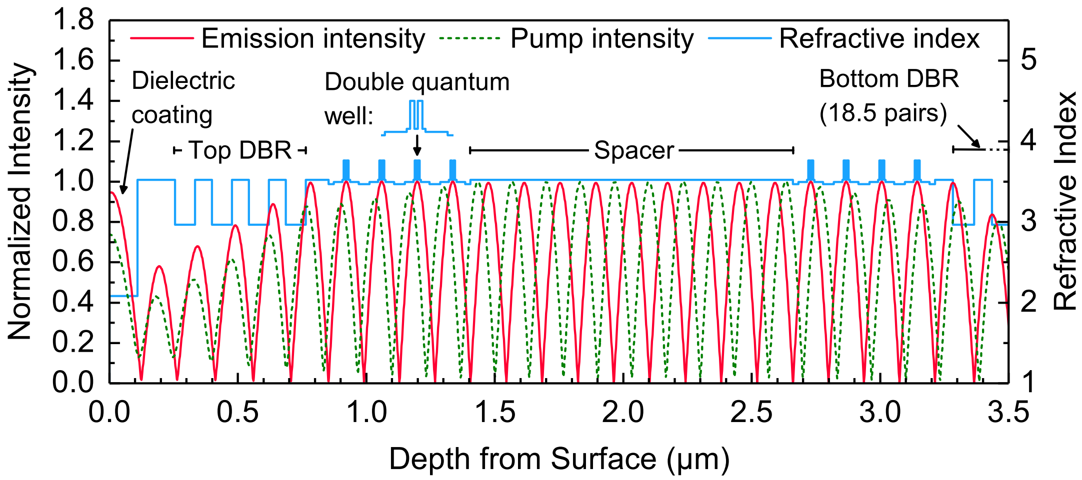

Fig. 1: Layer structure of the disk laser visualized by the refractive index profile as well as calculated TE standing-wave intensities of the laser and pump fields.

The reflectivity spectrum of a fully processed disk laser is shown in Fig. 2. The spectrum was recorded under an angle of 10° at a temperature of 80°C. Inside the stop band extending between 905 and 1015 nm, three resonance wavelengths are visible. The 953 nm long resonance wavelength is important for pumping the device because under a certain angle of incidence the 940 nm pump light is in resonance with cavity. A pump angle of 35° is therefore required in order to achieve a good absorption of the pump power. The laser emission takes place at the 988 nm long resonance wavelength. Even at output powers beyond 15 W the spectral width of the laser is below 1.1 nm (full width at half maximum). This makes the laser especially suitable for frequency doubling applications, since no birefringent filter is necessary to narrow the spectral width. The recorded photoluminescence spectrum shows a good overlap with the measured reflectivity spectrum. The photoluminescence spectrum was measured under an angle of 0° and at a heat-sink temperature of 50°C.

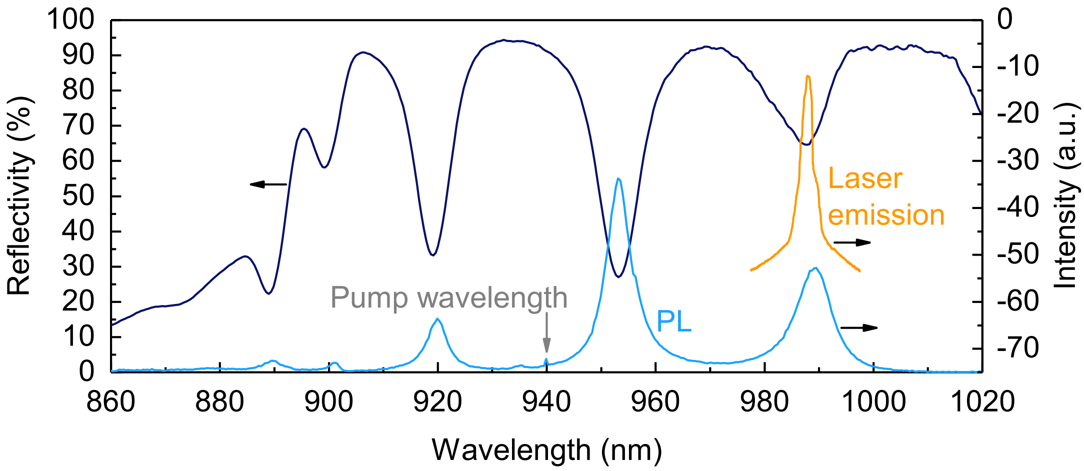

Fig. 2: Measured reflectivity, photoluminescence (PL) and emission spectrum of a quantum-well-pumped semiconductor disk laser.

3. Multipass-Pumped Semiconductor Disk Laser

One double pass of the pump radiation through the disk allows a pump power absorption of approximately 35 %. A significant improvement of the laser's efficiency is therefore possible by recycling the unused power. In order to achieve two double passes of the pump radiation through the disk and be able to measure the reflected pump power, an experimental setup as illustrated in Fig. 3 is used. The disk laser is operated in a linear resonator with an external mirror that has a reflectivity of 96 %. The pump optics consists of a parabolic mirror and a prism acting as a retro reflector. The collimated pump beam is propagating parallel to the linear resonator until it hits the parabolic mirror. The parabolic mirror focuses the pump light onto the semiconductor disk which is placed in the focal point of the parabolic mirror. The pump spot size of the multipass optics is determined by the diameter of the pump source, the focal length of the collimator lens, and by the focal length of the parabolic mirror [2]. A change of the spot size is therefore not possible without changing the used optics. The purpose of the prism is to perform a retro-reflection of the pump beam and to displace the beam by a few millimeters, so that the 180° turned beam hits the parabolic mirror on another position. From there the beam is focused again onto the chip. The experimentally determined loss factor of the pump optics is 14.7 %. By adding another prism to the pump optics, a third double pass of the pump radiation through the disk can be achieved. Due to space restrictions it not possible to measure the absorbed power in this configuration. The absorbed power shown in Fig. 4 for three double passes was therefore calculated from a reference measurement with two double passes.

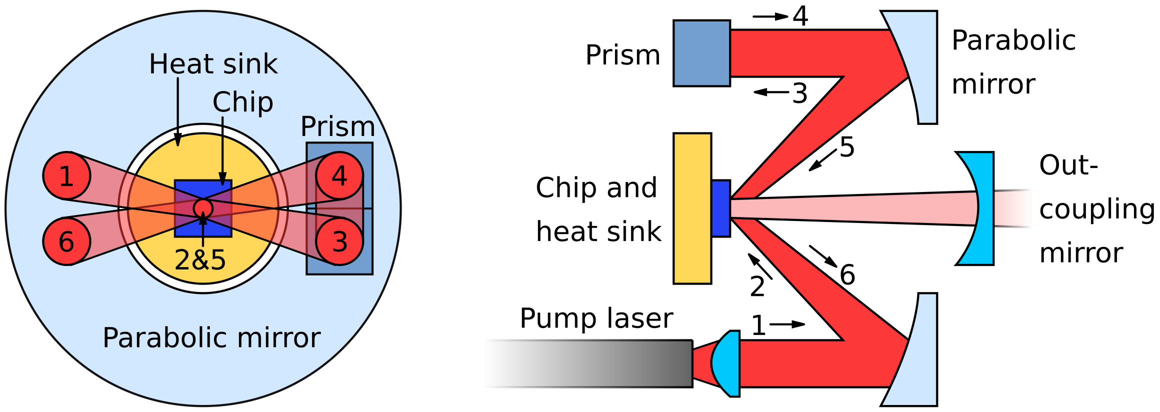

Fig. 3: Front view (left) and top view (right) of a pump optics for two double passes of the pump radiation through the semiconductor disk. The numbers 1 to 6 indicate the path of the pump beam.

Without using the multipass pump optics, the disk laser is capable of a slope efficiency of 56.7 % and an output power of 13.37 W. The maximum output power was limited by the available pump power. The threshold of the laser is 2.03 W. A threshold power density of 1.8 kW/cm^2 can be calculated considering the $400 \times 350\,\mu m^2$ large elliptical pump spot. The measured spot size of the multipass optics of $750 \times 650\,\mu m^2$ is almost 250 % larger than without the pump optics. Consequently, the threshold power increases. A large pump spot can cause additional heating problems, hence a larger spot size also increases the probability of semiconductor defects inside the pumped area. In addition, further heating problems may be expected, due to the compromised heat spreading. Nevertheless, only a minor decrease of the slope efficiency by 7.3 % is noticeable. A threshold pump power of 12.24 W and a threshold power density of 3.2 kW/cm^2 are measured with the multipass optics. The maximum achievable output power is 16.23 W for two double passes through the disk. The absorption of the pump power is between 50.7 and 61.9 %. The conversion of the pump optics into an optics which allows three double passes, without changing any other laser conditions, results in absorption rate in between 65.4 and 76.1 %. The other output characteristics of the laser are almost identical, except of a minor decrease of the achievable output power by 0.5 W. The power loss can be attributed to the elliptical shape of the pump spot, which does not allow a perfect overlap of all three pump spots on the disk, since the elliptical spots are tilted by the prisms. A pump optics for three double passes requires, as illustrated in Fig. 5, to overlap six spots on the chip by proper alignment of the pump optics and the external outcoupling mirror.

A clear disadvantage of the pump optics is its restriction to a few degrees around 19° for the pump angle. It is therefore required, that the microcavity of the disk laser has a suitable resonance wavelength for the pump wavelength of 940 nm. Otherwise, a weak absorption rate is unavoidable. A shift of 5 nm in the resonance wavelength, for instance, will result in an absorption of only 35.7 % instead of 61.9 % for two double passes of the pump radiation through the disk [7]. The thermal roll-over of the laser device when exceeding 45 W of absorbed pump power exceeds may be avoided by improvements of the cooling setup, which in our experiments does not allow heat-sink temperatures below 4°C and lacks in temperature stabilization.

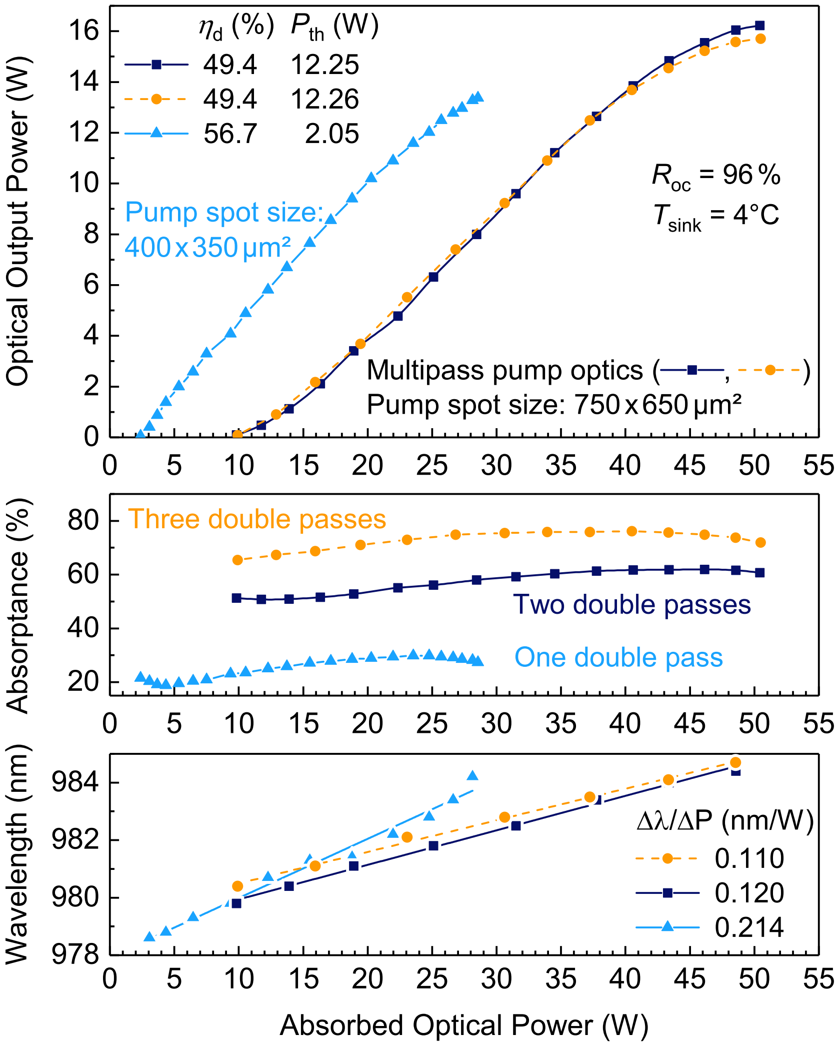

Fig. 4: Output characteristics of a quantum-well-pumped disk laser without a multipass pump optics and with a pump optics that allows two or three double passes of the pump radiation through the disk.

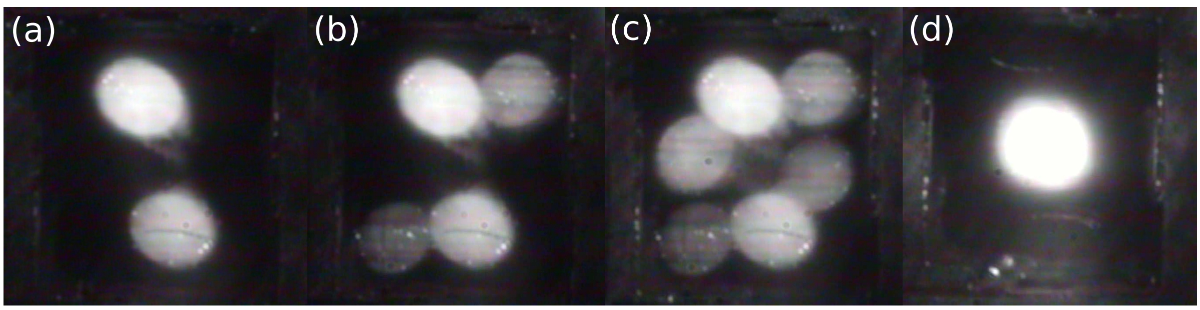

Fig. 5: Pictures of the disk laser's surface for one (a), two (b), or three (c) double passes of the pump radiation through the disk. The case of an aligned resonator and pump optics is shown in (d).

4. Conclusion and Outlook

By recycling the otherwise unused pump power with a multipass pump optics it was possible to significantly improve the pump power absorption of the investigated quantum-well-pumped semiconductor disk laser. The maximum achievable absorption of the disk laser is about 35 % during a single double pass of the pump radiation through the disk. With the used multipass pump optics, a second and third double pass was realized. This leads to a maximum absorption of 61.9 % and 76.1 %, respectively. By adding a third retro-reflecting prism and a flat end mirror which reverses the beam path, it will be possible to achieve eight double passes of the pump radiation through the disk. This may be sufficient for pump power absorptions above 95 % [7]. A temperature-stabilized cooling setup and the use of diamond heat spreaders may improve the output power beyond the value of 16.23 W, which has been achieved in this presentation.

Acknowledgment

My gratitude goes to Alexander Hein for his preliminary studies, to Susanne Menzel for the epitaxial growth and to Uwe Brauch for his technical support with the multipass pump optics.

References

[1] M. Polanik, “Optically pumped semiconductor disk lasers with ultra-low quantum defect”, seminar talk, *Seminar “Functional Nanosystems”, Ulm University*, Ulm, Germany, Jan. 2018.

[2] S. Erhard, *Pumpoptiken und Resonatoren für den Scheibenlaser*, Ph.D. Thesis, University of Stuttgart, Stuttgart, Germany, 2002.

[3] K. Albers and U. Wittrock, “Optical pump concepts for highly efficient quasi-three-level lasers”, *Appl. Phys. B*, vol. 105, pp. 245–254, 2011.

[4] S.-S. Beyertt, M. Zorn, T. Kübler, H. Wenzel, M. Weyers, A. Giesen, G. Tränkle, and U. Brauch, “Optical in-well pumping of a semiconductor disk laser with high optical efficiency”, *IEEE J. Quantum Electron.*, vol. 41, pp. 1439–1449, 2005.

[5] A. Hein and U. Brauch, “Optically in-well-pumped semiconductor disk laser with low quantum defect”, *Annual Report 2014*, pp. 69–76, Ulm University, Institute of Optoelectronics.

[6] M. Polanik, “Quantum-well-pumped semiconductor disk lasers for single- and dual-wavelength emission”, *Annual Report 2015*, pp. 3–12, Ulm University, Institute of Optoelectronics.

[7] M. Polanik, *Charakterisierung von optisch quantenfilmgepumpten Halbleiterscheibenlasern mit kleinem Quantendefekt*, Master Thesis, Ulm University, Ulm, Germany, 2015.

Piezoelectric Birefringence Tuning of Vertical-Cavity Surface-Emitting Lasers

Tobias Pusch

Exploiting the polarization dynamics of spintronic vertical-cavity surface-emitting lasers (VCSELs) can be a potential alternative to direct intensity modulation for high-speed data transmission. The frequency difference between the two fundamental linear polarization modes in VCSELs, the so-called birefringence splitting B, is the key parameter. For later applications, easy handling and control of B is favored, which can be realized by electrical birefringence tuning. In an integrated chip, thermally induced strain via asymmetric heating with a birefringence tuning range of 45 GHz was shown. In this article we present our work on VCSEL structures mounted on piezoelectric transducers for strain generation. Furthermore we investigate a combination of both techniques, namely VCSELs with piezo-thermal birefringence tunability.

1. Introduction

VCSELs are the emitters of choice for short-distance data transmission owing to their beneficial properties like low energy consumption, high fiber coupling efficiency, and low production cost [1]. Commercial devices with data rates of 25 . . . 28 Gb/s are currently being deployed. Data rates of 71 Gb/s (using transmitter equalization [2]) and 150 Gb/s (with higher-order modulation [3]) have already been shown. To reduce system complexity and increase the efficiency, a higher modulation bandwidth of the emitter is needed. An increase of the intensity modulation bandwidth is physically limited. Polarization dynamics in VCSELs are much faster and can be a promising alternative [4]. The frequency difference between the two fundamental linear polarization modes, the so-called birefringence splitting, is the determining factor for the polarization dynamics in a spin-VCSEL [4]. By inducing carrier spin in a birefringent VCSEL, an oscillation in the degree of circular polarization with an oscillation frequency close to birefringence splitting can be generated [5]. In combination with the capability to stop the oscillation after a very short time interval, this could be the basis for ultrafast dynamics in future devices [6]. Using the elasto-optic effect, the birefringence splitting in VCSELs can be manipulated. To do so, asymmetric strain has to be induced along a crystal axis parallel to one of the two preferred linear polarization directions. In 2015 we showed a record-high birefringence splitting of $B = 259$ GHz by direct bending of a VCSEL array [7]. For convenient operation and miniaturization, thermally induced splitting can be used. A first attempt to alter the strain thermally was reported by Jansen van Doorn et al. [8] using an external laser spot focused close to a VCSEL mesa. The birefringence splitting was increased irreversibly up to $B = 23$ GHz. With a keyhole-shaped VCSEL design we realized asymmetric heating close to the active area with a birefringence tuning range of $\Delta B = 45\,\text{GHz}$ [9]. In this paper we focus on strain inducing in VCSELs via a piezoelectric substrate, which combines electrical control and easy handling on a small scale.

In Sect. 2 we show the preparation steps to fabricate VCSEL arrays with extremely small sample thickness as needed to induce strain piezoelectrically. In Sect. 3 optical spectra and light–current–voltage curves for different piezoelectric voltages and sample thicknesses are presented. Furthermore we discuss the influence of the glue necessary to attach the VCSEL array to the piezoelectric substrate. Finally, for a first sample, the combination of (piezo-)mechanical stretching and on-chip asymmetric heating is investigated.

2. Simulations and Sample Preparation

Mechanical bending of a VCSEL sample is an efficient technique to obtain large birefringence splitting [7]. However, electrically driven birefringence tuning is favorable in terms of module size and fine-tuning capability. Piezoelectric transducers are a well-known manipulation tool used to induce strain in semiconductors [10, 11]. In this paper, for the first time we employ such actuators for birefringence tuning in VCSELs. To estimate the potential for strain transfer, finite-element simulations are performed with the Comsol Multiphysics software. Experimentally a VCSEL array of $1 \times 1\,\text{mm}^2$ size is attached to a piezoelectric substrate with a length of 9 mm. The relative stretching is limited to about 0.1 % (Piezo-stack PSt 150/2×3/7, Piezomechanik). In the ideal case, the strain is transferred to the VCSEL array without losses. In [7] we have reported an approximately linear increase of the birefringence splitting with increased bending. The maximum lattice expansion of about 0.4 % resulted in a birefringence splitting $B \approx 260\,\text{GHz}$. This leads to a potential birefringence splitting of about 65 GHz for strain inducing by the above piezoelectric transducers. For top-emitting VCSELs, strain relaxation takes place in the GaAs substrate below the epitaxial layers. From simulations, compared to a substrate-removed device, the strain is reduced by 19 % and 5 % for substrate thicknesses of 100 µm and 50 µm, respectively. The glue at the interface between VCSEL array and piezoelectric substrate has a thickness of about 15 µm and should theoretically have almost no influence on the transferred strain. However, quite some uncertainty exists in the actual elastic and surface properties of the glue material.

In 2016 we reported a first attempt of strain inducing in VCSELs via mechanical stretching of a piezoelectric transducer [12]. We used a $1 \times 1\,\text{mm}^2$ array of AlGaAs-based 850 nm single-mode oxide-confined VCSELs from Philips Photonics GmbH with p- and n-contacts on the top side which was glued on a piezoelectric substrate with a length of 9 mm. This is depicted in the photograph in Fig. 1 together with an image of the VCSEL unit cell as an inset.

With a sample thickness of 120 µm, including a total epitaxial layer thickness of about 8 µm on a GaAs substrate, and a stretching ratio of around 0.1 % there was no measurable change of the birefringence splitting. In this work we maximize the indirectly applied strain in the VCSEL array by reducing the thickness of the laser sample. Different VCSEL arrays with a size of $5 \times 5\,\text{mm}^2$ are cleaved from a larger sample as in [12]. We target

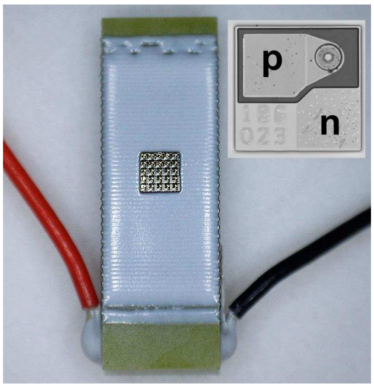

Fig. 1: VCSEL array of $1 \times 1\,\mathrm{mm}^2$ size glued on a piezoelectric substrate. Top view of the $165 \times 165\,\mu\mathrm{m}^2$ large VCSEL unit cell with p- and n-type top side contacts in the inset [12].

a series of measurements with sample thicknesses from 120 µm to about 20 µm in 10 µm steps. The arrays are glued upside down on a glass substrate with thermoplastic glue. To etch the GaAs substrate we use a mixture of hydrogen peroxide (H_2O_2) and aqueous ammonia solution (NH_4OH) with a pH value of 8.3. The chemical solution is sprayed at high pressure on the back side of the VCSEL array. A pre-determined etch rate serves to estimate the etch time. After etching the thinned VCSEL array is removed from the glass substrate and the final thickness is measured. We obtain samples with a minimum thickness of 28 µm. Thinner samples were too fragile and could not be handled anymore. The thinned arrays are cleaved to sample sizes of around $1 \times 1\,\mathrm{mm}^2$ to get rid of damaged material at the edges. Glueing is done with several drops of a two-component glue (EPO-TEK 353ND) that are put manually on the piezoelectric transducer with a syringe. To maximize the strain transfer, a positioning of the VCSEL array parallel to the stretching direction is necessary, which is realized by a pick-and-place machine.

3. Birefringence Tuning via Piezoelectric Effect

The piezoelectric substrate can be stretched by an applied voltage of up to 150 V, which could result in 0.1 % maximum expansion of the VCSEL array, disregarding the influence of the glue. The VCSEL array with minimum sample thickness of 28 µm according to Sect. 2 is investigated first. The light–current–voltage (LIV) curves and optical spectra are measured for piezo voltages V_{piezo} from 0 to 150 V in steps of 10 V. In addition, a measurement for a negative piezo voltage $V_{\mathrm{piezo}} = -30\,\mathrm{V}$ is done to see the effect of compression. Figure 2 shows the results for $V_{\mathrm{piezo}} = 0\,\mathrm{V}$. The threshold current is $I_{\mathrm{th}} = 0.5\,\mathrm{mA}$ at a voltage of $V_{\mathrm{th}} = 1.72\,\mathrm{V}$. At a bias current of $I = 3.5\,\mathrm{mA}$ an optical output of $P = 0.95\,\mathrm{mW}$ is reached. No change in P is noticed for a stretched sample at $\hat{V}_{\mathrm{piezo}} = 150\,\mathrm{V}$. Figure 2 also includes the optical spectrum of the fundamental mode at $\hat{V}_{\mathrm{piezo}}$ as a dash-dotted line. The two peaks which can be seen in both spectra are the two orthogonal polarization states of the fundamental mode. The spectral shifts of the polarization modes under stretching are approximately symmetric. The spectra were measured with a linear polarizer suppressing the dominant polarization mode at shorter wavelength. Without

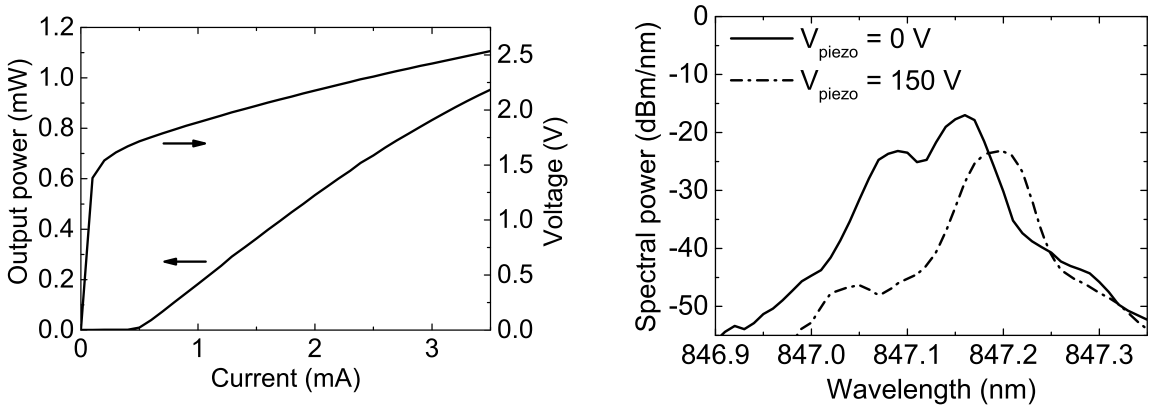

Fig. 2: Light–current–voltage curves of the VCSEL without applied piezo voltage (left). Optical spectra for $V_{\text{piezo}} = 0\,\text{V}$ (solid line) and $150\,\text{V}$ (dash-dotted line) at $I = 3.5\,\text{mA}$ (right). Both measurements were done with a linear polarizer suppressing the dominant polarization mode.

polarizer, even at the maximum resolution of the optical spectrum analyzer of 0.015 nm, the weak mode would be hidden in the shoulder of the main polarization mode. Without stretching a wavelength difference of $\Delta\lambda_{0\,\text{V}} = 0.07\,\text{nm}$ is measured. This splitting indicates a built-in strain in the sample originating from the electro-optic effect [13], the fabrication process, and possible contributions from mounting and contacting. For maximum piezo voltage, $\Delta\lambda_{150\,\text{V}} = 0.16\,\text{nm}$ is obtained. The wavelength splitting corresponds to the birefringence splitting $B = \Delta\nu = c\Delta\lambda/\lambda^2$ with c as the vacuum velocity of light, thus $B_{0\,\text{V}} = 29\,\text{GHz}$ and $B_{150\,\text{V}} = 67\,\text{GHz}$. The relation between birefringence splitting B and voltage applied to the piezoelectric transducer V_{piezo} is plotted in Fig. 3. A decrease of B from $-30\,\text{V}$ to $10\,\text{V}$ and an increase from $40\,\text{V}$ up to $150\,\text{V}$ are found. The maximum tuning range is $\Delta\hat{B} \approx B_{150\,\text{V}} - B_{50\,\text{V}} = (67-21)\,\text{GHz} = 46\,\text{GHz}$. The grey and black data points correspond to a dominant polarization mode at shorter and longer wavelength, respectively. Two polarization flips are observed, namely between 10 V and 40 V and at 110 V. The first flip occurs after the crossing of the modes when the long-wavelength mode is favored by the gain spectrum $g(\lambda)$. The second flip is in accordance with the shift of $g(\lambda)$ to shorter wavelengths under tensile strain [14]. The laser current and the sample temperature were kept constant, thus excluding effects of heating and associated red-shifts of the modes or the gain curve. Between about 10 V and 40 V the birefringence is below the resolution limit of the optical spectrum analyzer. As mentioned in Sect. 2, we are interested in the relation between sample thickness and birefringence splitting. Within the batch of produced samples only for four different sample thicknesses d a change of B was found. As can be seen in Table 1, the birefringence splitting increases from $B = 37\,\text{GHz}$ for $d = 58\,\mu\text{m}$ up to $B = 67\,\text{GHz}$ for $d = 28\,\mu\text{m}$, always at $V_{\text{piezo}} = 150\,\text{V}$. For the samples with $d = 50\,\mu\text{m}$ and $40\,\mu\text{m}$ the same birefringence splitting was measured. In our experiments we figured out that the glue plays an important role for the stress transfer from the piezoelectric substrate to the VCSEL array. As described, the glue deposition so far is a manual process and the amount of glue, which is directly related to the glue thickness, slightly differs from sample to sample.

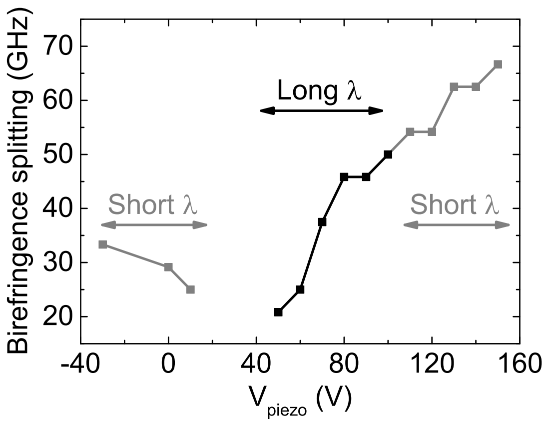

Fig. 3: Change of the birefringence splitting with applied piezo voltage V_{piezo}. Grey squares: dominance of the short-wavelength polarization mode; black squares: long-wavelength mode dominates.

Table 1: Birefringence splitting measured at maximum stretching of the piezoelectric transducer ($V_{\mathrm{piezo}} = 150\,\mathrm{V}$) for different sample thicknesses of the VCSEL array.

Sample thickness (µm)	Birefringence splitting (GHz)
58	37
50	54
40	54
28	67

4. Piezo-Thermal Birefringence Tuning

A VCSEL array equipped for asymmetric current-induced heating is combined with mechanical stretching using the piezoelectric effect for purely electrical piezo-thermal birefringence tuning. To incorporate strain by heating, the mesa has a keyhole-like shape with a ridge oriented parallel to one of the two preferred polarization directions. There are two bondpads on the top side connected with the ridge and the p-ring contact, respectively and a full-area back side contact. The oxide aperture diameter is around 5 µm and the ridge is fully oxidized to prevent current flow to the substrate side contact. Two electrical circuits provide a high heating current I_{H} and a low laser operation current I_{L} simultaneously. As shown in Fig. 4 (left), the heating current flows from the lower bondpad into the ridge to the p-ring contact and the upper bondpad. The main heating occurs in the ridge and creates an asymmetric heat gradient in the resonator. For laser operation, the current is injected in the upper bondpad and flows over the p-ring contact through the VCSEL to the back side contact. Combining this kind of VCSEL with the piezoelectric substrate, four contact needles are necessary for testing. First a VCSEL array is thinned as in Sect. 2 using wet-chemical etching until a sample thickness of 30 µm is reached. To establish a current flow for laser operation, a conductive glue (Polytec EC 101) is deposited on the piezoelectric transducer over an area slightly exceeding that of the VCSEL array. The

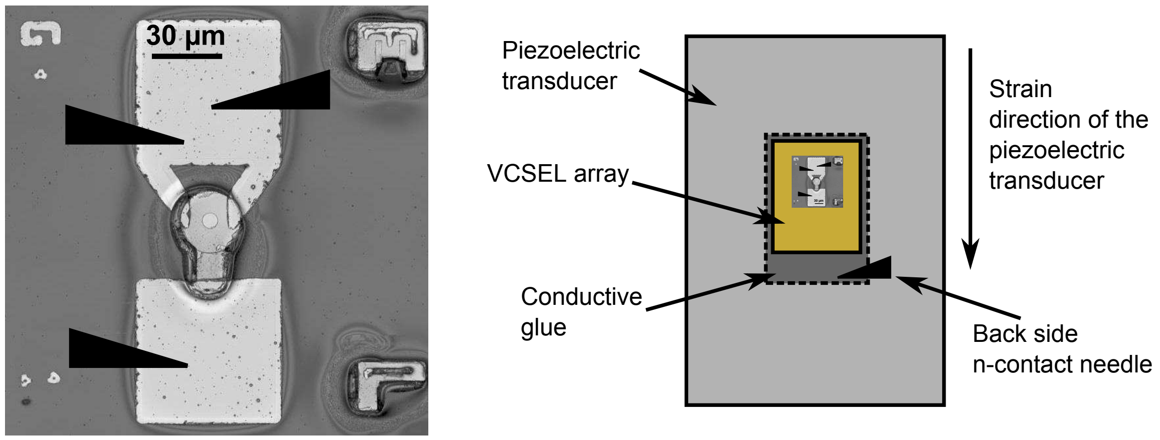

Fig. 4: Photograph of a VCSEL chip allowing for asymmetric thermally induced strain. Three contact needles are added for illustration (left). Schematic drawing of a VCSEL array glued on a piezoelectric transducer for piezo-thermal birefringence tuning. The image of the VCSEL unit cell shows the orientation relative to the strain direction (right).

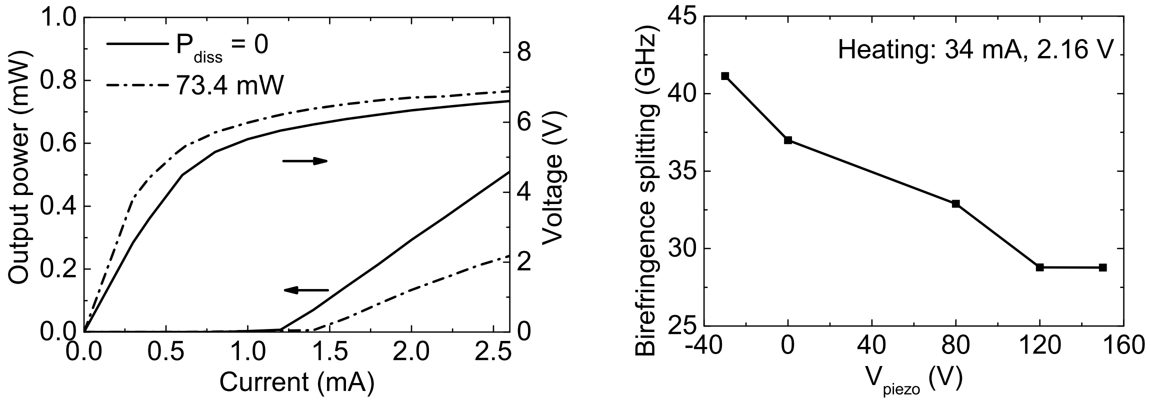

Fig. 5: Light–current–voltage curves of the VCSEL at 0 and 73.4 mW dissipated power (left). Change of the birefringence splitting with increasing applied piezo voltage V_{piezo} at a constant heating current I_{H} and heating voltage V_{H} of 34 mA and 2.16 V, respectively (right).

ridge is oriented parallel to the stretching direction of the piezo transducer. With a fourth contact needle dipped into the glue next to the VCSEL array, the electrical circuit for laser operation is established. A schematic drawing of the integrated device is depicted in Fig. 4 (right). In the experiment, the heating current I_{H} is set constant and the applied piezo voltage V_{piezo} is increased in a few large steps (−30 V, 80 V, 120 V, and 150 V). Afterwards the heating current is increased. This is done for heating currents $I_{\mathrm{H}} = 0\,\mathrm{mA}$, 20 mA, 25 mA, 30 mA, and 34 mA. The maximum value is chosen in order to prevent contact damage by overheating. Optical spectra are measured for every combination as well as the LIV curves for the different heating currents at $V_{\mathrm{piezo}} = 0\,\mathrm{V}$ to see the influence on the laser output. Figure 5 (left) shows the laser characteristics without heating (solid line) and at the peak dissipated power of $\hat{P}_{\mathrm{diss}} = \hat{I}_{\mathrm{H}} \cdot \hat{V}_{\mathrm{H}} = 34\,\mathrm{mA} \cdot 2.16\,\mathrm{V} = 73.4\,\mathrm{mW}$ (dash-dotted line). The output power at $I_{\mathrm{L}} = 2.6\,\mathrm{mA}$ is reduced by about a factor of two from $P_{0\,\mathrm{mA}} = 0.51\,\mathrm{mW}$ to $P_{34\,\mathrm{mA}} = 0.24\,\mathrm{mW}$. The threshold voltage $V_{\mathrm{th}} = 5.8\,\mathrm{V}$ can be attributed to the high back side contact resistance. In Fig. 5 (right) the birefringence splitting B is displayed for increasing applied piezo voltage V_{piezo} at a dissipated power $P_{\mathrm{diss}} = 73.4\,\mathrm{mW}$. Surprisingly a decrease of B for increased V_{piezo} from $B_{-30\,\mathrm{V}} = 41\,\mathrm{GHz}$ to $B_{150\,\mathrm{V}} = 32\,\mathrm{GHz}$ is measured. This behavior was verified with repeated measurements. Currently no explanation for this effect can be given.

5. Conclusion

We have shown mechanical stretching via piezoelectric substrates as a possibility for electrical birefringence tuning in VCSELs. For a VCSEL array with a sample thickness of 28 µm we have obtained a peak birefringence splitting of 67 GHz. We have observed an increase of the birefringence splitting with decreasing sample thickness. The glue between the sample and the piezoelectric transducer reduces the strain transferred to the laser. Automated minimum glue deposition and sample positioning are expected to improve reproducibility and to yield higher birefringence. First measurements combining thermally induced strain and piezo-mechanical stretching were done. Unexpectedly a decrease of B for increased V_{piezo} at a constant dissipated power P_{diss} was found. Further investigations are in progress.

6. Acknowledgment

The authors thank Susanne Menzel for fruitful discussions and technical support and Matthias Wehl for performing some of the measurements. Furthermore they are grateful to Philips Photonics GmbH for the provision of the VCSEL samples. This work is funded by the German Research Foundation (DFG) grant ‘Ultrafast Spin Lasers for Modulation Frequencies in the 100 GHz Range’.

References

[1] R. Michalzik, “VCSEL Fundamentals”, Chap. 2 in *VCSELs – Fundamentals, Technology and Applications of Vertical-Cavity Surface-Emitting Lasers*, R. Michalzik (Ed.), pp. 19–75. Berlin: Springer, 2013.

[2] D.M. Kuchta, A.V. Rylyakov, F.E. Doany, C.L. Schow, J.E. Proesel, C.W. Baks, P. Westbergh, J.S. Gustavsson, and A. Larsson, “A 71-Gb/s NRZ modulated 850-nm VCSEL-based optical link”, *IEEE Photon. Technol. Lett.*, vol. 27, pp. 577–580, 2015.

[3] T. Zuo, L. Zhang, J. Zhou, Q. Zhang, E. Zhou, and G.N. Liu, “Single lane 150-Gb/s, 100-Gb/s and 70-Gb/s 4-PAM transmission over 100-m, 300-m and 500-m MMF using 25-G class 850nm VCSEL”, in Proc. *Europ. Conf. on Opt. Commun., ECOC 2016*, pp. 974–976, Düsseldorf, Germany, Sept. 2016.

[4] N.C. Gerhardt and M.R. Hofmann, “Spin-controlled vertical-cavity surface-emitting lasers”, *Advances in Optical Technol.*, vol. 2012, pp. 268949-1–15, 2012.

[5] M. Lindemann, T. Pusch, R. Michalzik, N.C. Gerhardt, and M.R. Hofmann, "Frequency tuning of polarization oscillations: towards high-speed spin-lasers", *Appl. Phys. Lett.*, vol. 108, pp. 042404-1–4, 2016.

[6] H. Höpfner, M. Lindemann, N.C. Gerhardt, and M.R. Hofmann, "Controlled switching of ultrafast circular polarization oscillations in spin-polarized vertical-cavity surface-emitting lasers", *Appl. Phys. Lett.*, vol. 104, pp. 022409-1–4, 2014.

[7] T. Pusch, M. Lindemann, N.C. Gerhardt, M.R. Hofmann, and R. Michalzik, "Vertical-cavity surface-emitting lasers with birefringence splitting above 250 GHz", *Electron. Lett.*, vol. 51, pp. 1600–1602, 2015.

[8] A.K. Jansen van Doorn, M.P. van Exter, and J.P. Woerdman, "Tailoring the birefringence in a vertical-cavity semiconductor laser", *Appl. Phys. Lett.*, vol. 69, pp. 3635–3637, 1996.

[9] T. Pusch, E. La Tona, M. Lindemann, N.C. Gerhardt, M.R. Hofmann, and R. Michalzik, "Monolithic vertical-cavity surface-emitting laser with thermally tunable birefringence", *Appl. Phys. Lett.*, vol. 110, pp. 151106-1–3, 2017.

[10] K.D. Jöns, R. Hafenbrak, R. Singh, F. Ding, J.D. Plumhof, A. Rastelli, O.G. Schmidt, G. Bester, and P. Michler, "Dependence of the redshifted and blueshifted photoluminescence spectra of single $In_xGa_{1-x}As/GaAs$ quantum dots on the applied uniaxial stress", *Phys. Rev. Lett.*, vol. 107, pp. 217402-1–5, 2011.

[11] K. Shayegan, K. Karrai, Y.P. Shkolnikov, K. Vakili, E.P. De Porterre, and S. Manus, "Low-temperature, in situ tunable, uniaxial stress measurements in semiconductors using a piezoelectric actuator", *Appl. Phys. Lett.*, vol. 83, pp. 5235–5237, 2003.

[12] T. Pusch, M. Bou Sanayeh, M. Lindemann, N.C. Gerhardt, M.R. Hofmann, and R. Michalzik, "Birefringence tuning of VCSELs", *Proc. SPIE*, vol. 9892, pp. 989222-1–6, 2016.

[13] M.P. van Exter, A.K. Jansen van Doorn, and J.P. Woerdman, "Electro-optic effect and birefringence in semiconductor vertical-cavity lasers", *Phys. Rev. A*, vol. 56, pp. 854–853, 1996.

[14] P.S. Zory Jr., *Quantum Well Lasers* (2nd ed.), San Diego: Academic Press, 1993.

Operating Optically Current-Confined VCSELs With an External Laser Beam

Sven Bader and Mohamed Elattar

Optically controlled current confinement is an oxide- and regrowth-free method in vertical-cavity surface-emitting lasers (VCSELs) to funnel carriers in very close vicinity to the active layers to reach low lasing threshold currents. The essential component to steer the current flow through the laser is a monolithically integrated phototransistor (PT) in the cavity, operating as an optical switch. The PT layers become locally conductive where the highest photon density is reached in the resonator and establish the current aperture. Illuminating parts of the VCSEL by a focused external laser beam changes this spatial photon distribution by introducing additional photons. We demonstrate the possibility of manipulating the location of the current aperture as well as influencing the light–current characteristics by varying the power and wavelength of the external laser.

1. Introduction

Diverse novel fields of applications with the main scope of optical sensing and short-distance data communications have continuously increased the importance of vertical-cavity surface-emitting lasers in the past years [1]. However, not only the variety of applications contributed to the success but also profound VCSEL research and development played an important part. This resulted in more efficient, faster, and inexpensive lasers. Extending the device lifetime is a concern which is affected by several factors. One of them is the buried insulating oxide ring which funnels the current flow through its centered opening — the current aperture [2]. This leads to a strong local increase of current density and thus reduces the lasing threshold current. However, during the manufacture of this current aperture via selective wet-thermal oxidation, the high aluminum content AlGaAs layers of the top mirror reduce their volume when transformed to an oxide. Typically the current aperture is located close to the active zone. As a result, mechanical strain is directly transferred to the active layers of the VCSEL, which might affect the very-long-term reliability of the VCSEL [3]. Oxide-confined VCSELs are most popular for commercial use, however, alternative current confinement techniques like mesa-etching [4], proton implantation [5], or epitaxial regrowth [6, 7] still exist. Although the performance of those devices may be equivalent to that of oxidized VCSELs, the manufacturing effort is comparably high, in particular if regrowth is involved.

We have developed an optically controlled method for current confinement, where an epitaxially integrated phototransistor — configured as an optical switch — defines the current flow through the device [8]. The concept of this oxide- and regrowth-free approach

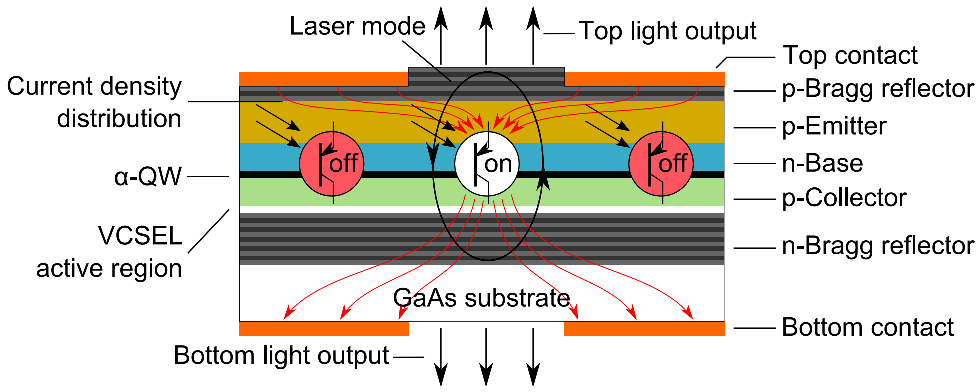

Fig. 1: Schematic layer structure of an optically current-confined VCSEL with integrated PT, which is configured as an optical switch. The PT opens where the highest lateral photon density is reached, thus the location of the current aperture strongly depends on the quality factor of the resonator and can be affected by etching the top mirror (i.e., under the top metal contact).

is discussed in detail in Sect. 2. The required photons for switching the PT conductive can either originate directly from the active zone of the PT-VCSEL or be injected into the resonator by an external laser beam. This new technique of defining and manipulating the current aperture is introduced in Sect. 3, where also its influence on the turn-on behavior of parallel-driven PT-VCSEL arrays will be investigated. Section 4 analyzes the impact of varying the output power and wavelength of the external laser on the light output curves of large-area VCSELs.

2. Optically Controlled Current Confinement

Optically current-confined PT-VCSELs combine the advantages of a strain-free epitaxial structure with a simple manufacturing process. Compared to existing methods, mentioned in Sect. 1, no physical barriers must be post-processed in order to partially block the current flow. Our approach epitaxially integrates a PT directly into the cavity where also the active zone of the VCSEL is located (see Fig. 1). As in a standard pnp-bipolar junction transistor configuration, the PT consists of p-emitter, n-base, and p-collector layers, however, except for the external base terminal. The base current I_B is generated in a dedicated quantum well (α-QW) between the base and collector layer by absorbing photons in the resonator. Actually, I_B is a photocurrent which can be calculated as

$$I_\mathrm{B} = (1 - \exp(-\alpha d)) \cdot \frac{q\lambda}{hc} \cdot P, \tag{1}$$

where α is the absorption coefficient and d is the width of the α-QW, q is the elementary charge, h is Planck's constant, and c the vacuum velocity of light with wavelength λ and optical power P in the cavity.

Ramping up the drive current, initially the PT acts as an insulating barrier which only allows leakage current to flow. However, this current already causes spontaneous emission, generated in the InGaAs QWs of the active zone. These photons get partly absorbed in

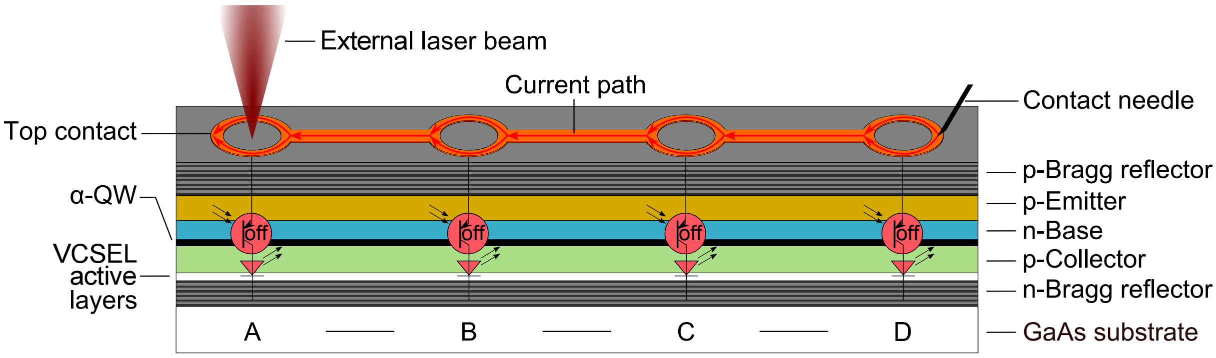

Fig. 2: Schematic layout of parallel-driven PT-VCSELs which are defined by four interconnected surface metal contact rings. The external laser beam is focused at position A and introduces additional photons in the resonator.

the α-QW and produce the base current (according to (1)). The GaAs-based PT-VCSEL is designed to absorb exclusively in the 1040 nm range via an InGaAs α-QW. Once I_{B} exceeds a certain threshold value, which mainly depends on the current gain, the lateral region of the PT with the highest photon density switches into a conductive state. The drive current now funnels through this current aperture, generates more photons and keeps this PT area open and stable in diameter. After reaching the threshold current density, the PT-VCSEL starts lasing. The location of the current aperture strongly depends on the spatial photon density during the turn-on of the device. It can either be influenced by the quality factor of the resonator, determined by, e.g., the number of top mirror pairs (see Fig. 1) or surface relief structures [9]. Alternatively, as will be explained in Sect. 3, additional photons can be introduced into the cavity by a focused tunable laser beam. Functional devices can be processed with a few cleanroom steps, not requiring the critical wet-thermal oxidation. Thus, the problematic strain close to the active zone is eliminated, which could extend the lifetime of the VCSELs. Moreover, the optimized spatial overlap between the current and photon distribution could lead to more efficient lasers.

3. External Current Aperture Definition and Manipulation

To modify the location of the current aperture during the turn-on of the PT-VCSEL means to influence the spatial photon distribution in the resonator. This can be done by incrementing the number of photons via light injection. We employ an external tunable laser with an optical output power of up to 35 mW and a wavelength range from 990 to 1075 nm. The wavelength of these photons must be chosen according to the resonance dip in the reflection spectrum of the PT-VCSEL to ensure the best possible injection efficiency. Owing to the red-shift of the spectrum caused by internal heating, the wavelength of the external laser needs to be readjusted when changing the drive current.

To qualitatively investigate the influence of additional photons in the cavity of PT-VCSELs, we have grown a test sample by molecular beam epitaxy on an n-doped GaAs wafer. The resonator is formed by p- and n-doped AlGaAs/GaAs Bragg mirrors consisting of 29 and 26.5 layer pairs, respectively. The calculated threshold gain is 1522 cm^{-1},

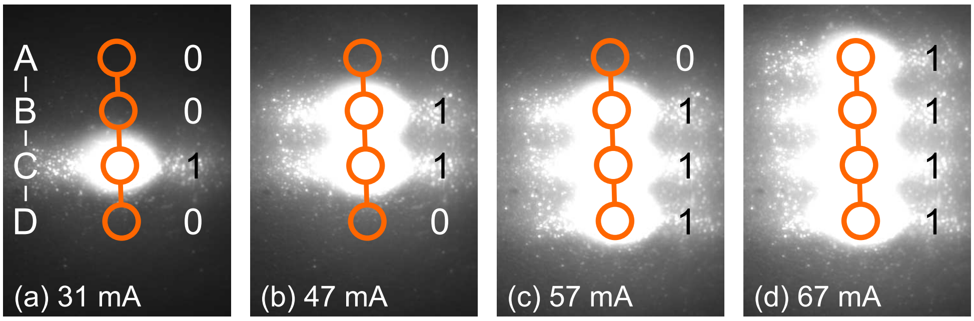

Fig. 3: CCD camera images of the bottom side of spontaneously emitting PT-VCSELs according to Fig. 2. The top metal contact structure is highlighted in orange. "0" and "1" represent the off-/on-state of each PT, respectively, and the turn-on currents where the individual PTs become locally conductive are displayed at the bottom. As in Fig. 2 the needle contacts an outer ring at position D. The turn-on order is C–B–D–A.

and the absorption coefficient of the α-QW is estimated to be $\approx 3500\,\text{cm}^{-1}$. To reach strong current confinement, the current gain β is kept very low [10], namely $\beta \approx 2$ in this sample.

We have processed one-dimensional arrays of four parallel-driven PT-VCSELs (see Fig. 2). Ti/Pt/Au contact rings on the surface with 100 µm inner diameter define each device. The rings are interconnected by 100 µm long metal lines with a width of 30 µm. The back side of the substrate was kept free from metal to guarantee an unobstructed view at the light output pattern of the PT-VCSEL. The sample holder has a dedicated opening for transmission of the bottom-emitted light. A large-area n-contact is established between the sample and the Au-coated vacuum holder. The current source is connected to the sample holder and to a tungsten needle which contacts the top metalization of device D. In addition to light versus current measurements, the setup allows to take CCD camera images from the bottom side of the wafer and obtain new insights about the turn-on process of the laser structure. Without external laser illumination, the turn-on order of these samples always follows a consistent routine [11]. Figure 3 shows the camera images taken from the back side of the structure during the turn-on process. Ramping up the current, during dark-current operation (before 31 mA), there is an almost homogeneous current flow over the whole width of the structure, which already generates faint spontaneous emission in the active zone. Finally, at 31 mA the PT with the highest leakage current of the base–collector junction begins to open (here at position C). Subsequently, while further increasing the drive current, spontaneous photons reach the adjacent regions and successively turn these PTs on. At 67 mA, all four parallel-driven PT-VCSELs are switched into a conductive state and show spontaneous emission. For still higher currents the needle-contacted array begins to lase where owing to lateral ohmic losses the highest current density is reached.

To manipulate the turn-on order from Fig. 3, we repeat the experiment while focusing the external laser beam at different positions on the surface (see Fig. 2). The power of the laser was set to 6.4 mW and the wavelength was chosen as 1038 nm according to the reflection characteristics. Initially, the drive current was set to 25 mA to operate in

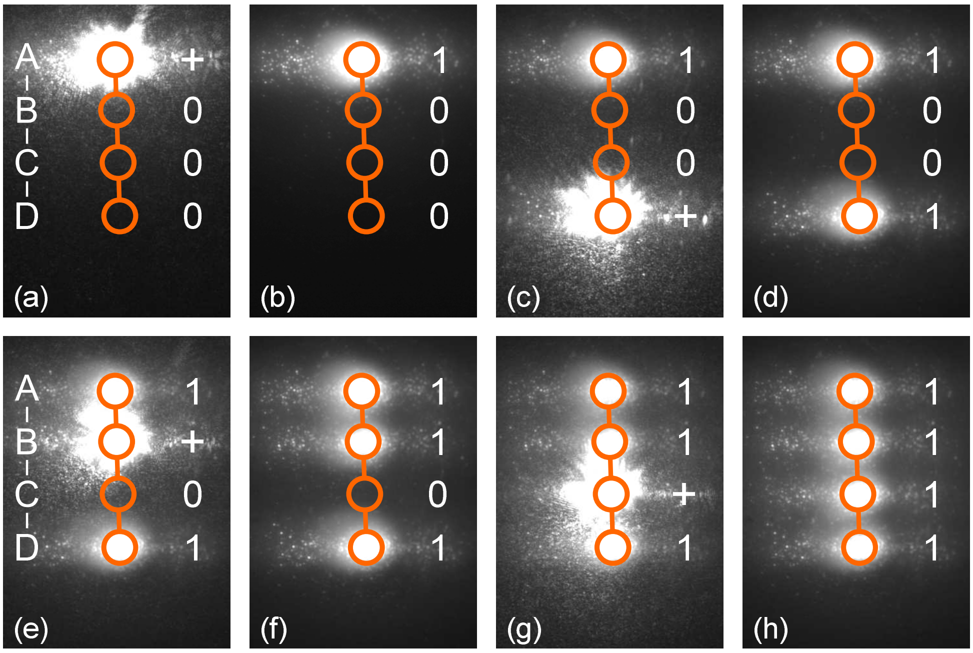

Fig. 4: CCD camera images of the bottom side of the PT-VCSEL arrangement from Fig. 2 at a constant current of 25 mA. The white "+" indicates the contact ring into which the external laser beam is focused. The images (a)–(h) illustrate a sequential experiment in which the external laser is switched on and off to open an additional PT. The stray light in the vicinity of the position "+" in images (a), (c), (e), and (g) originates from external laser emission transmitted through the complete device. The turn-on order of the one-dimensional array can be changed in any arbitrary way (here: A–D–B–C).

the dark-current mode of the PT-VCSELs. After directing the external laser beam to position A of the contact structure, the additional injected photons turned this PT into a conductive state even after switching the laser off again. As proven by Fig. 4, the turn-on order now exclusively depends on the position of the laser beam. Since the drive current is kept constant during the entire experiment, the turn-on current of the PTs was consequently decreased compared to the results in Fig. 3.

4. Impact of External Power and Wavelength

During the previous investigations, the optical power and wavelength of the external laser beam were kept constant. However, since the amount of injected photons is crucial for the turn-on of the PT-VCSEL, the output power of the external laser consequently has a direct influence on the device behavior. The impact of the photon wavelength depends strongly on the temperature-dependent emission spectrum of the PT-VCSEL. For functional devices it is essential to design the resonator and the α-QW in the same wavelength range. Since the diameter of the focused external laser beam is about 60 µm, a large-diameter PT-VCSEL device with 230 µm metal contact opening was chosen for the light–current (LI) measurements. This size is a compromise between small-diameter and large-area devices. On the one hand, in small devices, the large laser spot size would

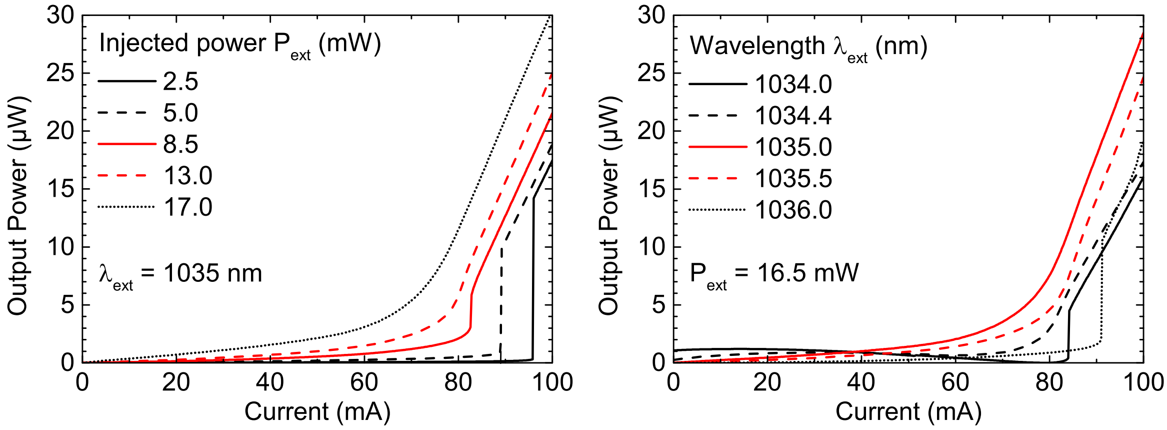

Fig. 5: Measured LI curves of a bottom-emitting PT-VCSEL with a contact ring diameter of 230 µm while varying the injected optical power (left) and the wavelength of the external laser source (right).

switch the whole mesa conductive, which would result in mesa current confinement. On the other hand, oversized samples are problematic owing to the higher ohmic resistance of the long lateral current paths between contact ring and current aperture. Figure 5 (left) depicts the LI measurements for different optical input powers P_{ext} from the external laser. The wavelength is kept constant to $\lambda_{\text{ext}} = 1035$ nm. It is obvious that the turn-on current of the PT (determined by the step-like rise of output power) decreases while intensifying the illumination, namely more photons per time are incorporated into the resonator, which helps to reach the threshold base current at lower drive currents. Also, instead of a step-like behavior, the LI curves show a more and more gradual onset of lasing operation. The step results from a sudden transition from an insulating to a conductive state of the PT. Simultaneously, the majority of carriers funnel through the newly established optically defined current aperture, which increases abruptly the current density and leads to a higher photon generation until finally stimulated emission is reached. This step is also detectable in the current–voltage (IV) characteristics, indicated as a sharp negative differential resistance region. By incorporating more external photons into the resonator, at some point (here between 8.5 and 13.0 mW) the PT switches conductive before the lasing threshold current density is reached. In this case the drive current must be further increased to reach lasing, which results in a smooth continuous LI curve and a diode-like IV characteristic. The decrease of the lasing threshold current with increasing input power can be explained by the accumulation of carriers in the α-QW as a result of absorption and the subsequent reduction of the absorption coefficient α from (1) (bleaching effect). Lower internal losses in the resonator then raise the slope of the LI curve. Concurrently, more external laser light can propagate through the device, which is detected by the optical power meter on the bottom side.

The influence of changes of the external laser wavelength λ_{ext} on the LI curve of the PT-VCSEL is illustrated in Fig. 5 (right). The external laser power was kept constant at 16.5 mW. The wavelength range for this investigation was chosen to be smaller than 1040 nm to ensure absorption of photons in the α-QW. Starting with 1034 nm (thus blueshifted to Fig. 5 (left)) the already known step function in the LI graph appears again (it disappeared at 13 mW already in the left figure part). Since λ_{ext} is outside the resonance dip of the laser at around 1035 nm, more photons of the external laser are reflected at the top surface and do no affect the turn-on process at 84 mA. However, they partly enter the resonator in the 0 . . . 30 mA drive current region and already create a current aperture. This effect is noticeable in the local maximum of the output power at about 15 mA caused by transmitted external laser light through the device, which is also responsible for finite light detection at zero current. While further increasing the current (and therefore red-shifting the spectrum), the influence of the external laser almost disappears again and the internally (in the active layers) generated photons at these low drive currents still do not suffice to keep the aperture open. This is the case only at 84 mA, as indicated by the step in the LI curve. By slightly increasing λ_{ext}, more external photons are injected at higher VCSEL currents. At 1035 nm the resonance dip of the PT-VCSEL is at the perfect position — leading to low turn-on currents — to support the establishment of the current aperture and subsequently keeping it open only by internally generated photons, even when the external amount of photons decreases while further increasing the current (and red-shifting the spectrum). Raising the wavelength to 1036 nm, the external photons cannot influence the turn-on process because they are able to enter the resonator only at high drive currents after the turn-on of the PT already happened internally. These measurements give valuable insight into the the turn-on behavior of PT-VCSELs and demonstrate the difficulty to mutually adjust the injection wavelength, the power, and the drive current to minimize the turn-on and lasing threshold currents.

5. Conclusion and Outlook

We have discussed the concept of optically controlled current confinement in VCSELs that contain a phototransistor in the cavity. We have presented detailed studies about the optical manipulation of the current aperture in PT-VCSELs by using a tunable laser beam. The possibility of externally defining the location of the current aperture in parallel-driven structures has been demonstrated. We have also investigated the impact of varying the optical power and wavelength of the external laser on the turn-on behavior of the PT-VCSELs and were capable to shift the turn-on current of the PT towards lower values without changing the current gain of the PT. The new insights help to optimize the next generation of PT-VCSELs regarding the turn-on characteristics as well as to motivate future PT-integrated devices like light-emitting diodes which could possibly be controlled by an external light source.

Acknowledgment

The authors thank Philips Photonics GmbH for the project support and the MBE growth of the PT-VCSEL wafer. Furthermore the authors are grateful to Dr.-Ing. Philipp Gerlach for many superb discussions and the fruitful cooperation. The technical assistance of Susanne Menzel and Rudolf Rösch in the cleanroom is highly appreciated.

References

[1] R. Michalzik (Ed.), *VCSELs — Fundamentals, Technology and Applications of Vertical-Cavity Surface-Emitting Lasers*, Springer Series in Optical Sciences, vol. 166, Berlin: Springer-Verlag, 2013.

[2] D.L. Huffaker, D.G. Deppe, K. Kumar, and T.J. Rogers, "Native-oxide defined ring contact for low threshold vertical-cavity lasers", *Appl. Phys. Lett.*, vol. 65, pp. 97–99, 1994.

[3] B.M. Hawkins, R.A. Hawthorne III, J.K. Guenter, J.A. Tatum, and J.R. Biard, "Reliability of various size oxide aperture VCSELs", in Proc. *52nd Electron. Comp. and Technol. Conf., ECTC 2002*, pp. 540–550. San Diego, CA, USA, May 2002.

[4] J.L. Jewell, A. Scherer, S.L. McCall, Y.H. Lee, S. Walker, J.P. Harbison, and L.T. Florez, "Low-threshold electrically pumped vertical-cavity surface-emitting microlasers", *Electron. Lett.*, vol. 25, pp. 1123–1124, 1989.

[5] M. Orenstein, A.C. Von Lehmen, C. Chang-Hasnain, N.G. Stoffel, J.P. Harbison, L.T. Florez, E. Clausen, and J.E. Jewell, "Vertical-cavity surface-emitting InGaAs/GaAs lasers with planar lateral definition", *Appl. Phys. Lett*, vol. 56, pp. 2384–2386, 1990.

[6] M. Ortsiefer, W. Hofmann, J. Rosskopf, and M.C. Amann, "Long-Wavelength VCSELs with Buried Tunnel Junction", Chap. 10 in *VCSELs*, R. Michalzik (Ed.), pp. 321–351, Berlin: Springer-Verlag, 2013.

[7] X. Yang, M. Li, G. Zhao, Y. Zhang, S. Freisem, and D. Deppe, "Small-sized lithographic single-mode VCSELs with high power conversion efficiency", in *Vertical-Cavity Surface-Emitting Lasers XIX*, C. Lei, K.D. Choquette (Eds.), Proc. SPIE 9381, pp. 93810R-1–6, 2015.

[8] S. Bader, P. Gerlach, and R. Michalzik, "Optically controlled current confinement in vertical-cavity surface-emitting lasers", *IEEE Photon. Technol. Lett.*, vol. 28, pp. 1309–1312, 2016.

[9] H.J. Unold, S.W.Z. Mahmoud, R. Jäger, M. Grabherr, R. Michalzik, and K.J. Ebeling, "Large-area single-mode VCSELs and the self-aligned surface relief", *IEEE J. Select. Topics Quantum Electron.*, vol. 7, pp. 386–392, 2001.

[10] S. Bader, P. Gerlach, and R. Michalzik, "VCSELs with optically controlled current confinement: experiments and analysis", in *Semiconductor Lasers and Laser Dynamics VII*, K.P. Panajotov, M. Sciamanna, A.A. Valle, R. Michalzik (Eds.), Proc. SPIE 9892, pp. 989208-1–6, 2016.

[11] S. Bader, P. Gerlach, and R. Michalzik, "Optically controlled current confinement in parallel-driven VCSELs", in Online Digest *Conf. on Lasers and Electro-Optics, CLEO/Europe 2017*, paper CB-3.4, one page. Munich, Germany, June 2017.

Refractive Index Measurement by Gain- or Loss-Induced Resonance

Markus Miller

Using a semiconductor optical resonator consisting of a Bragg reflector and a total internal reflection mirror, a refractive index sensor can be realized. When absorption or gain is present within the resonator, sharp resonance peaks in the reflectivity spectrum can be observed. Since the phase of the reflected light at total internal reflection depends on the refractive indices at the interface, the resonance wavelength is related to the refractive indices. Analytical calculations and transfer matrix simulations are presented to explain the measurement principle in detail and show the potential of the new sensor approach.

1. Introduction

Refractive index sensors are widely used in industry, biology, and medicine for a variety of purposes like, for instance, the analysis of glucose concentration in honey, jam, or even blood. In order to achieve high-precision measurements and to reduce the size of the device compared to the traditional Abbe refractometer [1], new sensors based on surface plasmon resonance [2], optical fibers [3], or resonant optical tunneling [4] have been investigated and developed. Many of these approaches determine the refractive index from the spectral shift of a resonance that is related to the variation of the refractive index of the sample. Therefore, the spectral shift per refractive index unit as well as the spectral width of the resonance peak are important for precise measurements [5]. A high-quality resonator with high sensitivity to changes of refractive indices fulfills these requirements.

2. Measurement Principle

The measurement principle of the presented sensor is based on a resonator providing multiple beam interference to obtain sharp resonances and on total internal reflection producing an evanescent field for high sensitivity of the resonance wavelength to refractive index changes. A side-view of the structure is shown in Fig. 1. The device can be regarded as a half vertical-cavity surface-emitting laser obtained by cutting through the active zone in lateral direction. Thus the device consists of the substrate, the remaining distributed Bragg reflector (DBR), the active region with refractive index $\bar{n}_1$ and the sensing area at the bottom interface between the device and the adjacent medium of refractive index $\bar{n}_2$. For $\bar{n}_2 < \bar{n}_1$ and for angles Θ_1 larger than the critical angle $\Theta_\mathrm{c} = \arcsin(\bar{n}_2/\bar{n}_1)$, total internal reflection occurs at the bottom interface. In this case only an evanescent field penetrates into the adjacent medium and the interface acts as an ideal mirror with

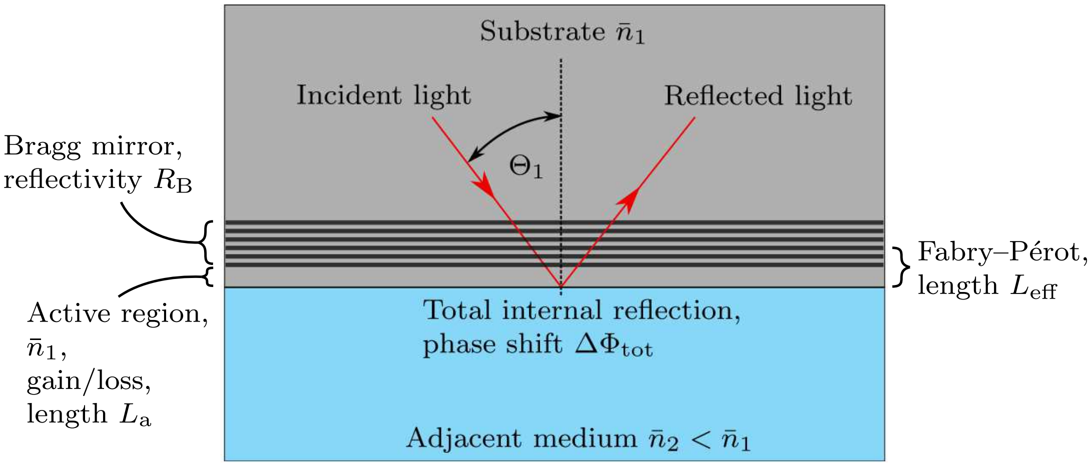

Fig. 1: Scheme of the measurement device consisting of substrate, DBR, active region, and the bottom interface to the adjacent medium.

a power reflectivity $R = P_\mathrm{r}/P_\mathrm{i} = 1$. The phase of the reflected light is shifted by $\Delta\Phi_\mathrm{tot}$. In the case of TE-polarized incident light, the phase shift $\Delta\Phi_\mathrm{tot,TE}$ is given by [6]

$$\Delta\Phi_\mathrm{tot,TE} = 2\arctan\frac{\sqrt{\bar{n}_1^2\sin^2\Theta_1 - \bar{n}_2^2}}{\bar{n}_1\cos\Theta_1} \tag{1}$$

and depends on the refractive indices $\bar{n}_1$ and $\bar{n}_2$ of the interface materials.

Total internal reflection and the DBR form a Fabry–Pérot cavity of effective length L_eff and a corresponding roundtrip phase Φ_FP in the TE-case of

$$\Phi_\mathrm{FP} = \frac{4\pi\bar{n}_\mathrm{eff}L_\mathrm{eff}\cos\Theta_1}{\lambda} - \Delta\Phi_\mathrm{tot,TE}, \tag{2}$$

where λ is the free-space wavelength and $\bar{n}_\mathrm{eff}$ is the effective refractive index of the resonator. When the roundtrip phase fulfills the condition $\Phi_\mathrm{FP} = m\cdot 2\pi$ with integer m, resonances occur at discrete wavelengths λ_m given by

$$\lambda_m = \frac{4\pi\bar{n}_\mathrm{res}L_\mathrm{eff}\cos\Theta_1}{m\cdot 2\pi + \Delta\Phi_\mathrm{tot,TE}}. \tag{3}$$

Thus, for a fixed angle of incidence, the resonance wavelength λ_m is a function of the refractive index of the adjacent medium, as the phase shift of total internal reflection $\Delta\Phi_\mathrm{tot,TE}$ depends on the refractive indices of both materials at the interface. Hence, for known device parameters, the refractive index of the adjacent medium can be obtained from the resonance wavelength.

Assuming a (positive or negative) absorption coefficient α in the active region of length L_a in an otherwise lossless device, the reflectivity as a function of the roundtrip phase Φ_FP is given by

$$R = \frac{(\sqrt{R_\mathrm{B}} - \exp(-\alpha L_\mathrm{a}))^2 + 4\sqrt{R_\mathrm{B}}\exp(-\alpha L_\mathrm{a})\sin^2(\Phi_\mathrm{FP}/2)}{(1-\sqrt{R_\mathrm{B}}\exp(-\alpha L_\mathrm{a}))^2 + 4\sqrt{R_\mathrm{B}}\exp(-\alpha L_\mathrm{a})\sin^2(\Phi_\mathrm{FP}/2)}, \tag{4}$$

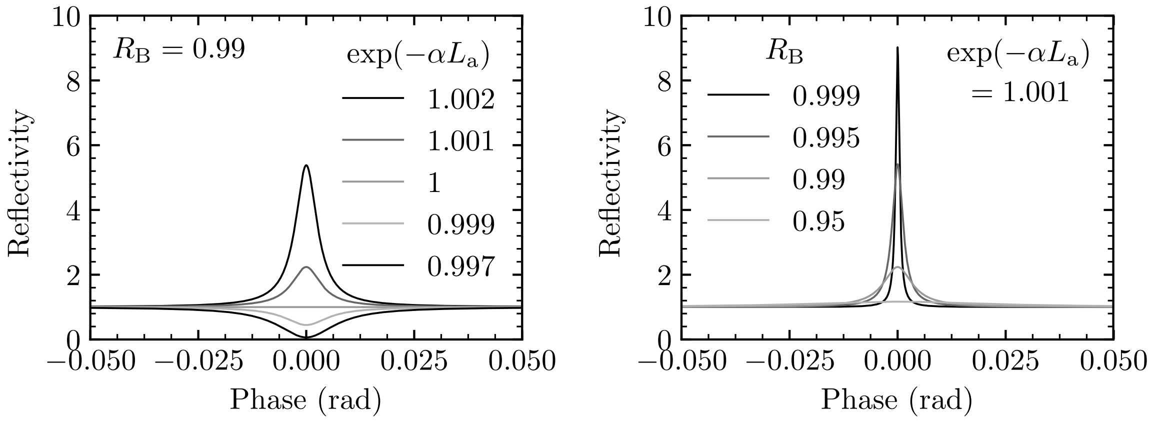

Fig. 2: Reflectivity R according to (4) plotted over the roundtrip phase for different absorption $\exp(-\alpha L_a)$ with fixed reflectivity R_B (left) and different Bragg reflectivities R_B with fixed amplification $\exp(-\alpha L_a) = 1.001$ (right).

where R_B is the reflectivity of the DBR and the reflectivity of the total internal reflection mirror is set to one. Equation (4) is plotted in Fig. 2 as function of the roundtrip phase. On the left-hand side the reflectivity is shown for different absorption and amplification $\exp(-\alpha L_a)$ in the active region and a fixed Bragg reflectivity, whereas on the right-hand side the reflectivity is displayed for a fixed amplification but varying DBR reflectivities R_B. For a phase equal to zero or $m \cdot 2\pi$, a clear dip or peak can be observed in Fig. 2, depending on the sign of the absorption coefficient. In the lossless case, no resonance occurs because of the ideal total internal reflection mirror. The height and half-width of the resonance depend on the DBR reflectivity as well as the absorption or gain. With increasing Bragg reflectivity the half-width of the resonance peak shrinks, as known for increasing finesse of a Fabry–Pérot resonator. Especially when gain is present within the active zone, the peak height and half-width depend strongly on the mirror reflectivity, resulting in a narrow, high peak for high DBR reflectivity.

3. Transfer Matrix Simulations

The transfer matrix method is a proper one-dimensional simulation approach to investigate the behavior of layered media devices, as it is possible to calculate reflectivity spectra as well as field distributions within the structure [7]. Therefore this method is used to design and analyze the structure of the presented sensor device based on III–V semiconductor materials. III–V compounds offer the possibility to incorporate quantum wells in the structure as absorbing or amplifying layers. All simulations presented in the following assume TE-polarized incident light.

Figure 3 shows the refractive index profile of the designed layer structure on the left-hand side and corresponding reflectivity spectra for normal incidence on the right side. The layer structure consists of a GaAs substrate on top, followed by 15 Bragg mirror pairs with GaAs of assumed refractive index equal to 3.6 as high-index layer and AlAs of refractive index equal to 3 as low-index layer. A 10 nm InGaAs quantum well of

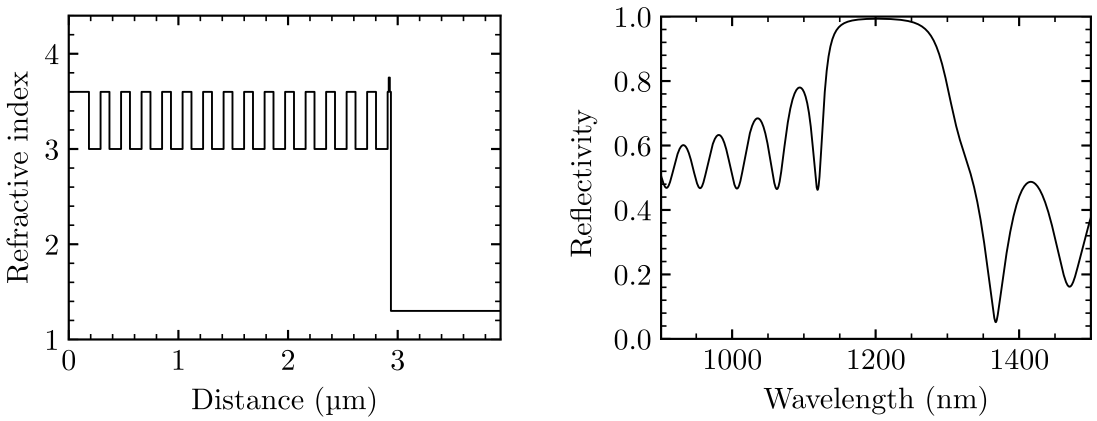

Fig. 3: Semiconductor layer sequence of the device containing 15 Bragg mirror pairs and a single quantum well (left) with corresponding reflectivity spectrum for normal incidence (right).

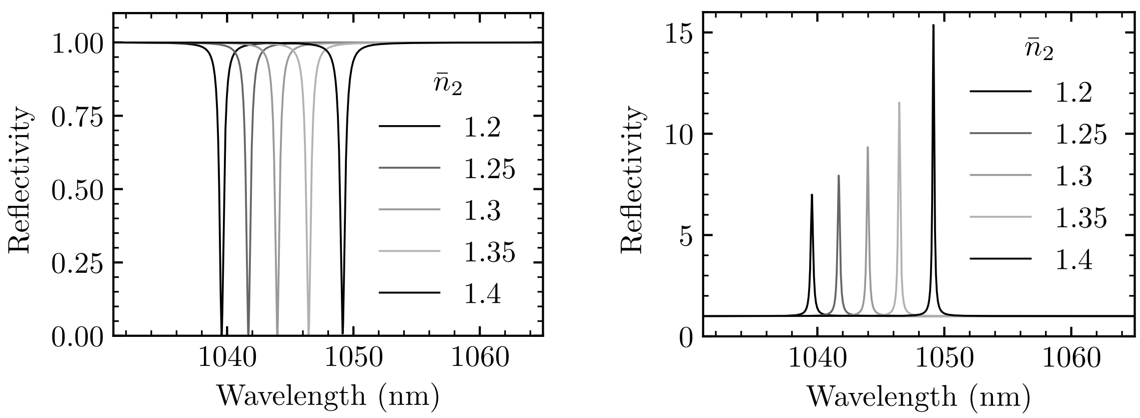

Fig. 4: Calculated reflectivity spectra at fixed angle of incidence ($\Theta_1 = 30.5\,^\circ$) for different refractive indices of the sample with absorption (left) or gain (right) in the quantum well.

refractive index 3.75 incorporated in thin GaAs layers is placed between the DBR and the interface to the adjacent medium of refractive index $\bar{n}_2$. Dispersion is neglected in all simulations and absorption only occurs within the quantum well, as described by the intensity absorption coefficient α. The Bragg mirror in Fig. 3 is designed to achieve high reflectivity at wavelengths of 1040 nm for an angle of incidence of about $30.5\,^\circ$ to obtain total internal reflection at the bottom interface. Thus the reflectivity spectrum for normal incidence in Fig. 3 is shifted towards longer wavelengths of about 1200 nm and its maximum reflectivity is lower compared to the angled incidence case.

In Fig. 4 calculated reflectivity spectra of the designed structure for an angle of incidence of $\Theta_1 = 30.5\,^\circ$ and various refractive indices of the sample are shown for an absorption coefficient of $\alpha = 500\,\mathrm{cm}^{-1}$ on the left and a gain coefficient of $\alpha = -1000\,\mathrm{cm}^{-1}$ on the right. In both cases a red-shift of the resonance wavelength with increasing refractive indices $\bar{n}_2$ can be observed, as the phase shift due to total internal reflection decreases towards zero with increasing refractive index of the adjacent medium. The shift rate is

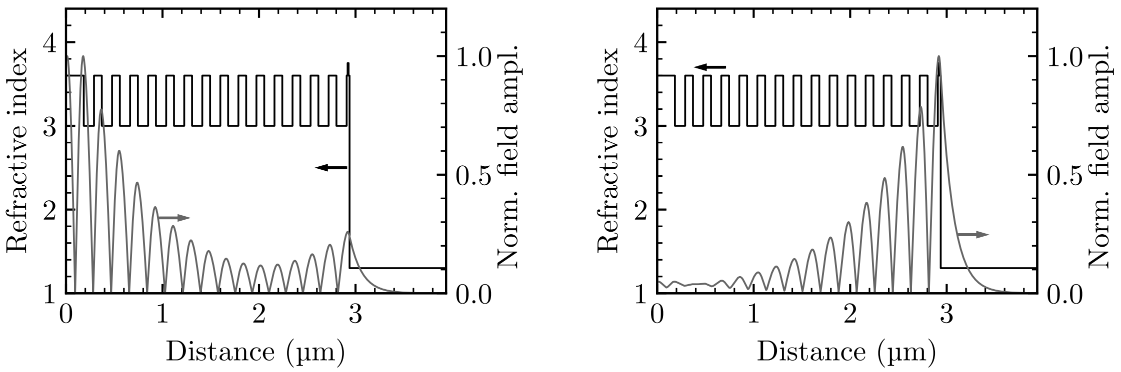

Fig. 5: Field distributions along the device for a sample with refractive index $\bar{n}_2 = 1.3$, a quantum well absorption coefficient $\alpha = -1000\,\mathrm{cm}^{-1}$, and an angle of incidence $\Theta_1 = 30.5\,°$ for wavelengths $\lambda = 1030\,\mathrm{nm}$ (left) and $\lambda = 1044\,\mathrm{nm}$ (right).

$\Delta\lambda/\Delta\bar{n}_2 \approx 50\,\mathrm{nm}$. The depth or height of the resonance differs as the reflectivity of the DBR is wavelength-dependent. This effect is especially seen when gain is present within the quantum well.

Figure 5 shows the field distributions for an adjacent medium of refractive index $\bar{n}_2 = 1.3$ and a quantum well absorption coefficient $\alpha = -1000\,\mathrm{cm}^{-1}$ for a non-resonant case at $\lambda = 1030\,\mathrm{nm}$ on the left and resonant behavior at $\lambda = 1044\,\mathrm{nm}$ on the right. At the interface to the adjacent medium, the evanescent field with a penetration depth of less than 500 nm is observable in both plots. In the non-resonant case, the field amplitude is small at the interface and the quantum well position compared to the incident amplitude. In contrast, in the resonant case, the field amplitude is over 20 times larger at the quantum well compared to the incident amplitude. Thus, the interaction with the quantum well is strong in the resonant case, leading to high absorption or amplification, depending on the excitation level of the quantum well. The small penetration depth of the evanescent field makes the sensor sensitive to refractive index changes of thin layers.

4. Conclusion

The presented refractive index measurement principle shows high potential as it is capable of measuring refractive indices over a wide range with high accuracy. The device structure is fairly simple and can be fabricated with common semiconductor epitaxial growth technologies. Of course, in a next step, the theoretical potential must be validated in experiments. Therefore, the coupling of the incident light into the semiconductor substrate to achieve total internal reflection at the bottom interface has to be considered. As the index contrast between air and GaAs is high, no direct light coupling into a planar GaAs slab to achieve the necessary angle above the critical angle in the semiconductor device is possible. In order to achieve sufficiently large angles of incidence at the interface, input light coupling via prisms or diffraction gratings can provide a solution.

References

[1] W. Boyes (Ed.), *Instrumentation Reference Book* (4th ed.), Burlington, MA, USA: Butterworth-Heinemann, 2010.

[2] J. Zeng and D. Liang, "Application of fiber optic surface plasmon resonance sensor for measuring liquid refractive index", *J. Intell. Material Syst. Struct.*, vol. 17, pp. 787–791, 2006.

[3] M. Naora, S. Taue, and H. Fukano, "Ultrasensitive fiber-optic refractive index sensor based on multimode interference with fiber-loop technique", in Proc. *22nd Microoptics Conference (MOC)*, pp. 130–131. Tokyo, Japan, Nov. 2017.

[4] A.Q. Jian, X.M. Zhang, W.M. Zhu, and M. Yu, "Optofluidic refractometer using resonant optical tunneling effect", *Biomicrofluidics*, vol. 4, pp. 043008-1–11, 2010.

[5] I.M. White and X. Fan, "On the performance quantification of resonant refractive index sensors", *Optics Express*, vol. 16, pp. 1020–1028, 2008.

[6] K.J. Ebeling, *Integrated Optoelectronics*, Berlin: Springer-Verlag, 1993.

[7] P. Yeh, *Optical Waves in Layered Media*, New York: John Wiley & Sons, 1988.

A New Approach to 3-D Imaging

Vignesh Devaki Murugesan

In this work, a new approach to three-dimensional (3-D) imaging using a continuously modulated electroabsorption modulator (EAM), a vertical-cavity surface-emitting laser (VCSEL) array, and a conventional complementary metal oxide semiconductor (CMOS) camera is presented. It is based on a time-of-flight method where the distance is indirectly obtained from the light intensity measured by a time-gated photon counter or charge integrator (i.e., a CMOS pixel). It is possible to acquire distance measurements for each pixel with accuracies up to few millimeters. Potential applications include augmented reality scenarios, face recognition systems in smartphones, industrial robotics, or machine vision.

1. Introduction

The acquisition of 3-D data is important for many control, navigation, and security scenarios [1]. Fast and reliable 3-D imaging has become a main requirement in commercial, industrial, and automotive applications. Currently different types of measuring techniques are available in the market for recording the 3-D information of an object or scene. Cameras for 3-D depth imaging using time-of-flight (TOF) methods have received a lot of attention recently for a number of reasons, including their low cost, compactness, and ability to obtain 3-D data at higher frame rates [2].

2. Working Principle of the Time-of-Flight Camera

2.1 Classification

Light waves based 3-D measurement techniques are broadly divided into active and passive approaches based on the source of light used, as shown in Fig. 1. Active measurement systems use a built-in illumination source (like laser or light-emitting diode) to probe the environment. Passive measurement systems rely on detecting backscattered ambient radiation to get the 3-D information [3]. Active measurement can be mainly classified in three categories:

1. Triangulation. In the triangulation technique, laser, camera, and point on the object to be measured form a triangle from which the distance is obtained.

2. Time-of-flight. Distance is measured by knowing the time difference between emitted and backscattered light wave and the velocity of light.

3. Interferometry. Distance is inferred from interference patterns of a coherent laser source. Interferometry is limited to distances approximately less than half the coherence length of the laser [3].

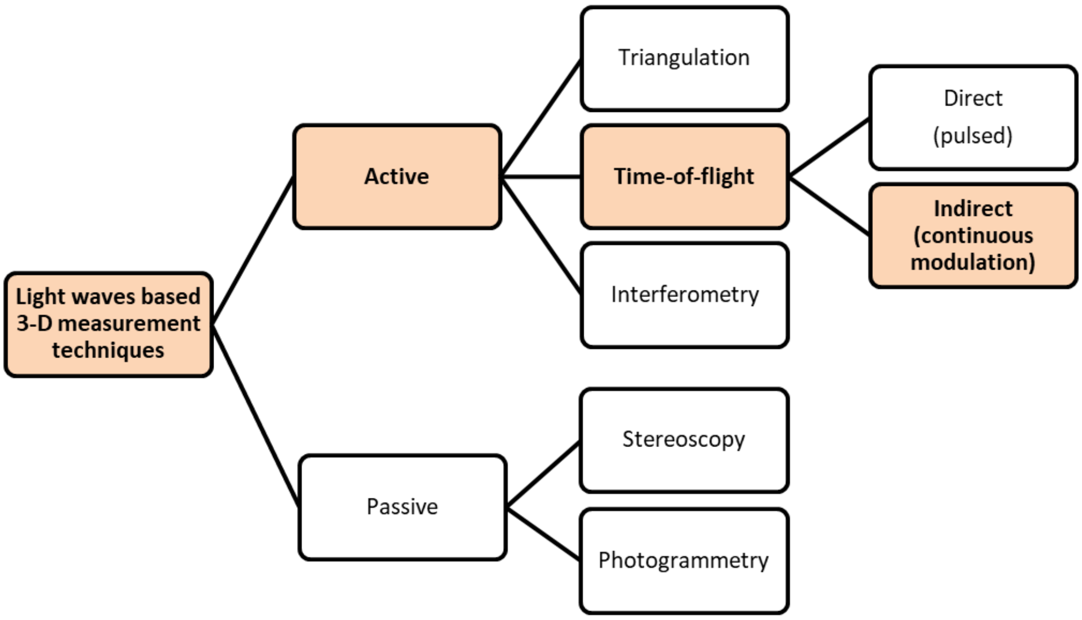

Fig. 1: Classification of non-contact 3-D surface measurement techniques based on light waves. The method discussed in this article is based on an indirect time-of-flight technique.

The TOF method is again divided into two categories:

1. Direct TOF. It is a classical TOF measurement where the time difference Δt between emitted and backscattered light waves is measured by a highly accurate stopwatch and the distance d is estimated from

$$d = \frac{c \cdot \Delta t}{2} \,, \tag{1}$$

   where c is the vacuum velocity of light ($c \approx 3 \cdot 10^8$ m/s). This method is commonly used for (scanned) single-point range systems.

2. Indirect TOF. In this method the round-trip time is indirectly extracted from a time-gated measurement of a sinusoidal modulated light intensity by comparing the phase shift between outgoing and incoming signals. In this case, there is no need of a precise stopwatch, but of time-gated photon counters like, for instance, a specialized CMOS camera sensor [4]. The method introduced in this article can be classified as indirect TOF and is discussed in detail in the next section.

Important passive 3-D measurement systems in Fig. 1 include

1. Stereoscopy. Stereoscopic systems usually employ two cameras, at a fixed distance apart, looking at the same scene. By analyzing the slight differences between the images seen by each camera, it is possible to determine the distance at each point in the images.

2. Photogrammetry. It is the science of making measurements from photographs. It involves taking multiple photographs of an object from various angles and positions with a camera. Then a 3-D computer model of the object is constructed from these photographs using sophisticated algorithms.

2.2 Basic working principle

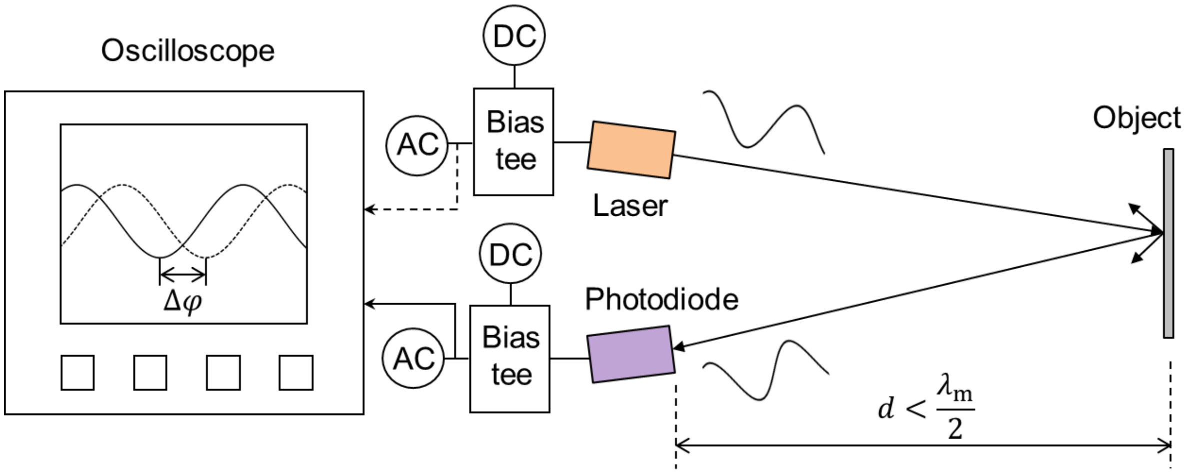

Fig. 2: Basic setup consisting of a laser modulated with a sinusoidal signal of wavelength λ_{m}, a photodiode, and an oscilloscope to measure the phase difference $\Delta\varphi$ between outgoing and incoming harmonic signals after light scattering at an object with distance d.

In order to explain the working principle of the method described here, one should first consider the simple setup in Fig. 2 to measure the distance of a single object point. The setup consists of a sinusoidal modulated laser and a photodiode, both with a bias tee, as well as an oscilloscope to measure the phase difference between outgoing and incoming signals. A bias tee is a passive electrical element consisting of an inductor and a capacitor that superimposes or separates direct current (DC) and alternating current (AC) signal components. The modulated laser beam is backscattered when it strikes an object at a distance d. The backscattered light from the object hits the photodiode under reverse bias and this produces an AC photocurrent with DC offset. The capacitor inside the bias tee blocks the DC and passes only the AC component to the oscilloscope. Since light has a definite speed, the light signal takes some time to travel to and from the object and the delay causes some phase shift that corresponds to the distance from the object. This phase shift $\Delta\varphi$ of the backscattered signal relative to the reference signal can be measured using an oscilloscope. The measured phase shift is proportional to the distance only if the latter is less than half the wavelength of the modulation, $d < \lambda_{\mathrm{m}}/2$. Otherwise ambiguity occurs due to the harmonic nature of the signal.

This ambiguity can be better understood when one considers placing the object at a distance of exactly half the wavelength of the modulation signal, so the backscattered wave would have travelled twice the distance (i.e., to and from the object), which corresponds exactly to a distance of one wavelength of the modulation λ_m. So the backscattered wave will be in phase with the reference signal and therefore will create an ambiguity whether the object is at zero distance or at $d = \lambda_\mathrm{m}/2$. Consequently, the distance should be less than half-wavelength of the modulation. The maximum range of measurement can be increased with larger λ_m. However, a longer wavelength of the modulation results in low depth resolution because a given distance span to be measured expressed as a percentage of λ_m will be small when compared with the same span in case of a small modulation wavelength. Hence, a given device with a fixed capability to resolve phase will have higher accuracy when the distance to be measured approaches $\lambda_\mathrm{m}/2$. In order to have a flexible range of measurement and good accuracy, measurements can be done with different wavelengths of modulation with decreasing λ_m, and by processing these sets of measurements, ambiguity can be resolved.

The simple setup discussed above can be used only to measure one single point. In order to get distance values for multiple points one needs to have a 2-D array of photodiodes and each photodiode connected to a circuit or device that can measure phase, which makes the setup costly and bulky. Another solution is to mount the setup on a movable device and to scan the object or scene, but this is a time-consuming process [3].

An alternative solution is to use an electroabsorption modulator and a CMOS camera to demodulate the signal and calculate the distance, as shown in Fig. 3. Owing to its favorable characteristics [5] a VCSEL is a convenient light source for use in the 3-D imaging setup. An intensity-modulated beam from a VCSEL is expanded using a suitable lens system to illuminate a defined area. The EAM is an optoelectronic device that can vary the amount of light transmitted through it when a voltage is applied. Its working principle is discussed in detail in Sect. 3.1. The same AC signal applied to the VCSEL also modulates the EAM favorably in a synchronous way. The EAM can be placed between lens and CMOS camera sensor, as shown in Fig. 3, or can be placed in front of the lens. Light backscattered from the object is focused by the lens on the image sensor and passes through the EAM. Calculations in the next section show in detail how demodulation is done to produce precise distance measurements by using this method.

2.3 Calculation and demodulation

Figure 4 shows the light signal power at various points along the indicated path of the ray. The optical output power of a sinusoidal modulated VCSEL is

$$P_\mathrm{V}(t) = P_0 \cdot (1 + p \cdot \sin(2\pi f_\mathrm{m} t)) \ , \tag{2}$$

where P_0 is the average power when only a DC bias is applied, f_m is the frequency of the AC signal, t is the time, and the modulation coefficient p is

$$p = \frac{\Delta P}{P_0} \quad (0 \leq p \leq 1) \tag{3}$$

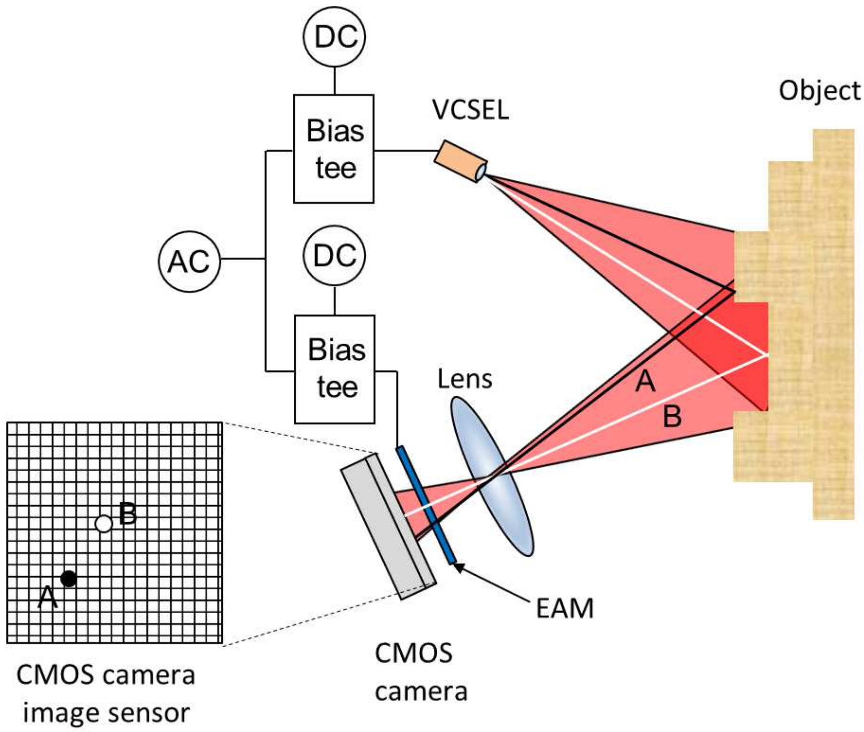

Fig. 3: 3-D measurement setup consisting of electroabsorption modulator (EAM) and CMOS camera to demodulate the signal and calculate the distance. The rays A and B hit different spots and travel different distances and therefore have different phases which are subsequently detected.

with ΔP being the modulation amplitude according to Fig. 4 (top right), where $0 \leq \Delta P \leq P_0$. In order to obtain a good signal-to-noise ratio, p should be close to 1. The light signal power backscattered by the object just before it arrives at the modulator has experienced a time delay Δt and is given by

$$P_{\mathrm{r}}(t) = R_0 \cdot P_{\mathrm{V}}(t - \Delta t) = P_0 \cdot (1 + p \cdot \sin(2\pi f_{\mathrm{m}} t - \Delta\varphi)) \ , \tag{4}$$

where R_0 is the ratio of the light power backscattered by the object towards the modulator to the light power emitted by the VCSEL and $\Delta\varphi$ is the modulation phase delay acquired by the wave after it has travelled a distance of $2d$, i.e., $\Delta\varphi = 2d \cdot 2\pi/\lambda_{\mathrm{m}}$ with $\lambda_{\mathrm{m}} = c/f_{\mathrm{m}}$. The EAM is driven with a DC-biased sinusoidal electrical signal that results in an EAM transmittance of

$$M(t) = M_0 \cdot (1 + m \cdot \sin(2\pi f_{\mathrm{m}} t)) \tag{5}$$

with

$$m = \frac{\Delta M}{M_0} \quad (0 \leq m \leq 1) \ , \tag{6}$$

where M_0 is the light power ratio transmitted through the EAM when only a DC bias is applied and ΔM is the EA modulation amplitude from Fig. 4 (bottom right). Equivalent to (3), $m \approx 1$ for best signal-to-noise ratio. The light signal power transmitted by the modulator is

$$P(t) = M(t) \cdot P_{\mathrm{r}}(t) \tag{7}$$

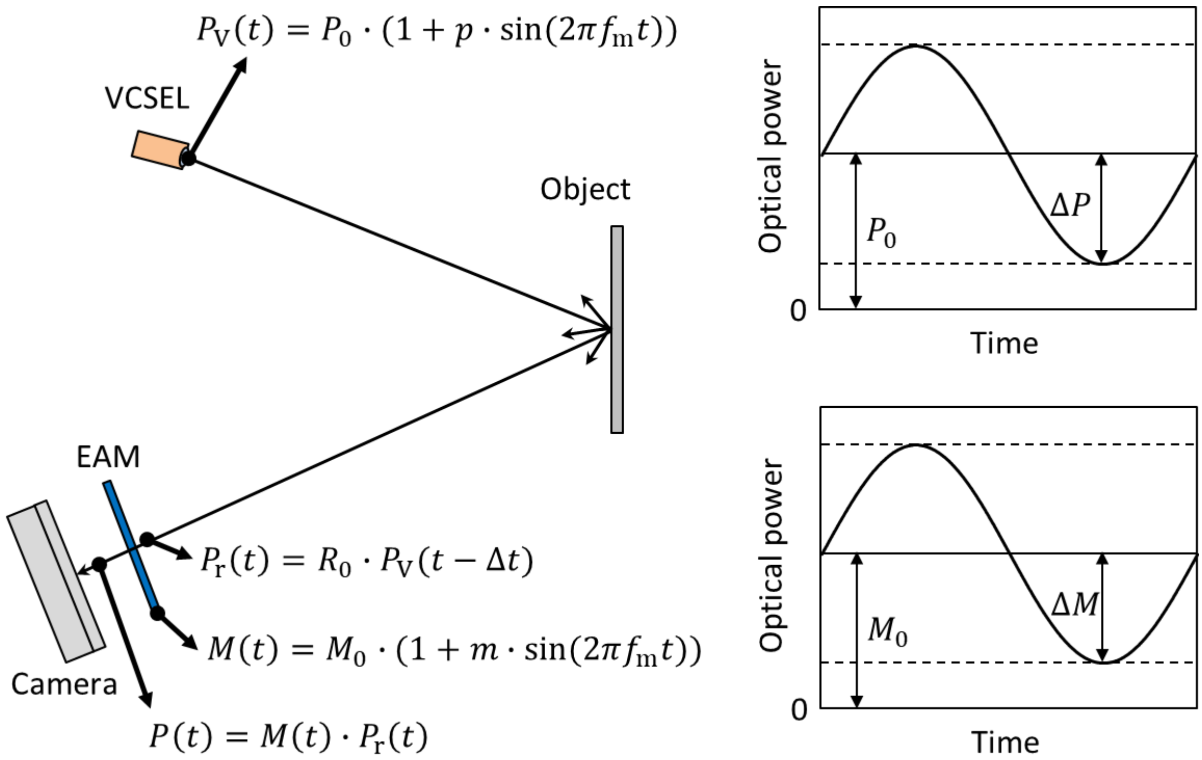

Fig. 4: Sinusoidal modulated light signal power at various points of the 3-D measurement setup in Fig. 3. Top-right and bottom-right diagrams show the time functions of VCSEL and EAM modulation, respectively.

or in explicit form

$$P(t) = P_0R_0M_0 \cdot (1 + m \cdot \sin(2\pi f_m t)) \cdot (1 + p \cdot \sin(2\pi f_m t - \Delta\varphi)) \ . \tag{8}$$

On applying a trigonometric theorem for the product of sine functions one obtains

$$\begin{aligned} P(t) = \frac{P_0R_0M_0}{2} \quad &\cdot \quad [2 + 2m \cdot \sin(2\pi f_m t) + 2p \cdot \sin(2\pi f_m t - \Delta\varphi) \\ &+ \quad mp \cdot \cos(\Delta\varphi) - mp \cdot \cos(4\pi f_m t - \Delta\varphi)] \ . \end{aligned} \tag{9}$$

When this signal is time-averaged $\langle \ldots \rangle_{\delta t}$ by the CMOS camera pixel for a specific time interval $\delta t \gg 1/f_m$, the sin and cos functions with $f_m t$ become zero. This leads to

$$P(\Delta\varphi) = \langle P(t, \Delta\varphi) \rangle_{\delta t} = \frac{P_0R_0M_0}{2} \cdot [2 + mp \cdot \cos(\Delta\varphi)] = A \cdot \cos(\Delta\varphi) + K \ , \tag{10}$$

where $K = P_0R_0M_0$ is a constant and $A = mpK/2$. Background radiation is not considered during the derivation but can be added into K assuming it remains constant over the period of integration. R_0 and $\Delta\varphi$ as well as unavoidable background radiation power are unknown in (10), so at least three measurements are required in order to find $\Delta\varphi$. Typically four samples at discrete phase offsets of 0°, 90°, 180°, and 270° of the function $P(\Delta\varphi)$ are used to sequentially acquire signals P_0, P_1, P_2, and P_3. More measurements improve the precision but also increase the acquisition and computation time, so it is usually sufficient to evaluate the four samples [6]

$$P_0 = P(\Delta\varphi) = A \cdot \cos(\Delta\varphi) + K \;, \tag{11}$$
$$P_1 = P(\Delta\varphi + 90°) = -A \cdot \sin(\Delta\varphi) + K \;, \tag{12}$$
$$P_2 = P(\Delta\varphi + 180°) = -A \cdot \cos(\Delta\varphi) + K \;, \tag{13}$$
$$P_3 = P(\Delta\varphi + 270°) = A \cdot \sin(\Delta\varphi) + K \tag{14}$$

and obtain

$$\tan(\Delta\varphi) = \frac{P_3 - P_1}{P_0 - P_2} \;. \tag{15}$$

Thus we arrive at

$$\Delta\varphi = \arctan \frac{P_3 - P_1}{P_0 - P_2} \;. \tag{16}$$

Phase $\Delta\varphi$ and distance d are related by

$$\Delta\varphi = \frac{2\pi}{\lambda_{\mathrm{m}}} 2d \;. \tag{17}$$

Since $\lambda_{\mathrm{m}} = c/f_{\mathrm{m}}$, (17) becomes

$$d = \frac{c}{4\pi f_{\mathrm{m}}} \Delta\varphi \;, \tag{18}$$

showing that the distance d of an object point is easily obtained by measuring the signals P_i, $i = 0, 1, 2, 3$ for every pixel of the image sensor.

3. Modulator

3.1 Working principle

The EAM works based on the principle of the quantum-confined Stark effect (QCSE). Figure 5 illustrates the band structure of a GaAs quantum well (QW) embedded in AlGaAs barriers. In the very thin ($\approx$ 10 nm) GaAs QW layer, quantum confinement of electrons and holes occurs which results in a radical modification of the optical absorption spectrum [7]. The quantum confinement changes the absorption spectrum from the smooth function of bulk material to a series of steps. Additionally, the confinement also increases the binding energy of the bound excitons, resulting in exceptionally clear exciton resonances at room temperature in GaAs–AlGaAs QWs. An exciton is a bound electron–hole pair where electron and hole are attracted by the electrostatic Coulomb force just as an electron is bound to a proton to form a neutral hydrogen atom [8]. Usually excitons in bulk GaAs are not stable at room temperature. This is because the excitons are ionized and elevated to the conduction band by phonons so fast that no resonances can develop. In contrast, GaAs QWs show excitonic resonances in absorption spectra at room temperature because the binding energy of two-dimensional excitons inside a QW in the ideal case is four times greater than in bulk material [9].

If a static electric field is applied perpendicular to the plane of the QW, the bands tilt and the potential profile is changed, as shown in the right part of Fig. 5. The deformation

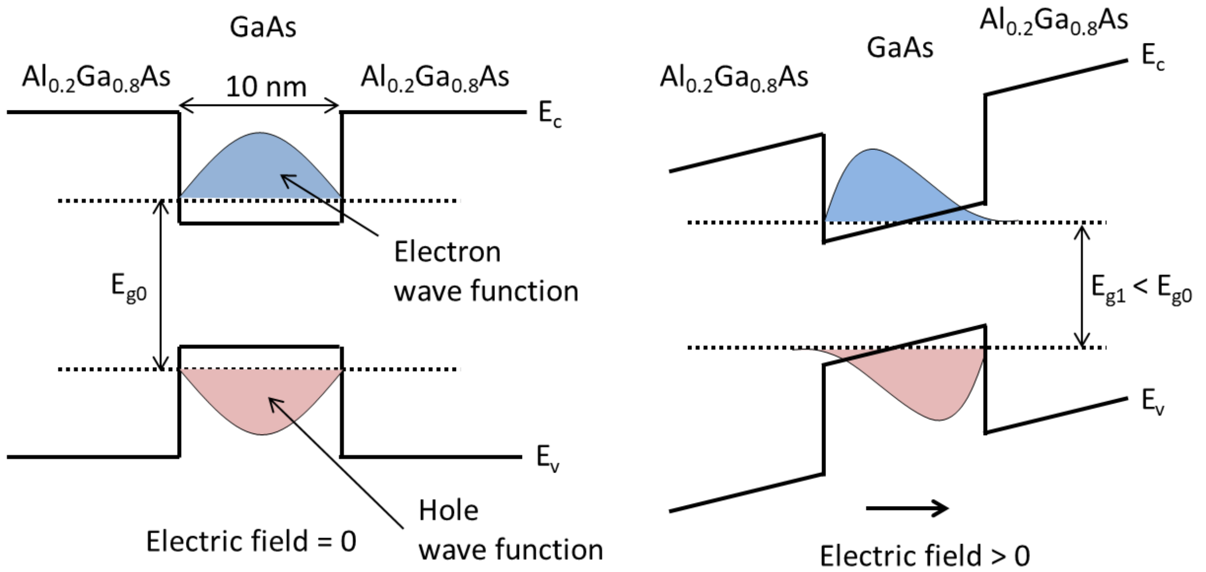

Fig. 5: Schematic band structure of a GaAs–AlGaAs quantum well (left) and tilting of band edges due to an applied electrical field perpendicular to the plane of the quantum well (right). Also indicated are electron and hole wave functions.

also displaces the energies of the bound electron and hole states in such a way that their energy difference becomes smaller, as indicated in the figure. Accordingly the absorption edge shifts towards longer wavelengths, which is known as the QCSE [7]. This effect can be utilized in the design of a low-power, fast absorption modulator. When light whose wavelength corresponds to the absorption peak of the exciton resonance passes through the QW it gets absorbed more when no external field F is applied and is absorbed less when $F > 0$, as the absorption peak shifts towards larger wavelengths. As shown in Sect. 4.2, an optimum operation wavelength has to be found where the absorption change is maximized for a given voltage swing and at the same time the residual transmission loss is small. For a given wavelength, the design of the QW has to be adapted.

3.2 Device structure and fabrication

The fabricated EAM consists of 50 intrinsic 10 nm thick GaAs quantum wells with 10 nm $Al_{0.2}Ga_{0.8}As$ barriers. Since in the first implementation it is to be used as a reflection modulator, an AlAs–$Al_{0.2}Ga_{0.8}As$ Bragg mirror is placed underneath the EAM for reflecting the laser beam. The Bragg reflector is n-doped and has 21 pairs. The two top layers covering the EAM consist of a p-doped 2 µm thick $Al_{0.2}Ga_{0.8}As$ layer and an another p-doped 20 nm thick GaAs layer for protecting the surface. The intrinsic quantum wells are placed between n-doped and p-doped layers in order to get a high field inside the QWs when a reverse bias is applied.

The following fabrication steps are involved for processing the EAM. First a mask is made using photolithography and then reactive ion etching is done on the exposed surface, thereby creating a mesa structure under the mask. Then a p-ring contact consisting of

Ti/Pt/Au (thicknesses of 20 nm / 50 nm / 150 nm) is evaporated. Finally the modulator is cleaved and pasted to the electrical ground of an SMA connector and the top ring contact is wire-bonded to the core of the connector.

4. Device Characterization

4.1 VCSEL

As described in Sect. 3.1, it is necessary to have the right wavelength of operation of the laser that matches with the excitonic absorption peak in order to achieve a high modulation depth of the EAM. In the experiment, a single-mode VCSEL with a peak emission wavelength of around 862 nm is employed which fits well to the EAM, as described in the following section. In a product-type realization of the 3-D sensor, a high-power 2-D VCSEL array should be used.

4.2 EAM

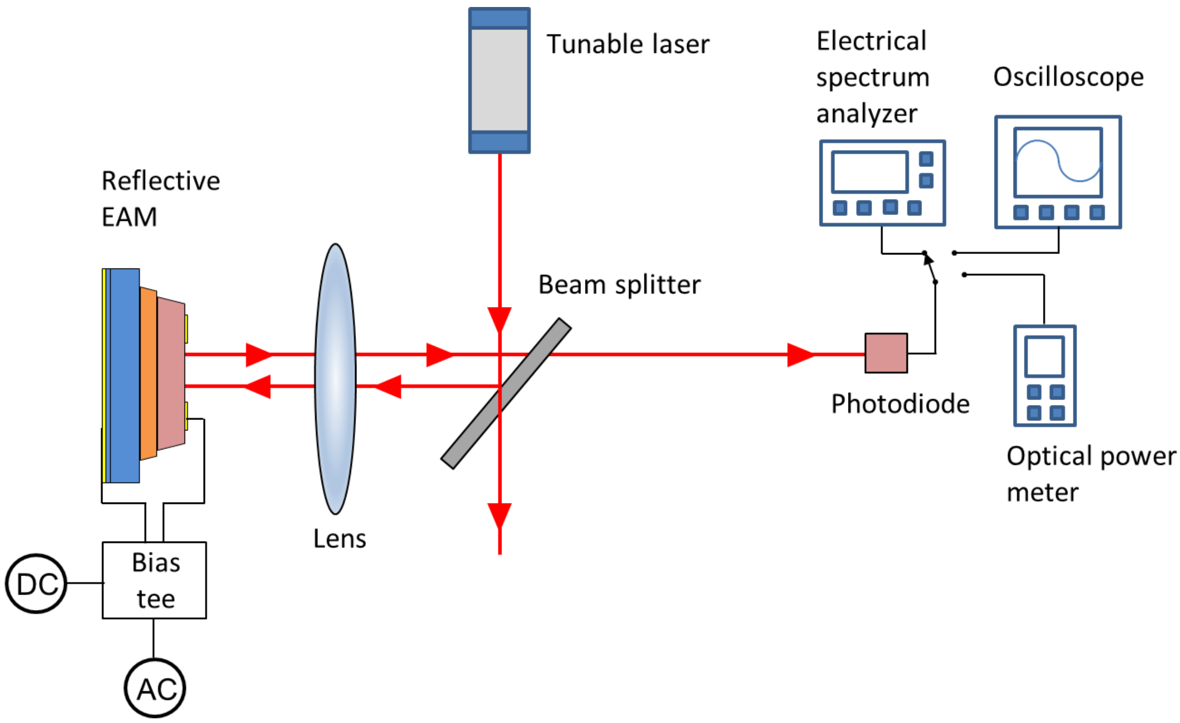

Fig. 6: Setup for EAM characterization.

The setup shown in Fig. 6 is used for characterizing the reflection modulator. A tunable laser with a tuning range from 830 to 880 nm is used as a continuous-wave source. The optical part consists of a lens (5× magnification, NA = 0.1) and a beam splitter. The beam from the tunable laser gets reflected by the beam splitter and is then focused by the lens onto the reflection modulator of dimension 200 µm × 200 µm. The DC bias and

AC signal are added and applied to the modulator through the bias tee. The laser beam is modulated and reflected by the EAM. The light then passes through the beam splitter and is detected by the photodiode. The photodiode can be variably connected to either power meter, oscilloscope, or electrical spectrum analyzer.

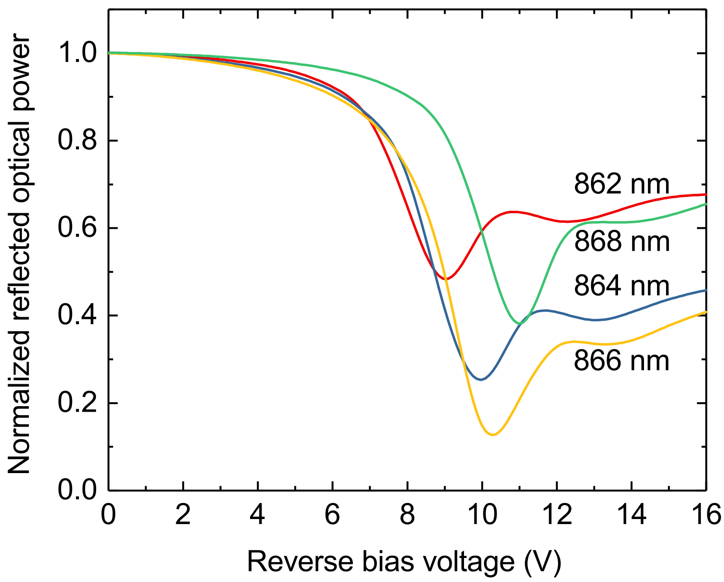

Fig. 7: Normalized reflected light power of a $(200\,\mu\mathrm{m})^2$ size EAM as a function of reverse bias voltage for four different wavelengths of incident tunable laser light.

Figure 7 shows the static characteristics of the modulator which is measured by varying the DC reverse bias without AC signal. The reflected light power is recorded with a power meter. The static characteristics are measured for various wavelengths using the tunable laser. It can be observed that there exists an optimum wavelength for which the modulation depth (difference between highest and the lowest reflectivity) is particularly large. This is due to the fact that maximum absorption occurs when the excitonic peak for an applied voltage coincides with the incident light wavelength. Effects of resonances in the optical cavity formed by the GaAs–air interface and the bottom Bragg mirror also influence the wavelength of maximum modulation depth.

Figure 8 illustrates the dynamic characteristics of the $(200\,\mu\mathrm{m})^2$ size modulator obtained by changing the AC signal frequency for a given DC reverse bias. The measured points are fitted using the first-order low-pass filter function

$$A(f_\mathrm{m}) = -10 \cdot \log_{10} \left[1 + \left(\frac{f_\mathrm{m}}{340.5\,\mathrm{MHz}} \right)^2 \right] \mathrm{dB}\,. \tag{19}$$

The 3 dB cutoff frequency or corner frequency of the modulator is 340.5 MHz. It is inversely proportional to the RC time constant.The capacitance is directly proportional to the mesa area but inversely proportional to the charge separation distance, i.e., the thickness of the multiple QW region. As discussed in Sect. 2.2, higher frequencies of modulation improve the depth resolution. Smaller area modulators have higher cutoff frequencies but allow less light to pass through and also usually reduce the size of the

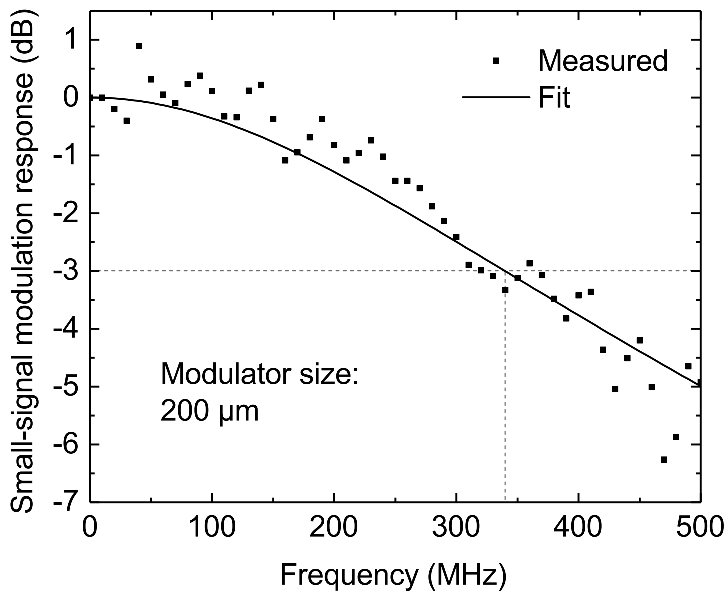

Fig. 8: Small-signal modulation response of a $(200\,\mu\mathrm{m})^2$ size EAM and first-order low-pass fit function according to (19).

image to be captured. On the other hand, larger modulators allow for larger image size but less accurate depth imaging.

5. Conclusion

In summary, various 3-D measurement methods were discussed and a new concept for 3-D imaging was presented. This method uses a sinusoidal modulated VCSEL and a synchronously modulated EAM and works with a regular CMOS camera. Calculations show how distances are determined from measured signals. Static and dynamic characterizations of an EAM were experimentally performed and the optimum operation points of VCSEL and EAM were determined. For high accuracy and precision of the measurements, large modulation amplitude and frequency of both modulated VCSEL and EAM are favorable.

Acknowledgment

The author thanks Philips Photonics GmbH for the MBE growth of the EAM wafer and for providing 860 nm single-mode VCSELs. The author is grateful to Dr. Martin Grabherr for fruitful discussions and valuable suggestions. The technical assistance of Rudolf Rösch, Irene Lamparter, Thomas Zwosta, Susanne Menzel, and Rainer Blood is highly appreciated. Also the author acknowledges Dr. Andreas Trasser and Sven Hettich from the Institute of Electron Devices and Circuits for their help with wire bonding and the signal generators. Last but not least the author expresses his gratitude to Markus Polanik for assisting with reflection spectrum measurements.

References

[1] M. Grzegorzek, C. Theobalt, R. Koch, and A. Kolb (Eds.), *Time-of-Flight and Depth Imaging*, Berlin: Springer-Verlag, 2013.

[2] M. Hansard, S. Lee, O. Choi, and R.P. Horaud, *Time-of-Flight Cameras*, London: Springer, 2013.

[3] J.A. Beraldin, F. Blais, L. Cournoyer, G. Godin, M. Rioux, and J. Taylor, "Active 3D sensing", *IEEE Comput. Graph. Appl.*, vol. 22, pp. 24–35, 2002.

[4] F. Remondino and D. Stoppa (Eds.), *TOF Range-Imaging Cameras*, Berlin: Springer-Verlag, 2016.

[5] R. Michalzik (Ed.), *VCSELs — Fundamentals, Technology and Applications of Vertical-Cavity Surface-Emitting Lasers*, Springer Series in Optical Sciences, vol. 166, Berlin: Springer-Verlag, 2013.

[6] R. Lange and P. Seitz, "Solid-state time-of-flight range camera", *IEEE J. Quantum Electron.*, vol. 37, pp. 390–397, 2001.

[7] D.A.B. Miller, D.S. Chemla, T.C. Damen, A.C. Gossard, W. Wiegmann, T.H. Wood, and C.A. Burrus, "Band-edge electroabsorption in quantum well structures: the quantum-confined Stark effect", *Phys. Rev. Lett.*, vol. 53, pp. 2173–2176, 1984.

[8] C. Kittel, *Introduction to Solid State Physics* (8th ed.), New York: Wiley, 2005.

[9] K.J. Ebeling, *Integrated Optoelectronics*, Berlin: Springer-Verlag, 1993.

Ph.D. Theses

1. Robert Leute,
   GaN-Nanostreifen für LED- und Laseranwendungen,
   March 2017.

2. Marian Caliebe,
   Metallorganische und Hydridgasphasenepitaxie von semipolaren (1122)-orientierten GaN-Schichten auf vorstrukturierten Saphir-Substraten,
   December 2017.

3. Junjun Wang,
   Three-dimensional InGaN/GaN Based Light Emitters with Reduced Piezoelectric Field,
   December 2017.

Master Theses

1. Stefan Lehner,
   Herstellung und Charakterisierung von Vertikallaserdioden mit integriertem Phototransistor,
   Feb. 2017.

2. Markus Miller,
   Resonatorintern gepumpte Halbleiterscheibenlaser mit kleinem Quantendefekt,
   Apr. 2017.

3. Markus Wegerer,
   Experimentelle Untersuchungen zu Durchstimmbarkeit und Leistungsskalierung von optisch gepumpten Halbleiterscheibenlasern bestehend aus zwei Chips,
   Apr. 2017.

4. Ranjan Kumar Rath,
   Investigation of GaN quantum well based chemical sensors with external bias,
   July 2017.

5. Eros La Tona,
   Design, fabrication, and characterization of vertical-cavity surface-emitting lasers with thermally tunable birefringence,
   Aug. 2017.

6. Steven El Bitar,
   Modeling and Characterization of Vertically Operated Quantum-Well-Based Optical Modulators,
   Oct. 2017.

7. Mohamed Elattar,
   Optical and Electrical Investigations on Phototransistor-Integrated Optoelectronic Devices,
   Nov. 2017.

Bachelor Theses

1. Pengyuan Zeng,
   Structural investigations of AlBGaN hetero structures,
   May 2017.

2. Paulette Hatem Hanna Iskander,
   Chemical sensors based on GaN heterostructures,
   Aug. 2017.

3. Abdel Rahman Said,
   Investigations about surface preparation of GaN-based sensor structures,
   Aug. 2017.

Talks and Conference Contributions

[1] S. Bader, P. Gerlach, and R. Michalzik, "Parallel-driven VCSELs with optically controlled current confinement", *European VCSEL Day 2017*, Cardiff, UK, June 2017.

[2] S. Bader, P. Gerlach, and R. Michalzik, "Optically controlled current confinement in parallel-driven VCSELs", *Conf. on Lasers and Electro-Optics Europe, CLEO/Europe 2017*, Munich, Germany, June 2017.

[3] M. Daubenschüz and R. Michalzik, "Efficient experimental analysis of internal temperatures in VCSELs", *Conf. on Lasers and Electro-Optics Europe, CLEO/Europe 2017*, Munich, Germany, June 2017.

[4] K.J. Ebeling and R. Michalzik, "VCSEL technology for imaging and sensor systems applications", *22nd Microoptics Conf., MOC 2017*, plenary paper PL-4, Tokyo, Japan, Nov. 2017.

[5] R. Michalzik, "Two odd VCSEL research topics: birefringence tuning and phototransistor integration", *Schottky Seminar*, Walter Schottky Institut, Technische Universität München, Munich, Germany, July 2017.

[6] T. Pusch, M. Lindemann, N.C. Gerhardt, M.R. Hofmann, and R. Michalzik, "Birefringence tuning in vertical-cavity surface-emitting lasers based on asymmetric heating", *European VCSEL Day 2017*, Cardiff, UK, June 2017.

[7] T. Pusch, E. La Tona, M. Lindemann, N.C. Gerhardt, M.R. Hofmann, and R. Michalzik, "Thermally induced birefringence tuning of 37 GHz in VCSELs", *Conf. on Lasers and Electro-Optics Europe, CLEO/Europe 2017*, Munich, Germany, June 2017.

[8] O. Rettig, J.-P. Scholz, N. Steiger, S. Bauer, T. Hubacek, Y. Li, H. Qi, J. Biskupek, U. Kaiser, K. Thonke, and F. Scholz, "Investigation of boron containing AlBN and AlBGaN layers grown by MOVPE", poster at *12th Int. Conf. on Nitride Semiconductors, ICNS 2017*, Strassbourg, France, July 2017.

[9] O. Rettig, "Epitaxy of boron containing III-nitrides and their applications", *Heimbach Workshop XXXI*, Chemnitz, Germany, Sept. 2017.

[10] O. Rettig, J.-P. Scholz, N. Steiger, S. Bauer, T. Hubacek, M. Zikova, Y. Li, H. Qi, J. Biskupek, U. Kaiser, K. Thonke, and F. Scholz, "Investigation of the growth process of boron containing AIN thin films", poster at *17th European Workshop on Metalorganic Vapour Phase Epitaxy, EWMOVPE XVII*, Grenoble, France, June 2017.

[11] O. Rettig, J.-P. Scholz, N. Steiger, S. Bauer, T. Hubacek, M. Zikova, Y. Li, H. Qi, J. Biskupek, U. Kaiser, K. Thonke, and F. Scholz, "Investigation of phase separation and 3D-growth of boron containing AIGaN-alloys grown by MOVPE", poster at

International Workshop on UV Materials and Devices 2017, IWUMD 2017, Fukuoka, Japan, Nov. 2017.

[12] M.F. Schneidereit, D. Heinz, F. Scholz, S. Chakrabortty, N. Naskar, T. Weil, F. Huber, B. Hörbrand, and K. Thonke, "Functionalization of (In)GaN quantum well structures for selective optical (bio) chemical sensing", *12th Int. Conf. on Nitride Semiconductors, ICNS 2017*, Strassbourg, France, July 2017.

[13] M.F. Schneidereit, "Planar InGaN heterostructures for biochemical sensing", *PulmoSens Fall Meeting*, Reisensburg, Günzburg, Germany, Oct. 2017.

[14] F. Scholz, D. Heinz, M.F. Schneidereit, V. Devaki Murugesan, F. Huber, B. Hörbrand, K. Thonke, S. Chakrabortty, N. Naskar, and T. Weil, "GaN-based hetero structures for gas and bio sensing" (invited), *German Japanese Spanish Workshop on Frontier Photonic and Electronic Materials and Devices*, Son Servera, Mallorca, Spain, Mar. 2017.

[15] F. Scholz, O. Rettig, M. Zikova, T. Hubacek, K. Thonke, J.-P. Scholz, N. Steiger, S. Bauer, M. Hocker, U. Kaiser, Y. Li, and H. Qi, "Epitaxie und Charakterisierung von AlBGaN-Heterostrukturen: Möglichkeiten zum Verspannungsmanagement in UV-LEDs?", *Seminar*, Osram Opto Semiconductors, Regensburg, Germany, Apr. 2017.

[16] F. Scholz, D. Heinz, M.F. Schneidereit, V. Devaki Murugesan, F. Huber, B. Hörbrand, K. Thonke, S. Chakrabortty, N. Naskar, and T. Weil, "GaN-based hetero structures for gas and bio sensing", *Seminar*, Osram Opto Semiconductors, Regensburg, Germany, Apr. 2017.

[17] F. Scholz, "GaN and related heterostructures part I: basics" (invited), *Workshop on Physics at Nanoscale*, Devet Skal, Czech Republic, June 2017.

[18] F. Scholz, "GaN and related heterostructures part II: current research topics and device concepts" (invited), *Workshop on Physics at Nanoscale*, Devet Skal, Czech Republic, June 2017.

[19] F. Scholz, M.F. Schneidereit, D. Heinz, R. Rath, V. Devaki Murugesan, F. Huber, B. Hörbrand, K. Thonke, S. Chakrabortty, N. Naskar, and T. Weil, "GaN-based hetero structures for gas and bio sensing" (invited), *18. Wörlitzer Workshop*, Wörlitz, Germany, June 2017.

[20] F. Scholz, O. Rettig, M. Zikova, T. Hubacek, K. Thonke, J.-P. Scholz, N. Steiger, S. Bauer, M. Hocker, U. Kaiser, Y. Li, J. Biskupek, and H. Qi, "Investigation of epitaxially grown AlB(Ga)N layers on AlN templates" (invited), *EMRS Fall Meeting*, Boston, USA, Nov. 2017.

[21] F. Scholz, O. Rettig, M. Zikova, T. Hubacek, K. Thonke, J. Scholz, N. Steiger, S. Bauer, M. Hocker, U. Kaiser, Y. Li, J. Biskupek, and H. Qi, "Investigation of epitaxially grown AlB(Ga)N layers on AlN templates", *32nd DGKK Workshop Epitaxy of III/V Semiconductors*, Freiburg, Germany, Dec. 2017.

[22] J. Shahbaz, M.F. Schneidereit, B. Hörbrand, S. Bauer, K. Thonke, and F. Scholz, "Optimising InGaN heterostructures for bio and gas sensors", poster at *17th European Workshop on Metalorganic Vapour Phase Epitaxy EWMOVPE XVII*, Grenoble, France, June 2017.

[23] J. Shahbaz, M.F. Schneidereit, D. Heinz, B. Hörbrand, F. Huber, S. Bauer, K. Thonke, and F. Scholz, "Simulation and verification of InGaN heterostructure-based gas and bio sensor design", poster at *12th Int. Conf. on Nitride Semiconductors, ICNS 2017*, Strassbourg, France, July 2017.

[24] J. Shahbaz, "InGaN heterostructures for gas sensing", *PulmoSens Fall Meeting*, Reisensburg, Günzburg, Germany, Oct. 2017.

[25] J. Shahbaz, Y. Liao, M.F. Schneidereit, and F. Scholz, "InGaN heterostructures as gas sensors", *32nd DGKK Workshop Epitaxy of III/V Semiconductors*, Freiburg, Germany, Dec. 2017.

[26] N.C. Gerhardt, M. Lindemann, T. Pusch, R. Michalzik, and M.R. Hofmann, "Ultrafast polarization dynamics with resonance frequencies beyond 100 GHz in birefringent spin-lasers", poster at *Gordon Research Conference, Spin Dynamics in Nanostructures*, Les Diablerets, Switzerland, July 2017.

[27] N.C. Gerhardt, M. Lindemann, T. Pusch, R. Michalzik, and M.R. Hofmann, "High-frequency polarization dynamics in spin-lasers: pushing the limits" (invited), *SPIE Optics + Photonics 2017, Spintronics X*, San Diego, CA, USA, Aug. 2017.

[28] N.C. Gerhardt, M. Lindemann, T. Pusch, R. Michalzik, and M.R. Hofmann, "Ultrafast spin-VCSELs" (invited), *European Semiconductor Laser Workshop*, Lyngby, Denmark, Sept. 2017.

[29] T. Hubacek, O. Rettig, M. Zikova, J.-P. Scholz, M. Hocker, N. Steiger, K. Thonke, Y. Li, U. Kaiser, and F. Scholz, "Effect of boron incorporation into thin AlGaN quantum wells grown by MOVPE", poster at *12th Int. Conf. on Nitride Semiconductors, ICNS 2017*, Strassbourg, France, July 2017.

[30] M. Lindemann, T. Pusch, R. Michalzik, N.C. Gerhardt, and M.R. Hofmann, "Investigations on polarization oscillation amplitudes in spin-VCSELs", *SPIE Photonics West 2017, Vertical-Cavity Surface-Emitting Lasers XXI*, San Francisco, CA, USA, Jan./Feb. 2017.

[31] M. Lindemann, T. Pusch, R. Michalzik, N.C. Gerhardt, and M.R. Hofmann, "Tunable polarization oscillations in resonantly pumped spin-VCSELs", *Conf. on Lasers and Electro-Optics Europe, CLEO/Europe 2017*, Munich, Germany, June 2017.

[32] A. Tibaldi, F. Bertazzi, M. Calciati, M. Goano, P. Gerlach, A. Ott, R. Michalzik, and P. Debernardi, "Multiphysical simulation of vertical-cavity surface-emitting lasers", *European VCSEL Day 2017*, Cardiff, UK, June 2017.

Publications

[1] S. Bader, P. Gerlach, and R. Michalzik, "Optically controlled current confinement in parallel-driven VCSELs", in Online Digest *Conf. on Lasers and Electro-Optics Europe, CLEO/Europe 2017*, paper CB-3.4, one page. Munich, Germany, June 2017.

[2] M. Daubenschüz and R. Michalzik, "Efficient experimental analysis of internal temperatures in VCSELs", in Online Digest *Conf. on Lasers and Electro-Optics Europe, CLEO/Europe 2017*, paper CB-P.8, one page. Munich, Germany, June 2017.

[3] K.J. Ebeling and R. Michalzik, "VCSEL technology for imaging and sensor systems applications" (plenary paper), in Proc. *22nd Microoptics Conf., MOC 2017*, pp. 20–21. Tokyo, Japan, Nov. 2017.

[4] D. Heinz, F. Huber, M. Spiess, M. Asad, L. Wu, O. Rettig, D. Wu, B. Neuschl, S. Bauer, Y. Wu, S. Chakrabortty, N. Hibst, S. Strehle, T. Weil, K. Thonke, and F. Scholz, "GaInN quantum wells as optochemical transducers for chemical sensors and biosensors", *IEEE J. Select. Topics Quantum Electron.*, vol. 23, pp. 1900109-1–9, 2017.

[5] T. Pusch, E. La Tona, M. Lindemann, N.C. Gerhardt, M.R. Hofmann, and R. Michalzik, "Monolithic vertical-cavity surface-emitting laser with thermally tunable birefringence", *Appl. Phys. Lett.*, vol. 110, pp. 151106-1–3, 2017.

[6] T. Pusch, E. La Tona, M. Lindemann, N.C. Gerhardt, M.R. Hofmann, and R. Michalzik, "Thermally induced birefringence tuning of 37 GHz in VCSELs", in Online Digest *Conf. on Lasers and Electro-Optics Europe, CLEO/Europe 2017*, paper CB-3.1, one page. Munich, Germany, June 2017.

[7] F. Scholz, K. Thonke, and T. Weil, "Sensitiv und selektiv: Optische Gas- und Biosensorik mit Halbleiter-Heterostrukturen", *Laborpraxis*, pp. 44–46, Apr. 2017.

[8] F. Scholz, *Compound Semiconductors: Physics, Technology and Device Concepts*, Singapore: Pan Stanford, Oct. 2017.

[9] N.C. Gerhardt, M. Lindemann, T. Pusch, R. Michalzik, and M.R. Hofmann, "High-frequency polarization dynamics in spin-lasers: pushing the limits" (invited), in *Spintronics X*, H.-J. Drouhin, J.-E. Wegrowe, M. Razeghi, H. Jaffrès (Eds.), Proc. SPIE 10357, pp. 103572F-1–6, 2017.

[10] M. Hocker, P. Maier, I. Tischer, T. Meisch, M. Caliebe, F. Scholz, M. Mundszinger, U. Kaiser, and K. Thonke, "Three-dimensional cathodoluminescence characterization of a semipolar GaInN based LED sample", *J. Appl. Phys.*, vol. 121, pp. 075702-1–7, 2017.

[11] Y. Li, H. Qi, T. Meisch, M. Hocker, K. Thonke, F. Scholz, and U. Kaiser, "Formation of I_2-type basal-plane stacking faults in $In_{0.25}Ga_{0.75}N$ multiple quantum wells grown on a $(10\bar{1}1)$ semipolar GaN template", *Appl. Phys. Lett.*, vol. 110, pp. 022105-1–4, 2017.

[12] M. Lindemann, T. Pusch, R. Michalzik, N.C. Gerhardt, and M.R. Hofmann, "Investigations on polarization oscillation amplitudes in spin-VCSELs", in *Vertical-Cavity Surface-Emitting Lasers XXI*, K.D. Choquette, C. Lei (Eds.), Proc. SPIE 10122, pp. 101220O-1–7, 2017.

[13] M. Lindemann, T. Pusch, R. Michalzik, N.C. Gerhardt, and M.R. Hofmann, "Tunable polarization oscillations in resonantly pumped spin-VCSELs", in Online Digest *Conf. on Lasers and Electro-Optics Europe, CLEO/Europe 2017*, paper CB-3.2, one page. Munich, Germany, June 2017.

[14] K. Lorenz, E. Wendler, A. Redondo-Cubero, N. Catarino, M. Chauvat, S. Schwaiger, F. Scholz, E. Alves, and P. Ruterana, "Implantation damage formation in a-, c- and m-plane GaN", *Elsevier Acta Materialia*, vol. 123, pp. 177–187, 2017.

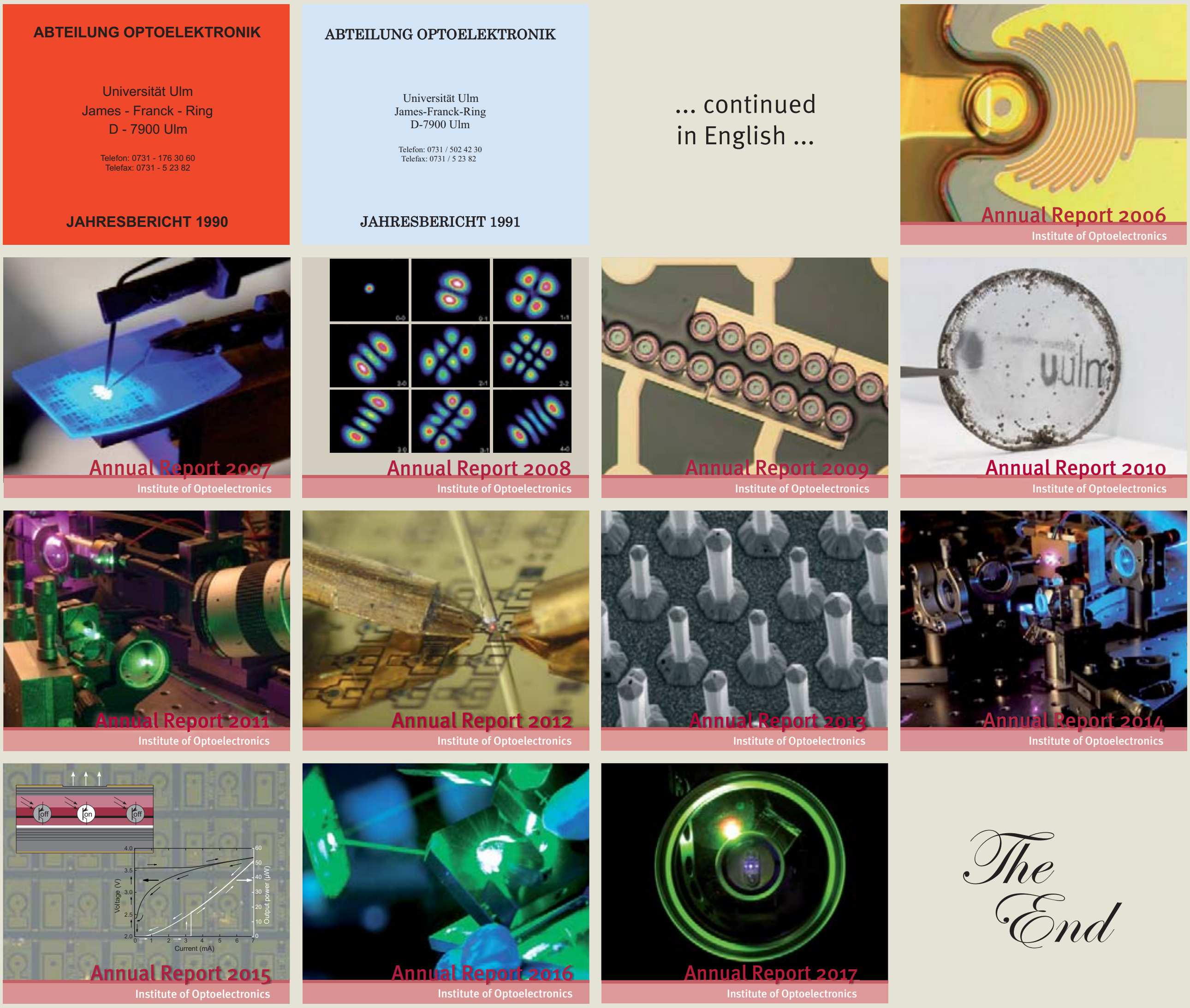

Ulm University | Institute of Optoelectronics | Annual Report 2017

ulm university universität ulm

Ulm University
Institute of Optoelectronics
Albert-Einstein-Allee 45
89081 Ulm | Germany